



TURK GEO

TURKISH JOURNAL OF GEOSCIENCES

g/KUP '4939/98; 8

OPEN ACCESS



dergipark.org.tr/tr/pub/turkgeo
turkgeosciences@gmail.com

VWTMI GQ.'F gego dgt 14244
Xqno g<5/'Kuwg<4

About The Journal

Turkish Journal of Geosciences is a multi-disciplinary open-access journal aimed to publish peer-reviewed original research and review articles covering all aspects of geosciences. The journal includes a wide scope of information on scientific and technical advances in all areas related to geosciences and indexed in international indices and databases that publish studies on earth sciences.

Aim and Scope

TURKGEO Journal has the following aim and scopes;

Aim of TURKGEO

- TURKGEO aims to promote the theory and practice from the integration of instruments, methodologies, and technologies and their respective uses in the environmental and other natural sciences.
- TURKGEO aims to provide a widely accessible discussion environment that will strengthen and accelerate the exchange of knowledge and experience among scientists, researchers, engineers and other implementers involved in the subject directly or indirectly.

Scope of TURKGEO

- Earth and Environmental Sciences Applications
- Geographic Information Systems
- Remote Sensing
- Photogrammetry
- Geostatistics
- GPS/GNSS
- RADAR/SAR/LIDAR and Laser Scanning
- Spatial Data Infrastructure
- Spatial Decision Support Systems
- Climate Change
- Geology
- Geomorphology
- Hydrogeology
- Geophysics
- Hydrology and Water Resources
- Oceanography

Publishing Frequency

2 issues per year (June-December)

ISSN

2717-7696

WEB

<https://dergipark.org.tr/en/pub/turkgeo>

Contact

turkgeosciences@gmail.com

EDITOR

Assoc. Prof. Dr. Osman ORHAN

Mersin University, FBE / Remote Sensing and Geographic Information Systems, Mersin

SECTION EDITORS

Geomatics Engineering

Assist. Prof. Dr. Cemil GEZGİN, Aksaray University

Assist. Prof. Dr. B. Baha BİLGİLİOĞLU, Gümüşhane University

Environmental Engineering

Assoc. Prof. Dr. Emine BAŞTÜRK, Aksaray University

Geology Engineering

Assist. Prof. Dr. Bahattin GÜLLÜ, Aksaray University

Dr. Mustafa Haydar TERZİ, Aksaray University

Dr. Hacer BİLGİLİOĞLU, Aksaray University

Mining Engineering

Dr. Mehmet MESUTOĞLU, Konya Technical University

Civil Engineering

Dr. Yakup BÖLÜKBAŞI, Aksaray University

EDITORIAL BOARD

Prof. Dr. Abdurrahman EYMEN, Erciyes University
Prof. Dr. Alper BABA, Izmir Institute of Technology
Prof. Dr. C. Serdar BAYARI, Hacettepe University
Prof. Dr. Fatih İŞCAN, Konya Technical University
Prof. Dr. Fatih POYRAZ, Cumhuriyet University
Prof. Dr. Fevzi KARSLI, Karadeniz Technical University
Prof. Dr. Füsün BALIK ŞANLI, Yıldız Technical University
Prof. Dr. Hakan KARABÖRK, Konya Technical University
Prof. Dr. Hakan YAVAŞOĞLU, Istanbul Technical University
Prof. Dr. Yusuf Kağan KADIOĞLU, Ankara University
Prof. Dr. Hediye ERDOĞAN, Aksaray University
Prof. Dr. Himmet KARAMAN, Istanbul Technical University
Prof. Dr. İbrahim TİRYAKIOĞLU, Afyon Kocatepe University
Prof. Dr. Mehmet ÇELİK, Ankara University
Prof. Dr. Murat YAKAR, Mersin University
Prof. Dr. Mustafa YANALAK, Istanbul Technical University
Prof. Dr. Nebiye MUSAOĞLU, Istanbul Technical University
Prof. Dr. Niyazi ARSLAN, Cukurova University
Prof. Dr. Orhan AKYILMAZ, Istanbul Technical University
Prof. Dr. Reha Metin ALKAN, Istanbul Technical University
Prof. Dr. Tolga ÇAN, Cukurova University
Assoc. Prof. Dr. Ahmet MERT, Isparta University of Applied Sciences
Assoc. Prof. Dr. Emine BAŞTÜRK, Aksaray University
Assoc. Prof. Dr. Hüseyin KARAKUŞ, Dumlupınar University
Assoc. Prof. Dr. Mustafa EL-RAWY, Shaqra University
Assoc. Prof. Dr. Sefa YALVAÇ, Gumushane University
Assoc. Prof. Dr. Selçuk ALEMDAĞ, Gumushane University
Assoc. Prof. Dr. Serkan DOĞANALP, Konya Technical University
Assoc. Prof. Dr. Tekin SUSAM, Gazi Osman Pasa University
Assoc. Prof. Dr. Uğur AVDAN, Eskisehir Technical University
Assoc. Prof. Dr. Zaide DURAN, Istanbul Technical University
Assist. Prof. Dr. Ahmet ÇİLEK, Cukurova University
Assist. Prof. Dr. Aydan YAMAN, Aksaray University
Assist. Prof. Dr. Bahattin GÜLLÜ, Aksaray University
Assist. Prof. Dr. Can İBAN, Mersin University
Assist. Prof. Dr. Erkan YILMAZER, Aksaray University
Assist. Prof. Dr. Esra GÜRBÜZ, Aksaray University
Assist. Prof. Dr. Kamil KARATAŞ, Aksaray University
Assist. Prof. Dr. Nizar POLAT, Harran University
Assist. Prof. Dr. Özlem GÜLLÜ, Aksaray University
Assist. Prof. Dr. Resul ÇÖMERT, Gumushane University
Assist. Prof. Dr. Senem TEKİN, Adıyaman University
Assist. Prof. Dr. Zehra YİĞİT AVDAN, Eskisehir Technical University
Dr. Burak Ömer SARAÇOĞLU
Dr. Fabiana CALO, CNR IREA
Dr. Homayoun MOGHIMI, Payame Noor University
Dr. Kaan KALKAN, TUBITAK-UZAY Space Technologies Research Institute
Dr. Mert MUTLU, Aksaray University
Dr. Müge ÜNAL ÇİLEK, Cukurova University
Dr. Syed Mobasher AFTAB, University of Balochistan

ADVISORY BOARD

Prof. Dr. Bahadır AKTUĞ, Ankara University
Prof. Dr. Dursun Zafer ŞEKER, Istanbul Technical University
Prof. Dr. Hacı Murat YILMAZ, Aksaray University
Prof. Dr. Haluk ÖZENER, Bogazici University
Prof. Dr. Hatim ELHATİP, Aksaray University
Prof. Dr. Mustafa AFŞİN, Aksaray University
Prof. Dr. Mustafa IŞIK, Aksaray University

TECHNICAL STAFF

Ahmet Tarık TORUN, Aksaray University
Burhan Baha BİLGİLİOĞLU, Gumushane University
Halil İbrahim GÜNDÜZ, Aksaray University
Ozan ÖZTÜRK, ISTANBUL Technical University

Contents

Research Articles;

Page	Article Titles and Authors
49-	<i>Parametric Analysis of Factors Affecting the Rainfall Induced Slope Stability</i> Furkan Veli Özçelik, Murat Ergenokon Selçuk
58-	<i>Analysis of the threat of forest fires to ancient cities by GIS and Remote Sensing methods</i> Ezgi Tükel, Kaan Kalkan
64-	<i>Application of Remote Sensing and GIS techniques for detecting burned areas and severity. A case study of the National Park "Dajti Mountain", Albania</i> Edmond Pasho, Arben-Q. Alla, Ernest Ramaj
75-	<i>Investigation of the Hamamayağı/Ladik (Samsun, Turkey) geothermal field and it's surroundings by optical Remote Sensing with GIS methods</i> Ömer Faruk Uzun, Orkun Turgay
84-	<i>Forest fire disaster risk analysis using Sentinel 2 and Landsat images case study: Al-Qoubaiyat and Tyre regions, Lebanon</i> Mohamed Issa, Mohammad Abboud

Parametric Analysis of Factors Affecting the Rainfall Induced Slope Stability

Furkan Veli Özçelik ^{*1}, Murat Ergenokon Selçuk ¹

¹Yıldız Technical University, Civil Engineering Faculty, Civil Engineering Department, Istanbul, Turkey

Keywords

Slope stability
Rainfall infiltration
Unsaturated soil
Shear strength

ABSTRACT

Slope failures are one of the most vital problems in geotechnical engineering applications which may cause damage both in human life and financial. Slope failures are frequently observed especially in regions where rainfall is high. The most important factor affecting slope stabilities is rainfall infiltration. It is known that infilled soils are generally unsaturated soil. Therefore, the analysis of infill slopes should be performed within the scope of unsaturated soil mechanics. Rainfall infiltration causes the groundwater level to rise, which reduces the shear strength of the soil causing slope instability. In this study, the effect of rainfall intensity, rainfall duration, soil permeability, groundwater level, cohesion of soil, internal friction angle of the soil, and slope angle of the slope on the slope stability were analyzed parametrically by using GEOSTUDIO software. The infiltration analyses were performed using Seep/w module and factor of safety number of unsaturated soil slope were determined using Morgenstern method of Slope/w module of GEOSTUDIO software. Furthermore, different factor of safety numbers was found for each analysis along with the interpretation of the parameters effecting the slope stability. The results obtained in the present investigation showed that the rainfall intensity affects the stability of the slope. It was determined that there existed a non-linear relationship between rainfall intensity and safety number. As the rainfall intensity increases, the negative pore water pressure in the soil decreases nonlinearly, and the factor of safety number of the slope similarly decreases by 10% relative to the initial condition. When the rainfall duration change was taken into account, it was found that short time-heavy rainfalls affected the slope stability more than long time-low density rainfalls. Moreover, slope angle significantly influenced slope stability. It was observed that when the slope angle increased from 40° to 50°, factor of safety number decreased by 18.34%.

1. INTRODUCTION

Slope stability problems are among the common problems in geotechnical engineering applications. For many years, natural or artificial slopes have been of special interest to the geotechnical engineers. The effect of rainfall is one of the most significant factors affecting slope stability. Landslides on unsaturated soils usually occur during heavy rainy seasons. In other words, slope failures are triggered by the effect of rainfall. Many natural events, climatic and geological conditions have shown to trigger slope stability. Some of the factors affecting slope stability are slope of the slope, moisture content, pore water pressure change. In order to understand the effects of infiltration on unsaturated soil, its effect on slope

stability must be studied. Several numerical and theoretical studies have been carried out on slopes under the effect of rainfall and reported in the literature.

The slope failures that occurred in Hong Kong and attempts to address the likely causes of these failures investigated by (Au, 1998). The author reported that the soils that were largely non-cohesive, steep terrain and intensive development were typical, slope failures frequently occurred, where intense rainfall in Hong Kong. Even though the impact of rainstorms on failures had not to be understood completely yet. Au, (1998) observed that rainfall intensity, areal extent, position and duration of the rainstorm had direct effects on the slope failure events.

* Corresponding Author

(ozcelikfv@gmail.com) ORCID ID 0000-0002-1989-6957
(meselcuk@yildiz.edu.tr) ORCID ID 0000-0003-1890-7965

Cite this article

Rainfall induced landslides on partially saturated soil slopes were investigated by using the 2011 Umyeonsan landslides at the center of Seoul, Korea by (Jeong et al., 2017). The comprehensive investigation results in the mountainous area showed that the landslide activity is mainly related to rainfall and soil characteristics, slope and vegetation. Numerical analysis was also carried out to confirm the influence of these factors on the occurrence of landslides. Special attention is paid to rainfall infiltration analysis to determine the depth of the wet zone damaged by shallow and deep slopes of watershed-scale landslides. The simulation results were in good agreement with the investigation results, indicating that the method is suitable for the simulation of unsaturated soil landslides

Wang et al. (2020) studied the stability of a three-layer heterogeneous slope based on the generalized limit equilibrium method. The results showed that the stability of the slope decreased with the increase of rainfall intensity until it is destroyed. The safety factor of the slope was the lowest for a period of time after the rain stops. This situation implied that slopes are more susceptible to damage. With the increase of rainfall, the seepage field and stress field of the slope have undergone significant changes, which eventually makes the slope unstable. Consequently, the slope is considerably tended to landslides. Hence, we have to pay attention to monitoring the safety of slopes during rainstorms and for a period after the rainfall stops.

Karabulut, (2019) investigated the effects of rainfall infiltration into the soil on a high embankment slope built under unsaturated soil conditions on the stability by numerical analysis. The material parameters were determined from the laboratory tests performed on soil samples taken from the field after the embankment was built and from the ground-water characteristic curve. Pore water pressure changes were determined by using the SEEP / W module of the GEOSTUDIO software for the case of the seepage of rainfall into the slope, and the stability of the slope was investigated with the SLOPE / W module. Karabulut, (2019) observed that the change of groundwater level in unsaturated soils affects the shear strength of the soils. With the increase of the groundwater level, the number of safeties has decreased due to the shear strength of the soil. Furthermore, Karabulut, (2019) observed that rainfall intensity played an important role in slope stability, especially on unsaturated soils. Shear strength of the slope decreases with the increase of monthly rainfall intensity. However, in soils with low permeability, it was observed that the increase in the intensity of rainfall did not significantly change the slope stability, as the rainfall did not cause a significant increase in pore water pressures due to the inability of the rainfall to penetrate into the soil.

In this paper, parametric analyses of the factors affecting the rainfall induced slope stability were performed by GEOSTUDIO software. Hereby, factor

of safety changes and percent decreases relative to the initial value were presented.

2. UNSATURATED SOIL MECHANICS

In classical soil mechanics applications, the conditions where the soil has positive pore water pressure are taken into account. However, in unsaturated soils, conditions where the pore water pressure is negative are taken into consideration. Soils are classified according to the water content in them as well as the size of the void that forms them. If the voids of the soils are completely filled with water, such soils are called saturated soils. If the voids are filled with a small amount of water, such soils are also called unsaturated soils (Önalp and Arel, 2013).

2.1. Suction Stress

It is known that in unsaturated soils, soil suction is related to the free energy of ground water. Matric and osmotic suction are components of this free energy. Total soil suction is obtained by summing up the two basic components, matric and osmotic suction components (Karabulut, 2019).

$$\psi = (ua - uw) + \pi \text{ (kPa)} \quad (2.1)$$

Where;

π = Osmotic suction (kPa), ua = Pore air pressure (kPa), uw = Pore water pressure (kPa), ψ = Total suction (kPa)

2.2. Soil Water Characteristic Curve

Soil-water characteristic curve (SWCC) is a considerable concept in determining unsaturated soil properties. Soil-water characteristic curve is generally defined as the relationship between soil water content and suction. Unsaturated soil properties can be determined by using soil water characteristic curve and saturated soil properties. In this case, the soil-water characteristic curve must be accurately estimated or measured and interpreted (Fredlund, 2012).

2.3. Shear Strength in Unsaturated Soils

The safety of many engineering structures depends on the strength of the soil that have located. Bearing capacity, lateral soil pressure, and slope stability are geotechnical applications depending on the shear strength of the soil. It is substantial to determine the shear strength of unsaturated soils because unsaturated soils are often used in the construction of engineering structures. It is also substantial to determine the changes in shear strength that may occur due to water infiltration in unsaturated soils (Fredlund, 2012).

The shear strength of unsaturated soils can be expressed in independent stress state variables. Any two of the stress state variables can be used for the shear strength equation. Equation (2.2) is obtained by using the $(\sigma-ua)$ and $(ua-uw)$ stress variables (Fredlund, 2012).

$$\tau=c'+(\sigma-ua) \tan\phi'+(ua-uw)\tan\phi^b \quad (2.2)$$

Where, $(\sigma-ua)$ refers to the effective normal stress, $(ua-uw)$ matric suction, and (ϕ_b) the angle that indicates the amount of increase in shear strength due to matric suction.

Vanapalli 1996, proposed equation (2.3) by developing a physical model to obtain the shear strength of the unsaturated soil by defining the change of the water area at different saturation degrees along a soil-water characteristic curve. By this equation, shear strength can be determined for each desired matric suction change (Tetik, 2020).

$$\tau=c'+(\sigma n-ua) \tan\phi'+(ua-uw) [(\tan\phi') (\theta-\theta_r/\theta_s-\theta_r)] \quad (2.3)$$

Where, θ , θ_r , θ_s refers to the volumetric water content, residual volumetric, water content and saturated volumetric water content respectively.

3. MATERIAL PROPERTIES

Soil parameters to be used in this study quoted from Aslan Fidan, (2017). Aslan Fidan, (2017) has worked around Veysel Karani Pond planned to be built in Veysel Karani Town of Baykan District of Siirt Province.

Within the scope of the field study of the Aslan, research wells were dug in six different locations in the study area in order to examine the geology of the region and to take samples for the necessary experiments.

3.1. Index and Physical Properties of the Soil

Determining the saturated and unsaturated parameters of the soil for slope stability analysis under the effect of rainfall infiltration of unsaturated soil is necessary. For this reason, the index and physical properties and shear resistance parameters of the examined clay soil were determined by routine laboratory experiments (Table 1). The unsaturated parameters of the soil were obtained by determining the soil-water characteristic curve by performing the filter paper test (Aslan Fidan, 2017).

Table 1. Index and Physical Properties of the Soil

Soil Index/Physical Properties	Change Interval
Natural Water Content (%)	21.37-25.83
Liquid Limit (%)	22.62-62.15
Plastic Limit (%)	15.74-26.51
Plasticity Index (%)	6.88-35.64
#4 sieve remaining (%)	0.16-48.74
#200 sieve passing (%)	31.25-90.05
Specific Gravity	2.72-2.75
Natural Unit Volume Weight (KN/m ³)	18.35-20.11
Permeability Coefficient (m/sec)	1x10 ⁻⁷ -6x10 ⁻⁷

3.2. Soil Water Characteristic Curve

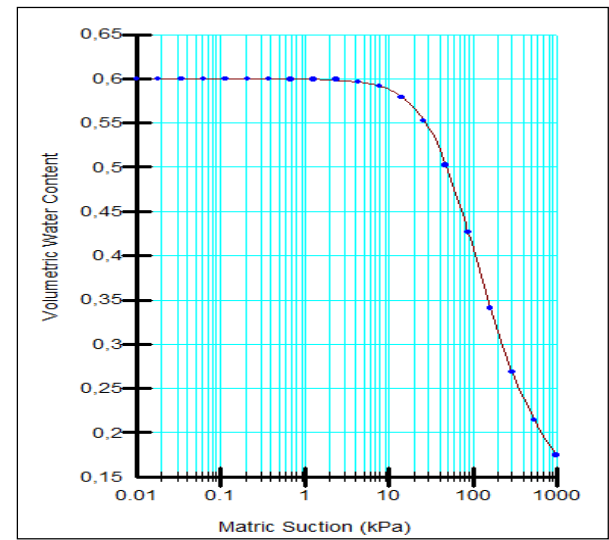


Figure 1. SWCC of the soil sample (Aslan Fidan, 2017)

One of the required input parameters for a transient analysis is the volumetric water content function. Since it can sometimes be difficult or time consuming to obtain a volumetric water content function, it may be of benefit to be able to develop an estimation of the volumetric water content function using either a closed-form solution that requires user-specified curve-fitting parameters, or to use a predictive method that uses a measured grain-size distribution curve. Seep/w module has several methods available to develop a volumetric water content function. One is to estimate a Data point function using a predictive method based on grain size, in which closed form equations based on known curve fit parameters. The soil-water characteristic curve obtained with the Data-Point Suction option in the Seep/w module of GEOSTUDIO software is shown in Figure 1.

3.3. Shear Resistance Parameters

Aslan Fidan, (2017) determined the total shear strength parameters required for slope stability analysis by unconsolidated-undrained triaxial pressure test (UU), and effective shear strength

parameters by consolidated-undrained triaxial pressure test (CU). According to the triaxial pressure tests (UU-CU), the shear resistance parameters of ophiolite clay are shown in Table 2.

Table 2. Shear resistance parameters of the soil (Aslan Fidan, 2017)

Total Cohesion c (kPa)	Total Internal Friction Angle, ϕ (°)	Effective Cohesion, (kPa)	Effective Internal Friction Angle, ϕ' (°)
66,87	12,4	15	14

4. METHODOLOGY

In the scope of this paper, GEOSTUDIO software was used which is a package software developed to provide solutions to geotechnical problems. There are eight different modules in the program: Slope/w, Sigma/w, Seep/w, Quake/w, Temp/w, Ctran/w, Air/w, Vadose/w. Each module is designed to solve different problems (GEOSLOPE, 2012).

4.1. Seep/w Module

The SEEP module provides numerical modelling of water flows in saturated and unsaturated soils. Advantages of numerical modelling over physical modelling; It can be listed as providing the solution of complex problems in a short time, modelling many different situations during the analysis, obtaining the results in every desired location at the end of the analysis, taking into account more boundary conditions (GEOSLOPE, 2015). There are lots of different analysis options in Seep Module. Within the scope of this study, transient seepage analysis will be used. Transient seepage analysis can be defined as a constantly changing situation. In order to obtain the change occurring at the end of the period determined in the transient seepage analysis, the pore water pressures of the soil at the beginning of the analysis should be introduced to the soil as the initial condition.

4.2. Slope/w Module

The SLOPE module provides the safety number of slope stability to be obtained by limit-equilibrium analysis methods. Morgenstern-Price, Spencer, Bishop, Janbu, Sarma, Lowre-Karaifath limit-balance methods can be used in the software. (GEOSLOPE, 2012) In this study, the Morgenstern-Price method was preferred as the limit-equilibrium method. Morgenstern and Price, (1965) developed a method similar to the Spencer method, but they allowed for various user-specified interslice force functions. Constant, Half-sine, Trapezoidal, Data-point specified are the interslice functions available in Slope/w for use with the Morgenstern-Price method (GEOSLOPE, 2012). Selecting the constant function

makes the Morgenstern-Price method identical to the Spencer method. In this study, Morgenstern-Price analysis with a half-sine function was used due to considering both interslice shear and normal forces. Simpler methods that do not include all interslice forces and do not satisfy all equations of equilibrium sometimes can err on the unsafe side. In summary, the Morgenstern-Price method:

- Considers both shear and normal interslice forces,
- Satisfies both moment and force equilibrium, and
- Allows for a variety of user-selected interslice force function (GEOSLOPE, 2012).

5. ANALYSIS AND EVALUATIONS

In this study, same slope geometry which has 10 m height, and 40° slope angle were used. In the analyses, all other parameters were kept constant, except for the parameter whose effect of change was examined. Rainfall intensities were also investigated using the actual rainfall data of the study area.

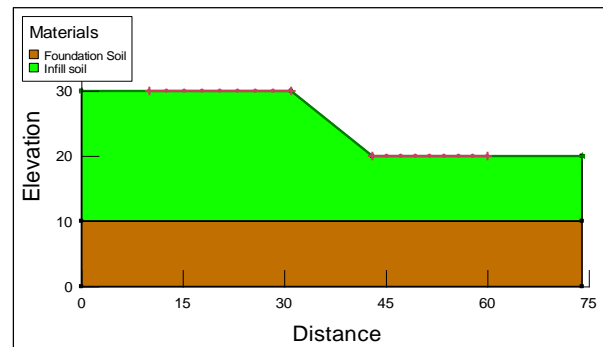


Figure 1. Slope model and Initial ground water table

5.1. Effect of Rainfall Intensity on Slope Stability

The effect of rainfall intensity on slope stability was investigated in unsaturated soil. At the initial conditions factor of safety was found as 1.75.

In the analyses, the monthly total rainfall amounts were converted into rainfall intensity. Safety numbers were obtained for three different monthly rainfall intensities: 300 mm, 500 mm, and 700 mm. Considering the groundwater level and pore water pressures after rainfall effect; Slope stability analyses were performed using unsaturated shear resistance parameters. Factor of safety values were found as 1.70, 1.64, and 1.59, respectively.

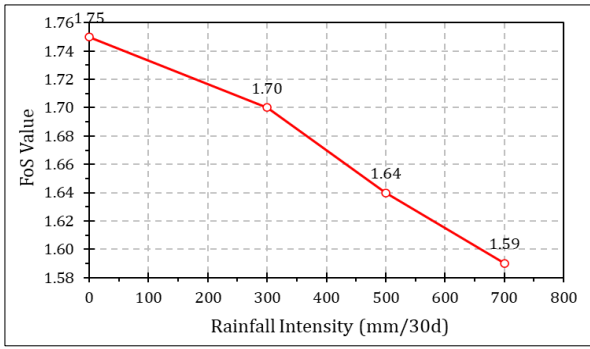


Figure 2. FoS value / Rainfall intensity graph

It was observed that the factor of safety number decreased while the rainfall intensity increased. In the Figure 3, the change in the factor of safety number depending on the rainfall intensity is seen clearly. Additionally, in Figure 4, percent decreases in the factor of safety number relative to the initial condition were shown. As it is seen in the Figure 4, 3.20%, 6.16%, and 9.08% decreases in the factor of safety number relative to the initial condition were observed under 300mm/30d, 500mm/30d and 700mm/30d of rainfall, respectively.

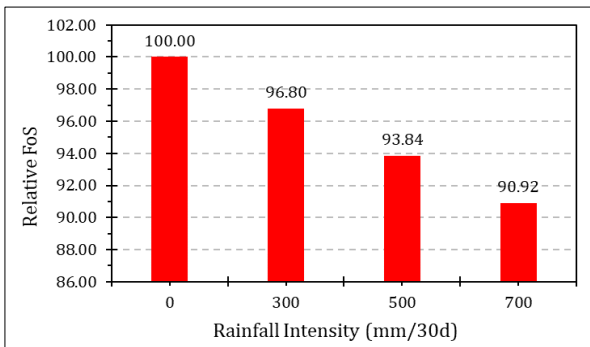


Figure 3. Percent FoS decreases relative to the initial value, depending on rainfall intensity

5.2. Effect of Rainfall Duration on Slope Stability

In order to see the effect of rainfall duration, the same amount of rainfall (300mm) was defined at different times as 3 days, 30 days, and 60 days.

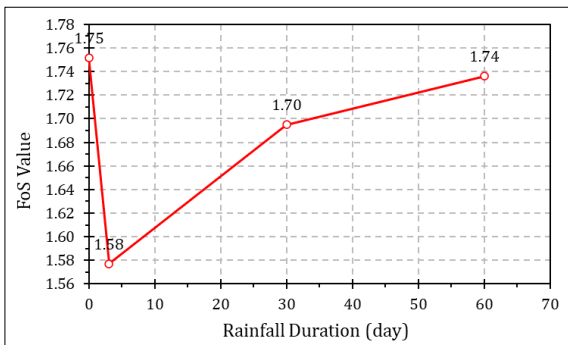


Figure 4. Factor of safety values after 300mm/3d, 300mm/30d, and 300mm/60d rainfall

As seen in the Figure 5, short time-heavy rainfalls affecting the slope stability more than long time-low density rainfalls. Additionally, in Figure 6, percent decreases in the factor of safety number relative to the initial condition were shown. As presented in the Figure 6, 9.99%, 3.25%, and 0.91% decreases in the factor of safety number relative to the initial condition were observed under 300mm/3d, 300mm/30d and 300mm/60d of rainfall, respectively. These results can be explained with the rapid decrease of the negative pore water pressure in the unsaturated soil.

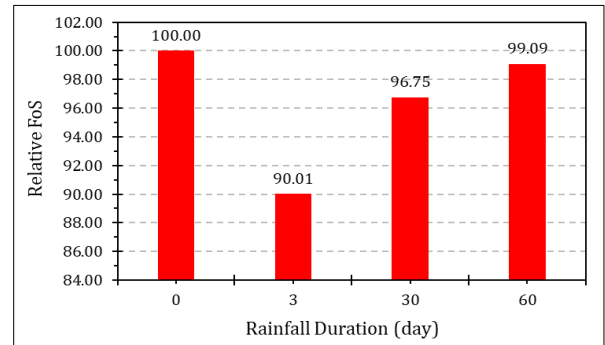


Figure 5. Percent FoS decreases relative to the initial value, depending on rainfall durations

5.3. Effect of Soil Permeability on Slope Stability

In this part, the effects of soil permeability on rainfall infiltration and consequently slope stability were investigated. Using different permeability values in the analyses, safety numbers were obtained after 300mm/30d rainfall. The permeability values which are used in the analyses are $k_1=5 \cdot 10^{-5}$, $k_2=1 \cdot 10^{-6}$, and $k_3=5 \cdot 10^{-7}$ m/sec.

In the Figure 7, the factor of safety changes while permeability of the soil decreases was presented. Additionally, in Figure 8, percent decreases in the factor of safety number relative to the k_1 (5.10-5m/sec) result were shown. As it is seen in the Figure 8, 6.48%, and 9.61% decrease in the factor of safety number relative to the k_1 result (1.76) were observed under 300mm/30d rainfall. This situation can be explained by the relationship between infiltration and drainage. In soils with very high permeability ($k_s > 10^{-4}$ m/sec), rapid drainage occurs simultaneously with infiltration and therefore pore water pressure does not rise. Due to this reason the factor of safety number not to be affected much by infiltration. On soils with intermediate permeability (10^{-4} m/s - 10^{-7} m/s) infiltration-drainage balance gains importance. As the permeability decreases in this range, accordingly the safety number decreases.

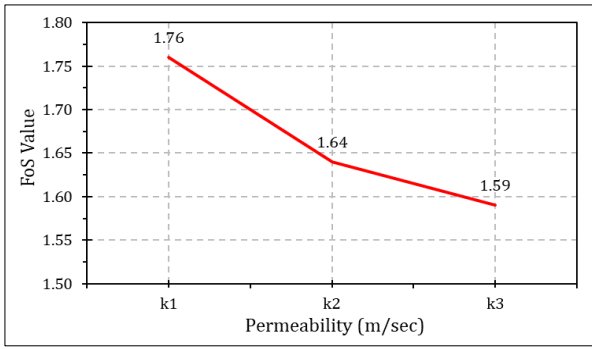


Figure 6. FoS number / Permeability graph

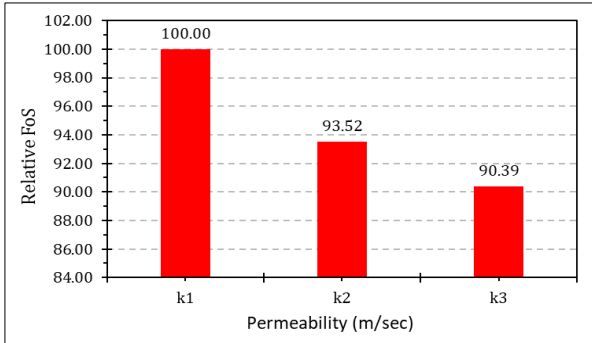


Figure 7. Percent FoS decreases relative to the first value, depending on the permeability

5.4. Effect of the Ground Water Table Change on Slope Stability

One of the noteworthy effects of rainfall is the change in groundwater level. A rise in the groundwater level may occur after rainfall, depending on the decrease in the negative pore water pressure (matric suction) of the soil, the shear strength that before rainfall of the soil decreases.

In this analysis, factor of safety numbers was obtained for 3 different groundwater levels in which, 16 m, 18 m, and 20 m above the lowest point of the slope model, in no rainfall conditions.

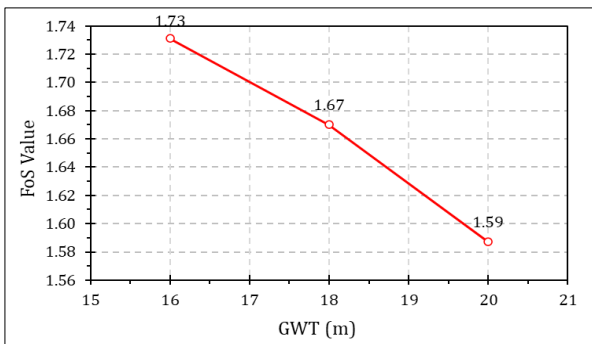


Figure 8. The change in the FoS values depending on GWT

As it is seen in the Figure 9, when the ground water table increase, factor of safety values decreases as well due to decrease in the matric

suction. Additionally, in Figure 10, percent decreases in the factor of safety number relative to the lowest GWT (16m) result were shown. 1.14%, 4.57%, and 9.14% decreases in the factor of safety number relative to initial value were observed.

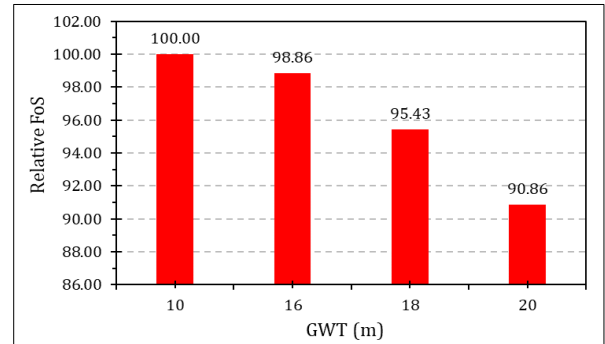


Figure 9. Percent FoS decreases relative to the initial value, depending on the GWT

5.5. Effect of Cohesion(c) on Slope Stability

In the analyses, the effect of the cohesion parameter on the slope stability was observed. Except cohesion, other parameters were kept constant in the analysis. Different factor of safety values was obtained for three different effective cohesion values of the unsaturated fill soil which are 15, 13 and 11(kPa).

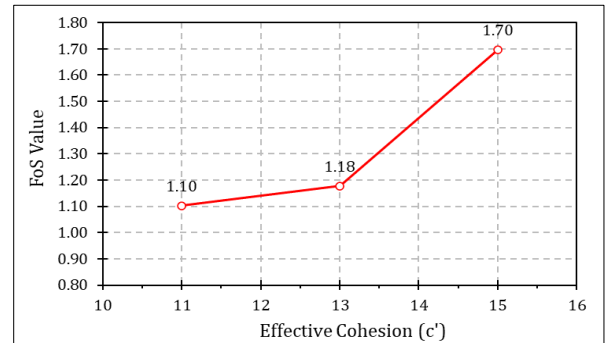


Figure 10. The change in the FoS values for different cohesion values

It is clearly seen in the Figure 11 that FoS increases with the increase in the effective cohesion. Additionally, in the Figure 12 percent decreases in the factor of safety number relative to the initial FoS value (1.75) were shown. 2.86%, 32.57%, and 37.14% decreases in the factor of safety number relative to the initial FoS value were observed. In order to evaluate the results, we can say that cohesion is a considerable soil parameter that affects the stability because the safety number was significantly reduced with a small reduction in cohesion.

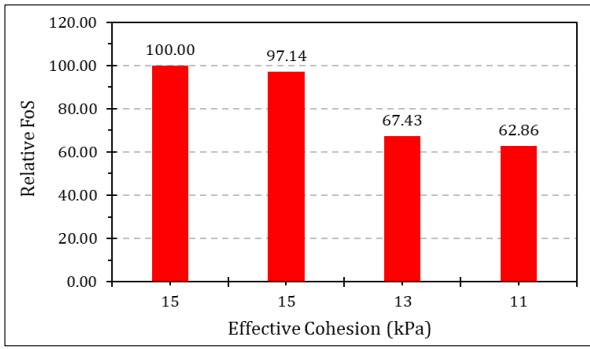


Figure 11. Percent FoS decreases relative to the initial value, depending on the effective cohesion

5.6. Effect of Internal Friction Angle on Slope Stability

In this analyses, effect of the internal friction angle in unsaturated soil on slope stability was investigated. Different factor of safety values was obtained for three different effective internal friction values of the unsaturated fill soil which are 14°, 12° and 10°. For these different internal friction angles, different ϕ_b values were calculated. The ϕ_b values calculated as 8.82°, 7.31°, and 6.08° for 14°, 12°, and 10° internal friction angles, respectively. Then, the new angles were used for each analysis.

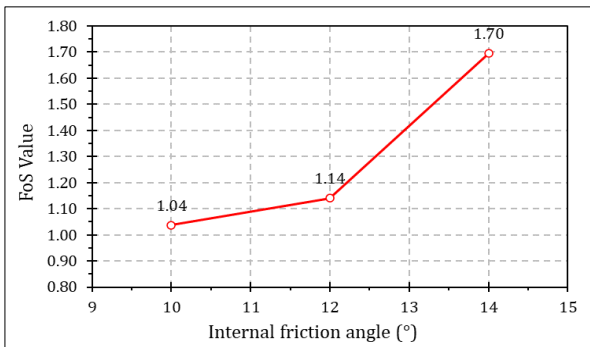


Figure 12. FoS number depending on internal friction angle

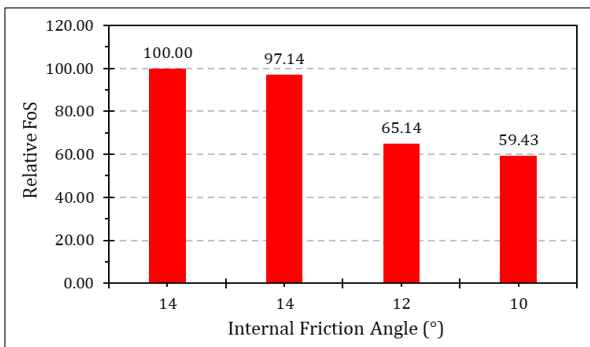


Figure 13. Percent FoS decreases relative to the initial value, depending on internal friction angle

In the Figure 13, it is seen that as the internal friction angle increases, the FoS values increases as

well. Additionally, in the Figure 14, percent decreases in the factor of safety number relative to the initial FoS value were shown. 2.86%, 34.86%, and 40.57% decreases in the factor of safety number relative to the initial FoS value were observed.

5.7. Effect of Slope Angle on Slope Stability

In these analyses, only effect of slope angle change on slope stability was investigated. During the previous analyses slope angle was 40°. This angle was increased from 40° to 45° and 50°. At the initial conditions, FoS values obtained as 1.75, 1.59, and 1.44 for 40°, 45°, and 50° slope angles, respectively. As seen in the Figure 15, after 300mm/30d rainfall, FoS values were obtained as 1.69, 1.54, and 1.38 for 40°, 45°, and 50° slope angles, respectively.

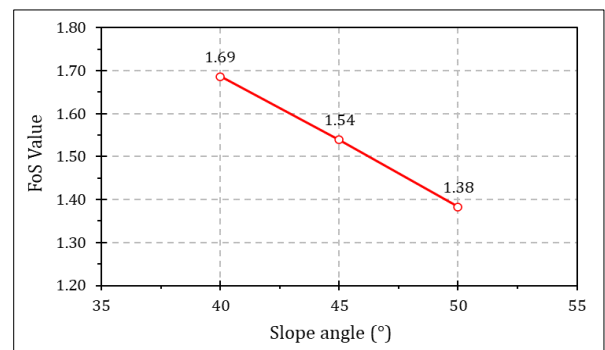


Figure 14. FoS values depending on slope angle

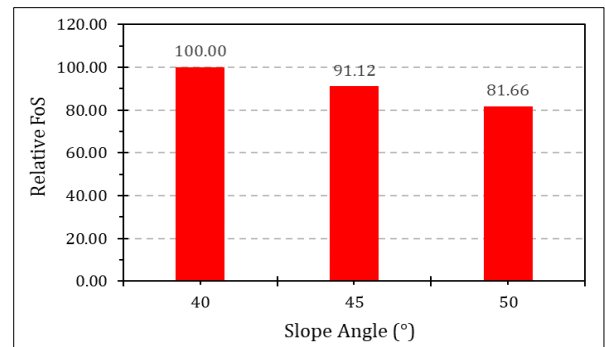


Figure 15. Percent FoS decreases relative to the first value, depending on slope angle

In the Figure 15, it is obviously seen that FoS values decreases as slope angle increases. For this reason, it can be said that slope angle is a significant factor on slope stabilities especially in rainy areas. Additionally, in the Figure 16, percent decreases in the factor of safety number relative to the FoS value of the 40° of slope angle were shown. 8.88%, and 18.34% decrease in the factor of safety number relative to the FoS value of the 40° of slope angle were observed.

6. CONCLUSION

The results showed that the rainfall intensity affects the stability of the slope significantly. Non-linear relationship between rainfall intensity and safety number was determined. As presented in the Table 3, while the rainfall intensity increases, the negative pore water pressure in the soil decreases nonlinearly, and consequently the factor of safety number of the slope similarly decreases.

Table 3. Rainfall intensity analysis results

Rainfall Intensity (mm/day)	FoS Value at Initial Condition	FoS Values After Rainfall	Percent Decrease Relative to Initial Condition
300	1.75	1.70	3.20
500		1.64	6.16
700		1.59	9.08

When the effects of rainfall duration on infiltration and accordingly slope stability were examined, it was seen that short-term heavy rainfall was more effective than long-term but relatively low-intensity rainfall. As seen in the Table 4, when 300 mm of rainfall fell on the soil in 3 days, a considerable decrease in the number of safeties were observed. These results can be explained with the rapid decrease of the negative pore water pressure in the unsaturated soil.

Table 4. Rainfall duration analyses results

Rainfall Duration (day)	FoS Value at Initial Condition	FoS Values After Rainfall (300mm)	Percent Decrease Relative to Initial Condition
3	1.75	1.58	9.99
30		1.70	3.25
60		1.74	0.91

It was further observed by different permeability analyses that when permeability decreased, the number of safeties also decreased. The analyses results are presented in the Table 5. This observation can be explained by the relationship between infiltration and drainage. In soils with very high permeability ($k_s > 10^{-4}$ m/sec), rapid drainage occurs simultaneously with infiltration and therefore pore water pressure does not rise. On soils with intermediate permeability (10^{-4} m/s - 10^{-7} m/s) infiltration-drainage balance gains importance. As the permeability decreases in this range, accordingly the safety number decreases.

Table 2. Permeability analyses results

Soil Permeability (m/sec)	FoS Value at Initial Condition	FoS Values After Rainfall (300mm)	Percent Decrease Relative to Initial Condition
5×10^{-5}	1.75	1.76	0
1×10^{-6}		1.64	6.48
5×10^{-7}		1.59	9.61

Likewise, it has been observed that the shear strength of the soil decreases, thus the safety number decreases with the rise of the groundwater level. When the initial conditions were examined, it was observed that as the groundwater level increased, the safety number decreased compared to the initial conditions due to the decrease in the matric suction values of the soil.

Table 3. GWT analyses results

Ground Water Table (m)	FoS Value at Initial Condition	FoS Values in no rainfall Condition	Percent Decrease Relative to Initial Condition
16	1.75	1.73	1.14
18		1.67	4.57
20		1.59	9.14

Furthermore, soil cohesion on slope stability was evaluated, and it was found that the shear strength of the soil decreases markedly with the reduction of the cohesion. Hence, factor of safety decreased. As presented in the Table 7, 32.57%, and 37.14% decreases which are remarkable decreases in accordance with other parameters, observed with the reduction of effective cohesion value.

Table 4. Effective cohesion analyses results

Effective Cohesion (c') (kPa)	FoS Value at Initial Condition	FoS Values After rainfall (300mm/day)	Percent Decrease Relative to Initial Condition
15	1.75	1.70	2.86
13		1.18	32.57
11		1.10	37.14

When the internal friction angle effect was evaluated. It has been found that the shear strength of the soil decreases with the reduction of the internal friction angle. Similar to the effective cohesion analyses results, 34.86% and 40.57% decreases seen due to reduction of internal friction angle value.

Table 5. Internal friction angle analyses results

Internal Friction Angle (°)	FoS Value at Initial Condition	FoS Values After rainfall (300mm/day)	Percent Decrease Relative to Initial Condition
14		1.70	2.86
12	1.75	1.14	34.86
10		1.04	40.57

Slope angle has a key role on slope stability. When the slope angle increased, it has been obtained that factor of safety decreased. Therefore, slope angle determinations must be done carefully on the related projects. In the Table 9, factor of safety changes and percent decreases relative to the 40° slope angle value is given. As seen in the Table 9, 8.88% and 18.34% decrements were observed due to 5° and 10° increments of the slope angle value.

Table 6. Slope angle of slope analyses results

Slope Angle of Slope (°)	FoS Values After rainfall (300mm/day)	Percent Decrease Relative to 40° Slope Angle
40	1.69	0
45	1.54	8.88
50	1.38	18.34

When the results of all analyses were evaluated, it was seen that the results were consistent with other studies in the literature.

Author Contributions

Furkan Veli Özçelik: Conceptualization, Methodology, Software. **Murat Ergenokon Selçuk:** Supervision, Reviewing, and Guiding.

Conflicts of Interest

The authors declare no conflict of interest.

REFERENCES

- Aslan Fidan, A. (2017). Doygun olmayan koşullarda yağış infiltrasyonu etkisindeki şevlerin stabilite analizi. (MSc thesis). Dicle University, Diyarbakır, Turkey (in Turkish).
- Au, S.W.C. (1998). Rain-induced slope instability in Hong Kong. *Engineering Geology*, 51(1), 1-36.
- Fredlund, D.G. (2012). Unsaturated soil mechanics in engineering practice. *Journal of geotechnical and geoenvironmental engineering*, 132(3), 286-321.
- GEOSLOPE (2012). Stability Modeling with Slope/w. Canada.
- GEOSLOPE (2015). Seepage Modeling with Seep/w.
- Jeong, S., Lee, K., & Kim, J. (2017). Analysis of Rainfall-Induced Landslide on Unsaturated Soil Slopes. *Sustainability*, 9(7), 1280.
- Karabulut, B. (2019). Yağış ile Sızmanın Şevlerin Stabilitesine Etkisi . (MSc thesis). Yıldız Technical University, İstanbul, Turkey (in Turkish).
- Önalp, A., & Arel, E. (2013). Geoteknik bilgisi I zeminler ve mekaniği çözümlü problemlerle. Birsen Yayınevi, İstanbul, 461.
- Tetik, A. (2020). Yağış etkisi altındaki şevlerin stabilite analizi (MSc thesis). Manisa. Celal Bayar University, Manisa, Turkey (in Turkish).
- Wang, Y., Chai, J., Cao, J., Qin, Y., Xu, Z., & Zhang, X. (2020). Effects of seepage on a three-layered slope and its stability analysis under rainfall conditions. *Natural Hazards*, 102(3), 1269-1278.



© Author(s) 2021. This work is distributed under <https://creativecommons.org/licenses/by-sa/4.0/>

Analysis of the threat of forest fires to ancient cities by GIS and Remote Sensing methods

Ezgi Tükel*¹, Kaan Kalkan²

¹Eskişehir Technical University, Department of Remote Sensing and Geographic Information Systems, Eskişehir, Turkey

²TÜBİTAK Space Technologies Research Institute, Ankara, Turkey

Keywords

Forest Fires
Archaeological Site
Fire Risk
Burn Severity
Landsat-8

ABSTRACT

Forest fires have been more common in recent years and caused extensive damage. Not only settlements and natural life but also historical places and ancient cities are at risk of forest fires. This study discussed forest fires in Turkey in the summer of 2021. Forest fire risk classifications were determined using Landsat-8 images. The Normalized Burn Ratio (NBR) and Differenced Normalized Burn Ratio (dNBR) indices were used to assess the area impacted by fire and to create fire risk classes. Furthermore, the burned and unburned areas in different zones from the Amos ancient city in the Marmaris were calculated using remote sensing methods. Thus, areas that should be protected from the fire were determined in future studies for fire risk areas.

1. INTRODUCTION

Forest fires are becoming more frequent with increasing global warming worldwide (Hantson et al., 2016). Many forest fires occurred in the summer of 2021, and Turkey's total burned area reached 204,408 hectares (EFFIS, 2021). Forest fires have a natural effect on occurrences, can rejuvenate forests, and eliminate illnesses and other dangerous risks. On the other hand, they may negatively affect settlements and natural life (Daşdemir et al., 2021; Nuthammachot and Stratoulis, 2021). Forest fires pose a threat not only to natural vegetation and settlements but also to historical and archaeological sites (Dimitrakopoulos et al., 2002).

Several studies focus on the conservation of National Park and ancient site regions. Portugal's Herdade da Contenda region is a national hunting area, and a conservation-integration plan was studied using remote sensing methods (Teodoro et al., 2015). Furthermore, to assist in the conservation plan, multi-criteria decisions and buffer zone management methods were applied to protected areas (Geneletti and Duren, 2008; Hjortsø et al., 2006). On the other hand, forest fire risk zone mapping can create to understand the fire impact on

natural and cultural heritage areas (Nikhil et al., 2021).

In the literature, there are many different fire detection studies using UA and GIS techniques. Previously implemented fire detection algorithms using remote sensing are generally developed and tuned for regional, continental, and global applications (Flasse and Ceccato, 1996). "Burn severity" is a term used to describe the physical, chemical, and biological alterations for the purpose of identifying the burned area after a fire (White et al., 1996). Furthermore, several techniques are used to create fire risk maps, including weighted registration, machine learning, deep learning, and frequency ratio (Javad et al., 2014; Tien Bui et al., 2017; Stroppiana et al., 2021). On the other hand, the land surface temperature (LST) is related to burned areas based on the severity of the forest fire (Vlassova et al., 2014).

Several remote sensing methods are used to understand the forest fire severity. Some of these are based on multi-date change detection such as differenced Normalized Burn Ratio (dNBR), the soil-adjusted vegetation index, and burned area index (Hall et al., 2008; Marino et al., 2016; Smith et al., 2010). Forest fire risk and hazard maps are crucial for the environmental management of forest regions

* Corresponding Author

(ezgitukel@eskisehir.edu.tr) ORCID ID 0000-0002-8675-2128
(kaankalkan@gmail.com) ORCID ID 0000-0002-2732-5425

Received: 05/07/2022; Accepted: 31/08/2022

Cite this article

Tükel E., & Kalkan K. (2022). Analysis of the threat of forest fires to ancient cities by GIS and Remote Sensing methods. Turkish Journal of Geosciences 3(2), 58-63.

and for establishing long-term strategic fire prevention plans (Akay and Şahin, 2019; Eugenio et al., 2016). Remote sensing methods enable the analysis, display, and presentation of fire severity and risk classification (Boer et al., 2008; Değerliyurt and Çabuk, 2015; Sandamali and Chaturanga, 2021).

The primary purpose of this study is to examine the impact of fire risk on the ancient city and its environment. In this study, forest fires covering the Aegean and Mediterranean regions of Turkey in 2021 were discussed. The Amos ancient city in the Marmaris district was chosen as the study area since it is one of the most damaged areas by the fire. The fire around the ancient city of Amos started on 4 August 2021 and was brought under control on 5 August 2021 with the intervention of the fire brigade (Url-1, Url-2).

In this study, dNBR, which is the most common remote sensing method, was used to determine fire severity and fire risk areas at different distances from the ancient city point were defined to assess the threat and risk of fire to the ancient city of Amos. Moreover, according to the forest fire severity map created in the study we tried to understand how much the ancient city was affected by the forest fire.

The remainder of the study is organized as follows. Section 2 presents the methodology, including the study area, the satellite data sources, and the description of the analysis indexes. Analyses are described in Section 4. Section 3 concludes the study.

2. METHODOLOGY

2.1. Study Area and Materials

Marmaris is one of the districts of Muğla province. The area of the district is 963.73 km²; 80% is forestland, 5% is agricultural land, and a coastline of 451.72 km (Figure 1). Amos ancient city was selected as a study area (Figure 2). On the southwest side of contemporary Turunç, Marmaris, Amos is one of the Rhodian antiquities located on the Asarcık hill (Gürbüz, 2021; Yaman, 2022).

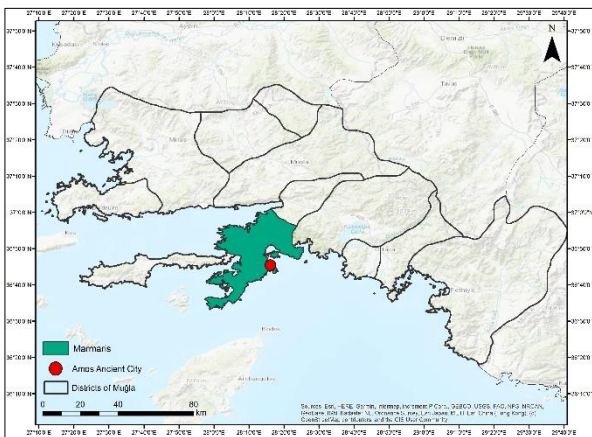


Figure 1. Study area

Landsat-8 images were used as satellite images in this study. Landsat-8 images were obtained from USGS (United States Geological Survey) websites in 2022 and has 11 bands with developed band combinations (Acharya and Yang, 2015). Two images were acquired, one from 2020 and the other from 2021 (Table 1). Moreover, ancient site point data was obtained from QGIS Open Street Map Plugin. According to Turkish news sources, the Amos ancient city was chosen for investigation since Amos was under the threat of forest fires (Url-2).

Table 1. Dates of Landsat images

Landsat Images	Date
LC08_L1TP_180034_20201224_02_T1	24.12.2020
LC08_L1TP_180034_20210821_02_T1	21.08.2021

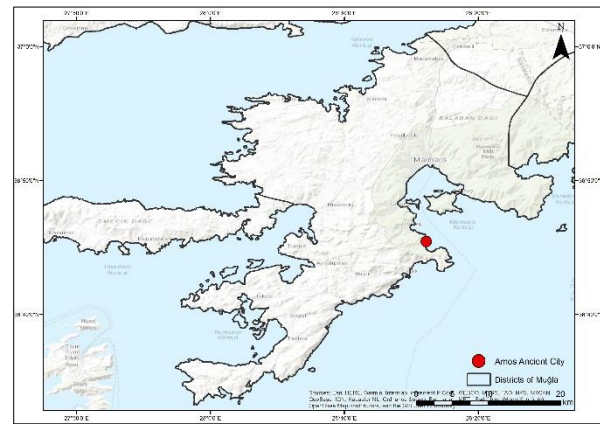


Figure 2. Location of Amos Ancient City

2.2. Method

We focused on NBR and dNBR as indices to evaluate burned areas in satellite images. First, the radiometric correction was applied to bands of Landsat-8 images. NBR analysis was performed on the image to estimate the intensity of the burn severity areas from before and after forest fire images. NBR is calculated as a ratio between the near-infrared (NIR) and shortwave infrared (SWIR) values. Furthermore, dNBR observes changes between two dates (Stankova and Nedkov, 2015).

$$NBR = (NIR - SWIR) / (NIR + SWIR) \quad (1)$$

$$dNBR = [Pre - fire NBR - Post - fire NBR] \quad (2)$$

For the Landsat 8 image, the NIR value corresponds to Band 5, while the SWIR value corresponds to Band 7 (Url-3). For Landsat 8:

$$NBR = (Band 5 - Band 7) / (Band 5 + Band 7) \quad (3)$$

This study used Band 7 of Landsat-8, which detects the wavelength between 2100 and 2290 in the infrared region. On the other hand, Band 6 is at a lower wavelength and was not included in the study.

After the NBR analysis on Band 5 and Band 7 for the dates before and after the fire, dNBR analysis was applied to understand the burn severity of forests between the two dates. In a study of fire escape scenarios, the distances between the fire starting and end points were determined as 861 meters, 935 meters and 1175 meters (Castro-Basurto et al., 2021). Therefore, in this study, escape distances were determined approximately, to observe the fire threat to the Amos ancient city, 500 meters, 1 kilometer, and 2 kilometers buffer zones were applied to the point of the ancient city. In this study, the effect of fire severity in the determined buffer zones based on the area was examined. Moreover, projection systems were defined as a UTM Zone 35 in the QGIS. Figure 3 shows the methodology flow chart of the study.

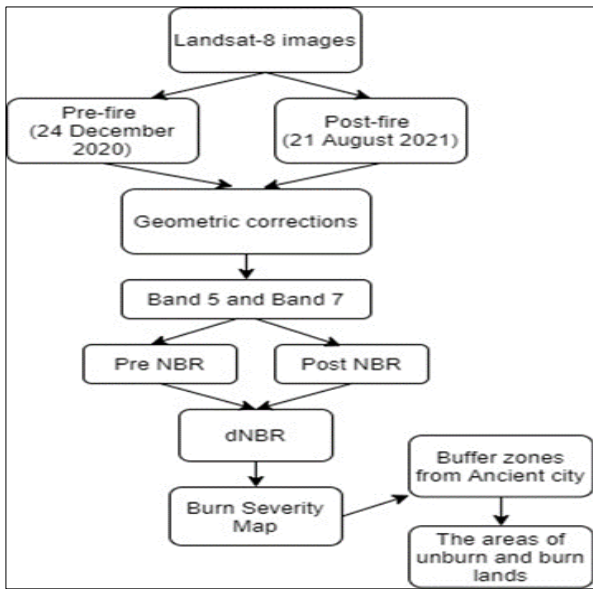


Figure 3. Methodology flow chart

3. RESULTS AND DISCUSSION

The burn severity indices values were classified as shown in Table 2. Severity indices are based on previous studies (Giddey et al., 2022; Konkathi and Shetty, 2019). The result shows the fire intensity map after applying the NBR and dNBR analyzes. Moreover, the area with high and severe burn areas are close to the Amos ancient city (Figure 4).

Table 2. Classified Burn and Unburn Areas

Severity Level	Values
Unburn Area	<0.099
Low Burn Area	0.1-0.27
Moderate Burn Area	0.27-0.54
High Burn Area	0.54-0.72
Severe Burn Area	>0.72

In Marmaris, there are 67.53 km² of unburned land, 345.28 km² of low burn, 326.30 km² of moderate burn, 54.74 km² of high burn, and 38.66

km² of severe burn. Distance buffers of 500 meters, 1 kilometer, and 2 kilometers were applied to the unburn and burn areas of the ancient city (Figure 5).

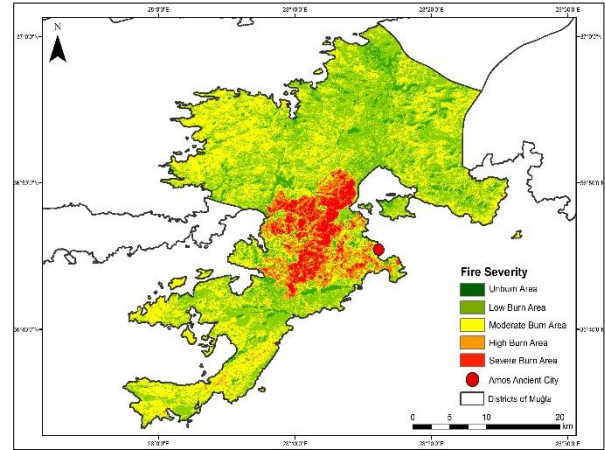


Figure 4. The dNBR results

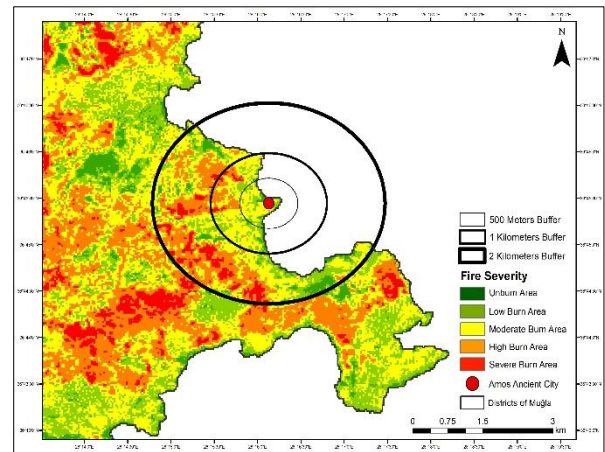


Figure 5. Buffer zones of Amos ancient city

The severe burn area of 500 meters from the Amos ancient city is 0.02 km², which is 0.05% of the Marmaris severe burn area. At a distance of 1 kilometer, the severe burn area is %0.18 of the district's severe burned area. Moreover, at a distance of 2 kilometers, the severe burn area is %1.26 of the Marmaris severe burned area. 2 kilometers from the Amos ancient city, the burn areas are respectively low burn area (2.3 km²), moderate burn area (1.7 km²), high burn area (1.04 km²) and severe burn area (0.49 km²). Furthermore, the Amos ancient city's unburn area is 0.6 km² in 2 kilometers.

According to the dNBR result, which is the difference between pre-fire and post-fire areas, there are different burn ratio classes at different distances to the Amos ancient city. While the area of the severe burn area zone of 1-kilometer distance to the ancient city is fewer, the area of the severe burn area zone of 2 kilometers distance to the ancient city is increasing. However, in the area zone of 500 meters and 1 kilometer, the moderate burn area is more than other classes (Table 3).

Table 3. Burn and unburn areas of buffers of the Amos ancient city

Landsat Images	In 500 meters	In 1 kilometer	In 2 kilometers
Unburn area(km ²)	0.01	0.15	0.6
Low burn area (km ²)	0.05	0.61	2.3
Moderate burn area (km ²)	0.14	0.42	1.7
High burn area (km ²)	0.01	0.16	1.04
Severe burn area (km ²)	0.02	0.07	0.49

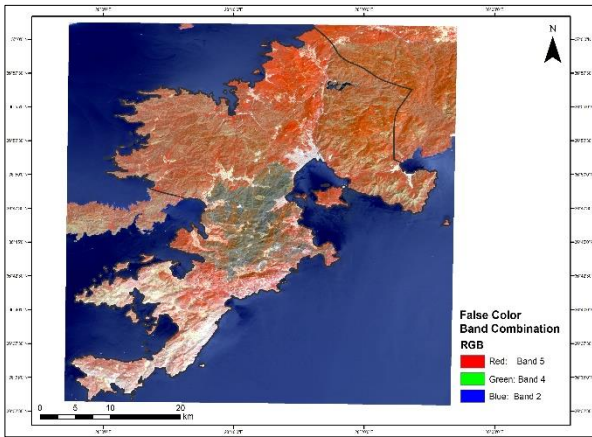


Figure 6. False color band combination

The false color band combination was applied to observe the vegetation change in the burned areas (Figure 6). Accordingly, 5-4-2 Bands were selected for Landsat 8. As a result, vegetation decreased in the severe burned forest area.

4. CONCLUSIONS

Previous studies focused on fire management in ancient cities and national parks (Humphrey et al., 2021; Roos et al., 2021). Moreover, forest fire severity and forest fire susceptibility studies were implemented for national parks using remote sensing methods (Gigović, 2019; Rozario, 2018).

However, there are no comprehensive studies in the literature that analyze the effects of forest fires on ancient cities with remote sensing methods. The study aims to determine the fire risk areas of the ancient city and its environment in Turkey in the summer of 2021 forest fires. Furthermore, forest risk areas were evaluated from Amos ancient city at different distances. According to this, severe burn areas increased by 2 kilometers from the Amos ancient city.

This study evaluated the impact using remote sensing and GIS methods. Moreover, conservation management can be created by calculating the

burned areas and evaluating the situation around the ancient city.

The limitation of the study is that there is no data on the borders of Amos ancient city, so the fire risk zones were calculated by measuring the buffer from the point. On the other hand, this study can benefit future forest fire management and long-term strategic fire prevention plans.

Acknowledgement

We thank our three peer reviewers for pointing out areas where the text needed clarification.

Author Contributions

Ezgi Tükel: Methodology, Software, Validation, Formal analysis, Writing-Original Draft, Visualization. **Kaan Kalkan:** Conceptualization, Methodology, Writing- Reviewing and Editing.

Conflicts of Interest

The authors declare no conflict of interest.

REFERENCES

- Acharya, T.D., & Yang, I. (2015). Exploring Landsat 8. *International Journal of IT, Engineering and Applied Sciences Research (IJIEASR)*, 4(4), 4-10.
- Akay, A.E., & Şahin, H. (2019). Forest fire risk mapping using GIS techniques and AHP method: a case study in Bodrum (Turkey). *European Journal of Forest Engineering*, 5(1), 25-35.
- Boer, M.M., Macfarlane, C., Norris, J., Sadler, R.J., Wallace, J., & Grierson, P.F. (2008). Mapping burned areas and burn severity patterns in SW Australian eucalypt forest using remotely-sensed changes in leaf area index. *Remote Sensing of Environment*, 112(12), 4358-4369.
- Castro-Basurto, K., Jijon-Veliz, F., Medina, W., & Velasquez, W. (2021). Outside dynamic evacuation routes to escape a wildfire: A prototype app for forest firefighters. *Sustainability*, 13(13), 7295.
- Daşdemir, İ., Aydın, F., & Ertuğrul, M. (2021). Factors affecting the behavior of large forest fires in Turkey. *Environmental Management*, 67(1), 162-175.
- Değerliyurt M., & Çabuk S. (2015). Defining geography with geographical information systems Eastern. *Geogr J* 20:37-48.
- Dimitrakopoulos, A.P., Mitrakos, D., & Christoforou, V. (2002). Concepts of wildland fire protection of cultural monuments and national parks in Greece. Case study: Digital telemetry networks




- at the forest of Ancient Olympia. *Fire Technology*, 38(4), 363-372.
- EFFIS (European Forest Fire Information System), 2021. EFFIS Annual Country Statistics for TR – Turkey, retrieved from <https://effis.jrc.ec.europa.eu/apps/effis.statisticks/effisestimates>, access date: 12/01/2022.
- Eugenio, F.C., Dos Santos, A.R., Fiedler, N.C., Ribeiro, G.A., Da Silva, A.G., Dos Santos, Á.B., Paneto G.G., & Schettino, V.R. (2016). Applying GIS to develop a model for forest fire risk: A case study in Espírito Santo, Brazil. *Journal of environmental management*, 173, 65-71.
- Flasse, S.P., & Ceccato, P. (1996). A contextual algorithm for AVHRR fire detection. *International Journal of Remote Sensing*, 17(2), 419-424.
- Geneletti, D., & Van Duren, I. (2008). Protected area zoning for conservation and use: A combination of spatial multicriteria and multiobjective evaluation. *Landscape and urban planning*, 85(2), 97-110.
- Giddey, B.L., Baard, J.A., & Kraaij, T. (2022). Verification of the differenced Normalised Burn Ratio (dNBR) as an index of fire severity in Afrotropical Forest. *South African Journal of Botany*, 146, 348-353.
- Gigović, L., Pourghasemi, H. R., Drobnjak, S., & Bai, S. (2019). Testing a new ensemble model based on SVM and random forest in forest fire susceptibility assessment and its mapping in Serbia's Tara National Park. *Forests*, 10(5), 408.
- Gürbüz, M. (2021). Amos' ta Yeni Araştırmalar ve Bulgular. *Cedrus*, 9, 219-249.
- Hall, R. J., Freeburn, J.T., De Groot, W.J., Pritchard, J.M., Lynham, T.J., & Landry, R. (2008). Remote sensing of burn severity: experience from western Canada boreal fires. *International Journal of Wildland Fire*, 17(4), 476-489.
- Hantson, S., Pueyo, S., & Chuvieco, E. (2016). Global fire size distribution: from power law to log normal. *International journal of wildland fire*, 25(4), 403-412.
- Hjortsø, C. N., Stræde, S., & Helles, F. (2006). Applying multicriteria decision-making to protected areas and buffer zone management: A case study in the Royal Chitwan National Park, Nepal. *Journal of forest economics*, 12(2), 91-108.
- Humphrey, G. J., Gillson, L., & Ziervogel, G. (2021). How changing fire management policies affect fire seasonality and livelihoods. *Ambio*, 50(2), 475-491.
- Javad, M., Baharin, A., Barat, M., & Farshid, S. (2014). Using frequency ratio method for spatial landslide prediction. *Research Journal of Applied Sciences, Engineering and Technology*, 7(15), 3174-3180.
- Konkathi, P., & Shetty, A. (2019). Assessment of burn severity using different fire indices: A case study of Bandipur National Park. In *2019 IEEE Recent Advances in Geoscience and Remote Sensing: Technologies, Standards and Applications (TENGARSS)* (pp. 151-154) IEEE.
- Marino, E., Guillén-Climent, M., Ranz Vega, P., & Tomé, J. (2016). Fire severity mapping in Garajonay National Park: Comparison between spectral indices. *Flamma: Madrid, Spain*, 7, 22-28.
- Nikhil, S., Danumah, J. H., Saha, S., Prasad, M. K., Rajaneesh, A., Mammen, P. C., ... & Kuriakose, S. L. (2021). Application of GIS and AHP method in forest fire risk zone mapping: a study of the Parambikulam tiger reserve, Kerala, India. *Journal of Geovisualization and Spatial Analysis*, 5(1), 1-14.
- Nuthammachot, N., & Stratoulis, D. (2021). Multicriteria decision analysis for forest fire risk assessment by coupling AHP and GIS: method and case study. *Environment, Development, and Sustainability*, 23(12), 17443-17458.
- Roos, C. I., Swetnam, T.W., Ferguson, T.J., Liebmann, M. J., Loehman, R.A., Welch, J.R., ... & Kiahtipes, C.A. (2021). Native American fire management at an ancient wildland-urban interface in the Southwest United States. *Proceedings of the National Academy of Sciences*, 118(4), e2018733118.
- Rozario, P.F., Madurapperuma, B.D., & Wang, Y. (2018). Remote sensing approach to detect burn severity risk zones in Palo Verde National Park, Costa Rica. *Remote Sensing*, 10(9), 1427.
- Sandamali, K.U., & Chathuranga, K.A.M. (2021). Quantification of Burned Severity of the Forest Fire using Sentinel-2 Remote Sensing Images: A Case Study in the Ella Sri Lanka. Research and Reviews: *Journal of Environmental Sciences*, 3(3), 1-12.
- Smith, A. M., Eitel, J.U., & Hudak, A.T. (2010). Spectral analysis of charcoal on soils: Implications for wildland fire severity mapping methods. *International Journal of Wildland Fire*, 19(7), 976-983.

- Stankova, N., & Nedkov, R. (2015). Monitoring forest regrowth with different burn severity using aerial and Landsat data. In *2015 IEEE International Geoscience and Remote Sensing Symposium (IGARSS) IEEE*.
- Stroppiana, D., Bordogna, G., Sali, M., Boschetti, M., Sona, G., & Brivio, P.A. (2021). A Fully Automatic, Interpretable and Adaptive Machine Learning Approach to Map Burned Area from Remote Sensing. *ISPRS International Journal of Geo-Information*, 10(8), 546.
- Teodoro, A., Duarte, L., Sillero, N., Gonçalves, J. A., Fonte, J., Gonçalves-Seco, L., Pinheiro da Luz, L.M., & Dos Santos Beja, N.M.R. (2015). An integrated and open source GIS environmental management system for a protected area in the south of Portugal. In *Earth Resources and Environmental Remote Sensing/GIS Applications VI* (Vol. 9644, pp. 143-154). SPIE.
- Tien Bui, D., Bui, Q.T., Nguyen, Q.P., Pradhan, B., Nampak, H., & Trinh, P.T. (2017). A hybrid artificial intelligence approach using GIS-based neural-fuzzy inference system and particle swarm optimization for forest fire susceptibility modeling at a tropical area. *Agricultural and Forest Meteorology*, 233, 32-44.
- Vlassova, L., Pérez-Cabello, F., Mimbbrero, M.R., Llovería, R.M., & García-Martín, A. (2014). Analysis of the relationship between land surface temperature and wildfire severity in a series of landsat images. *Remote Sensing*, 6(7), 6136-6162.
- White, J.D., Ryan, K.C., Key, C.C., & Running, S.W. (1996). Remote sensing of forest fire severity and vegetation recovery. *International Journal of Wildland Fire*, 6(3), 125-136.
- Yaman, A. (2022). Amos arkeolojik yüzey arařtırmalarında ele geen seramikler. *Olba*, 30, 113-127.
- Url-1: <https://www.haberturk.com/mugla-haberleri/89560498-tarihi-amos-antik-kenti-cevresindeki-yangina-toma-mudahalesi> (last accessed 05.08.2022)
- Url-2: <https://www.trthaber.com/haber/turkiye/ma-rmaristeki-yangin-amos-antik-kentine-ilerliyor-599654.html> (last accessed 12 June 2022)
- Url-3: <https://www.usgs.gov/landsat-missions/landsat-normalized-burn-ratio> (last accessed 12 June 2022)



© Author(s) 2021. This work is distributed under <https://creativecommons.org/licenses/by-sa/4.0/>

Application of Remote Sensing and GIS techniques for detecting burned areas and severity. A case study of the National Park "Dajti Mountain", Albania

Edmond Pasho*¹, Arben-Q. Alla¹, Ernest Ramaj¹

¹Universiteti Bujqësor i Tiranës, Fakulteti i Shkencave Pyjore, Departamenti i pyjeve, Tirana, Albania Country

Keywords

Forest
dNBR
Landsat 8
NDVI
EVI

ABSTRACT

Assessment of forest areas affected by wildfire is crucial for designing appropriate management strategies to support post-wildfire restoration. This study integrates Remote Sensing and GIS data to map burned areas and severity, and regeneration of vegetation in a Mediterranean forest type ecosystem (National Park "Dajti Mountain", NPDM), in Albania. Landsat 8 satellite imagery was employed to calculate various spectral indices such as the Normal Burn Ratio Index (NBR), NBR2, the Normalized Difference Vegetation Index (NDVI) and the Enhanced Vegetation Index (EVI). Burn severity levels were defined by using the dNBR thresholds developed by Key and Benson (2006). The accuracy of burn severity map produced was evaluated by relating field-based Composite Burn Index (CBI) and satellite-derived metrics (dNBR) from Landsat-8. By means of dNBR and dNBR2 we detected and mapped several burned forest areas within the NPDM, at the sites of Shkallë, Qafëmolle, Ibë, Tujan, Derje, Selbë, Surrel and Dajt, which were affected by wildfire during the year 2017. The dNBR produced the best results for burned areas mapping and burn severity assessment (91.7%) over the dNBR2 (89.8%). The dNBR and dNBR2 index maps showed that a total of 103.59 and 105.72 hectares of forests was affected by wildfire. Areas with different levels of burn severity were detected: 17.29 and 23.80% unburned, 43.36 and 45% low, 15.11 and 12.13% moderate, 24.93 and 21.2% high. Overall, the dNBR2 index produced lower percentages of wildfire-affected areas at high and moderate rates compared to the dNBR index while for unburned areas the dNBR2 index resulted in higher percentages. Vegetation recovery during the subsequent growing season was generally good as revealed by the high dNDVI and dEVI values, indicating the reactivation of photosynthetic activity. This information is useful for forest managers/specialists to design relevant strategies for the proper rehabilitation/management of burned forest areas in the future.

1. INTRODUCTION

Wildfire is considered any non-structured fire, other than prescribed fire, that occurs in the wildland (Firewise, 1998). Wildfires worldwide are affecting large areas and consequently are associated with negative impacts on forest ecosystems, such as: desertification, soil erosion, loss of water supply, biodiversity, biological functions which follow with large socio-economic losses, contribute to deforestation, greenhouse gas emissions, and also harm human well-being (Mallinis et al., 2018). The increasing frequency and intensity of wildfires has led to an increase in the

need to monitor them but also to assess areas damaged by wildfire through modern techniques including mapping with Remote Sensing and GIS methods. Satellite images have been used to detect changes in vegetation response to light spectrum in different spectral bands where these changes are reflected (Warner et al., 2017). Data provided by satellite images are very important for natural resource managers to understand and evaluate the effects of wildfires on the ecosystem as well as the impact of environmental changes on the ecological functioning of the ecosystem (Morgan et al., 2014). Accurate and rapid mapping of burned areas is essential to support their management

* Corresponding Author

Cite this article

(mondipasho@gmail.com) ORCID ID 0000-0001-5699-4858
(benialla@gmail.com) ORCID ID 0000-0002-6937-2940
(nestiramaj@gmail.com) ORCID ID 0000-0002-9740-898X

Pasho, E., Q-Alla, A., & Ramaj, E. (2022). Application of Remote Sensing and GIS techniques for detecting burned areas and severity. A case study of the National Park "Dajti Mountain", Albania. Turkish Journal of Geosciences 3(2), 64-74.

Received: 31/07/2022; Accepted: 21/10/2022

/rehabilitation, to calculate environmental damage, to define planning/management strategies and to monitor vegetation regeneration. Given the time and field efforts of wildfire management as well as the permanent and temporary impacts that fire cause on the ecosystem, Remote Sensing has become a reliable and applicable alternative for assessing the extent of wildfires (Lentile et al., 2006).

The most widely used method for evaluating wildfire impacts in the field is the Composite Burn Index (CBI) developed by Key and Benson, (2006). This field protocol, has shown good correlation with the spectral reflectance recorded from remote sensing images (Key and Benson, 2006; Mallinis et al., 2018). Several methods have been developed for mapping wildfire-affected areas from multi-temporal or single post-wildfire satellite images (Hudak et al., 2007; Escuin et al., 2008). These methods comprise a variety of spectral indices (e.g., NDVI, EVI, NBR, NBR2, MIRBI, BIAS2, BAI, etc.) covering the visible/NIR, the NIR/short SWIR and the short SWIR/long SWIR spectral spaces (Hu et al., 2021; Sirin and Medvedeva, 2022). However, the Normalized Burn Ratio difference (dNBR, dNBR2) and the Normalized Difference Vegetation Index (NDVI) have shown a good correlation with wildfire severity and therefore have been widely used for estimating burn severity and vegetation regeneration (Key and Benson, 2006; Mallinis et al., 2018; Atak and Tonyaloğlu, 2020). The ability of dNBR index to differentiate wildfire effects on vegetation is strongly related to the contrasting signal in NIR and SWIR reflectance bands provided by healthy versus wildfire-disturbed vegetation (Saulino et al., 2020). Remote sensing burn severity indices are able to rapidly and accurately detect burned forest areas which is crucial for post-wildfire management practices, especially in spatial heterogeneous and prone to wildfire Mediterranean forest ecosystems. During the year 2017, in several Mediterranean countries large forest areas were affected by wildfires (San-Miguel-Ayanz et al., 2018).

This is also the case of Albania where in 2017 have been reported many wildfires all over the country. These wildfires occurred repeatedly, mostly on shrublands and less in high forests. In most cases, causes of forest fires remain unknown but it is believed that they are human set wildfires. Apart from many shrub species, considerable areas of *Pinus nigra* and *Fagus sylvatica* forests were burned all over the country causing high economic and ecological damage (Forestry Sector Study Report, 2021).

The aim of this study was to evaluate the environmental impacts of wildfires that occurred during year 2017 in national park "Dajti mountain" (NPDM), region of Tirana, Albania, by means of Remote Sensing and GIS data. More specifically, it was intended to assess forest areas affected by wildfire, evaluate burn severity and the current state of vegetation (regeneration) in the affected areas. The objectives of this study were: (1) to produce burned area and severity maps of National Park "Dajti Mountain" by means of dNBR and dNBR2 indices and assess their accuracy, (2) to identify the most capable spectral index for evaluating wildfire severity and vegetation regeneration, (3) to evaluate the current state of vegetation (regeneration) in affected areas through the use of NDVI and EVI vegetation indices maps.

2. METHOD

2.1. Study Area

Study area is located about 5 km North-East of Tirana and covers the entire territory of National Park "Dajti Mountain" (NPDM) as well as areas around it (Figure 1). NPDM is affected by the Mediterranean pre-mountain and mountain climate characterized by relatively cold and humid autumn and winter while spring and summer are drier and hotter.

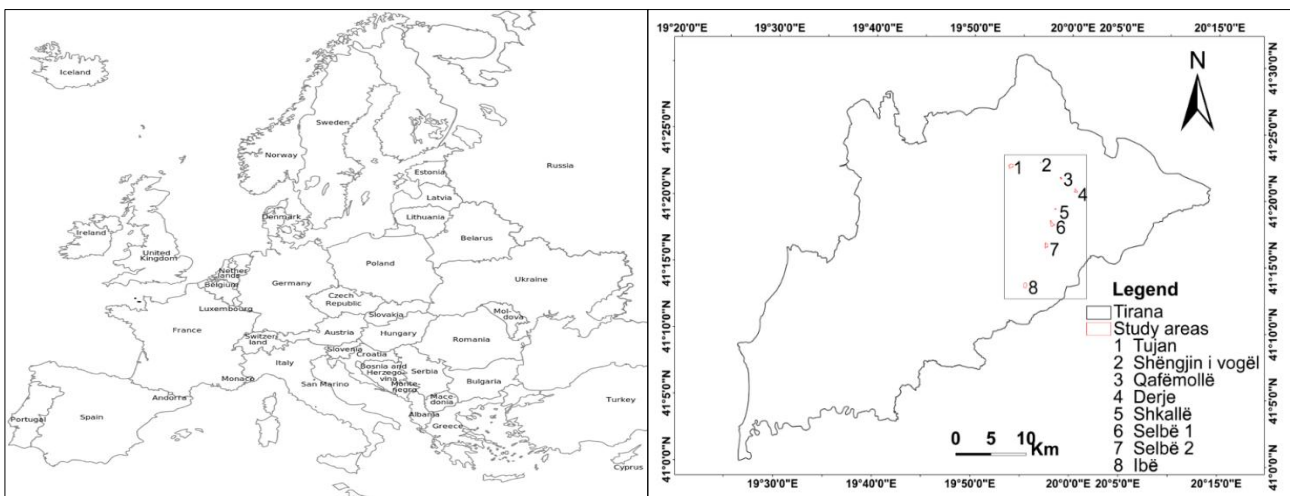


Figure 1. Map of Europe (left) and the study area located in north-east of Tirana (right). Red perimeter delineate the burned areas located within the national park "Dajti Mountain"

Average annual temperatures range from 15°C to 22°C. Nearly 70% of the annual precipitation falls in winter where the maximum rainfall reaches up to 237 mm per day (Bruci, 2007). The elevation ranges between 650m and 1613m, whereas the slope varies between 5% -70%. The park is characterized by fragmented and rugged topography which creates favorable conditions for a great diversity of ecosystems. Generally, NPDM is dominated by grey dark soils which are distributed at altitudes of 900-1600 m above sea level, but also by brown soils up to 900 m. The vegetation is characterized by evergreen species such as *Arbutus unedo*, *Erica arborea* and *Quercus ilex* and deciduous species such as *Fagus sylvatica*, *Quercus frainetto*, *Quercus cerris*, etc, and shrubs *Carpinus orientalis*, *Corylus avellana*, etc. NPDM is fire prone area where wildfires are occurring frequently every year. In particular, the year 2017 was characterized by extensive burning at the NPDM, including large and small burned areas with different levels of burn severity. Most wildfires occur during the dry season, from June to August, when vegetation contributes to accumulation of dry fuels that are easily combustible (Forestry Sector Study Report, 2021).

2.2. Field Data Collection

One month after the wildfires, a total of 30 Composite Burn Index CBI plots (30m × 30m) were established randomly within the wildfire affected areas. Wildfire severity was evaluated visually and classified at four levels of burn severity (unburned, low, moderate and high). Geographical coordinates were recorded at the center point of each plot using a GPS and digital photos were taken (See appendix 1). The four strata identified were substrate, herbs, shrubs and trees. They were stratified according to the forest type of the area combined with a preliminary interpretation of satellite image. Wildfire severity for each strata was visually evaluated as described in CBI data sheet (Key and Benson, 2006). The CBI contains information to evaluate burn severity level for five main strata of the vegetation: substrate, vegetation (herbs, shrubs, and trees) less than 1 m tall, tall shrubs and trees 1–5 m, intermediate trees (sub-canopy and pole-sized trees) and big trees (canopy, dominant and co-dominant) (Key and Benson, 2006). Burn-severity level within each stratum is estimated on a 0.0–3.0 scale. CBI overall severity value was then calculated by averaging the strata values of each plot. Field data of burned areas and severity were used to validate results (accuracy assessment) produced by Remote Sensing Landsat 8 spectral indices.

2.3. Satellite Data Collection and Analysis

To assess the forest areas affected by wildfires, a combination of satellite and field data were used. Cloud-free Landsat 8 satellite images acquired pre

and post fire (June – August 2017, respectively) were used in the analyses. Landsat 8 satellite imagery was downloaded free of charge on the US Space Agency (NASA) website (Url-1). Table 1 lists the band names, spatial resolutions and wavelengths of Landsat 8 OLI sensor.

Table 1. Spectral bands characteristics of Landsat 8 OLI

Bands	Wavelength (micrometers)	Resolution (meters)
Band 1 - Coastal aerosol	0.43-0.45	30
Band 2 - Blue	0.45-0.51	30
Band 3 - Green	0.53-0.59	30
Band 4 - Red	0.64-0.67	30
Band 5 - Near Infrared (NIR)	0.85-0.88	30
Band 6 - SWIR 1	1.57-1.65	30
Band 7 - SWIR 2	2.11-2.29	30
Band 8 - Panchromatic	0.50-0.68	15
Band 9 - Cirrus	1.36-1.38	30
Band 10 - Thermal Infrared (TIRS) 1	10.6-11.19	100
Band 11 - Thermal Infrared (TIRS) 2	11.50-12.51	100

The study area encompasses UTM zones 34, north. Images were downloaded in Level-2C product format and had some pre-processing related to geometric and radiometric correction based on field control points and the Digital Elevation Model (DEM) for topographic accuracy. The reflectance images were then imported into Miramon software for further analysis. The images were projected to the UTM/WGS84 projection. The pre-wildfire and post-wildfire images were selected as close as possible to the wildfire occurrence, in order to minimize spectral differences due to seasonal changes in the landscape. The eight wildfires considered in this study occurred during the time interval 14 July-18 August of year 2017. The pre-fire image (LC08_L1TP_186031_20170601) was selected on the 01th of June 2017 and the post-fire image (LC08_L1TP_186031_20170820) was selected on the 20th of August 2017. Landsat 8 satellite images were used to calculate spectral indices for burned area and severity assessment, as well as for vegetation regeneration. Spectral indices employed in this study were the Normalized Burn Ratio (NBR), NBR2, Normalized Difference Vegetation Index (NDVI) and Enhanced Vegetation Index (EVI) (Table 2). The pre-wildfire and post-wildfire NBR, NBR2 were used to calculate the differentiated NBR. The dNBR and dNBR2 index values were classified into several classes of burned severity (Table 3) following (Key and Benson, 2006).

Table 2. Spectral indices used in this study

Index full name	Abreviation	Formula	Reference
The Normalized Burn Ratio	NBR	$(NIR - SWIR2) / (NIR + SWIR2)$	Key and Benson, 2006
Differentiated NBR	dNBR	$NBR_{pre} - NBR_{post}$	Key and Benson, 2006
The Normalized Burn Ratio 2	NBR2	$(SWIR1 - SWIR2) / (SWIR1 + SWIR2)$	USGS, 2019
Normalized Difference Vegetation Index	NDVI	$(NIR - RED) / (NIR + RED)$	Tucker, 1979
Enhanced Vegetation Index	EVI	$2.5 * (NIR - RED) / (NIR + 6RED - 7.5BLU + 1)$	Huete et al., 2002

For Landsat 8: RED (Band 4); BLUE (Band2); NIR: Near infrared (Band 5); SWIR1: Short wave infrared (Band 6); SWIR2: Short wave infrared (Band 7)

Table 3. Classification of dNBR, dNBR2 values into burn severity classes (Key and Benson, 2006)

Burn severity class	Range of dNBR, dNBR2
Unburned	< 0.1
Low	0.1-0.349
Moderate	0.35-0.459
High	>0.46

To analyze and assess the current condition /regeneration of forest areas damaged by wildfire we used NDVI and EVI vegetation indices calculated on Landsat 8 images. In particular, near post (20th of August 2017) and one-year post fire (04th of June 2017) NDVI and EVI images were analyzed and difference images were used. The EVI index was used as a complement to the NDVI index because it was created to improve the vegetation signal and to provide more accurate data on photosynthetic activity on dense biomass areas (Huete et al., 2002).

2.4. GIS Analysis

The image maps of areas affected by wildfire and vegetation regeneration were imported to GIS where initially were converted to shapefile to

calculate the respective areas. Moreover, based on the field data and the dNBR values we identified 8 forest sites within the DMNP affected by the 2017 wildfire which were located near the villages of Tujan, Shëngjin i Vogël, Qafë Mollë, Derje, Shkallë, Selbe (2 areas) and Ibë (Figure 1). The perimeter of damaged areas was digitized and they were clipped on the dNBR and dNBR2 as well as the NDVI and EVI maps. Also, the preparation, comparison and export of maps produced was done through the use of Arc Map program.

3. RESULTS AND DISCUSSION

3.1. Burn area and severity

The fire-affected forest area evaluated in the field was 95 hectares (See appendix 2), whereas the one mapped by the Landsat spectral indices dNBR and dNBR2 were 103.59 and 105.72 ha, respectively (Table 4). Spectral indices clearly differentiated burned from unburned areas with a discrepancy of only 2% (Figure 2). Overall accuracies of forest burned area and severity maps generated with dNBR and dNBR2 were 91.7% and 89.8%, respectively.

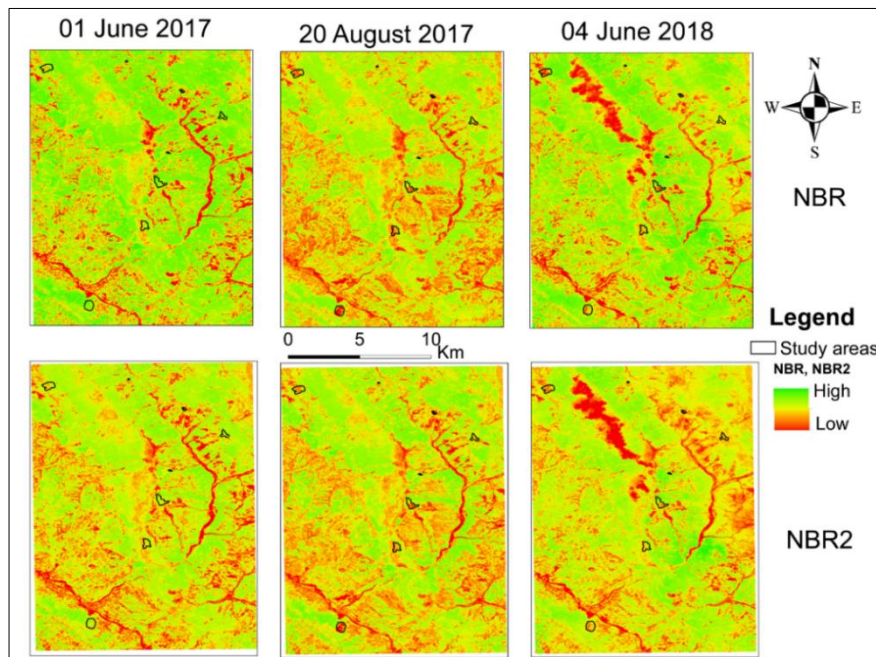


Figure 2. NBR and NBR2 images of the study area before the fire (01 June 2017), near after fire (20 August 2017) and after fire (04 June 2018). See Key and Benson, (2006) for NBR responses. Other details as in figure 1.

This indicates that dNBR spectral index was slightly more accurate at estimating fire severity compared to dNBR2. Various studies showed higher capability of NBR and NBR2 at discriminating burned areas as compared to other spectral indices (Sacramento et al., 2020; Sirin and Medvedeva, 2022; Atak and Tonyaloğlu, 2020). Based on these studies, both NBR and NBR2 indices produce similar results and are considered the most important indices to be used for burn area detection and mapping. However, the slight differences observed between NBR and NBR2 in this study could be related to NIR and SWIR spectral bands sensitivity to the characteristics of vegetation types in terms of density and spatial heterogeneity as they are captured from the remote sensing spectral reflectance (Mallinis et al., 2018). Figure 3 shows the forest areas affected by wildfire in 2017 at the NPDM, based on the dNBR/dNBR2 indices.

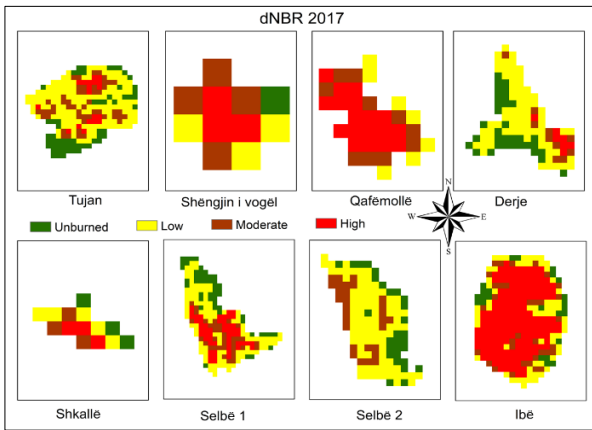


Figure 3. Maps of burned areas and burn severity detected by dNBR index

Forest site located at Ibë has suffered high wildfire damage as a significant part of the area was characterized by high dNBR values. More specifically, at Ibë about 60% of the forest area affected by wildfires was characterized by high burn severity while approximately 32% of the area was presented with moderate to low burn severity, and only 8% of the area was undamaged by wildfire (Figure 3, Table 4). Qafëmollë burned forest area also was characterized by high wildfire damage (51.42%), while in other forest areas (Shëngjin i Vogël (27.27%), Shkallë (21.43%), Selbe 2 (21.6%), Tujan (6.78%), Derje (5.83%)) only a relatively small part was characterized by high burn severity. Relatively high percentages of forest area moderately affected by wildfire were found at Shëngjin i Vogël (36.36%) and Qafëmollë (28.57%), while the areas with low burn severity were mainly found at Tujan (54.28%), Derje (58.33%), Selbe 1 (59.72%) and Selbe 2 (44.50%). Forest areas with the highest percentage of vegetation undamaged by wildfire were Tujan (21.07%), Derje (27.5%), Shkallë (21.43%) and Selbe 1 (20.14%). These tendencies are clearly observed in Figure 3 where

the burn severity levels are visible through the respective colors.

Figure 4 shows the forest areas affected by wildfire in 2017 according to the dNBR2 index. Also with dNBR2 index it was possible to map the burned areas as well as discriminate different burn severity levels. High burn severity was found at the forest sites of Ibe, Qafëmollë and Selbe 2, while the areas characterized by low burn severity or undamaged by wildfire were found mainly at sites of Tujan, Derje and Selbe 1.

The similarities of dNBR2 with dNBR index in terms of damaged area assessment were high but still noticeable changes were observed in all categories of burn severity at all sites (Table 4).

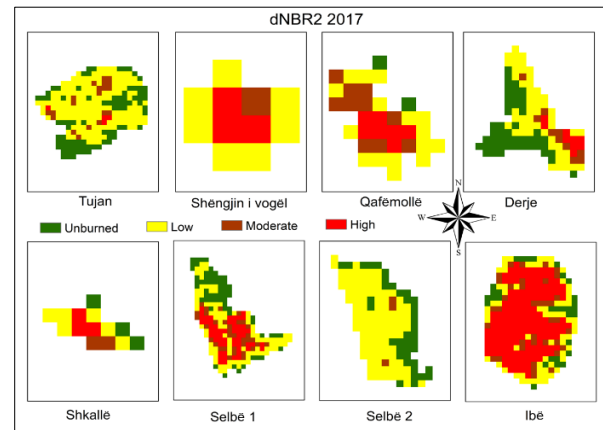


Figure 4. Maps of burned areas and burn severity detected by dNBR2 index.

Numerous researchers have studied the association between the dNBR index and wildfire severity all over the world to discriminate burned areas and assess vegetation regeneration after wildfire damage (Key and Benson, 2006; Nasery and Kalkan, 2020; Brown et al., 2018). They have found that the dNBR index achieves better discrimination of burned areas compared to other spectral indices due to the inclusion of near-infrared spectral band in its calculation. This spectral band is quite effective at discriminating areas affected by wildfire as chlorophyll strongly reflects sunlight at this wavelength and the scarce/lack of vegetation causes the reflection to be low/inexistent. When an area is burned, a drastic reduction in near-infrared reflection is observed, accompanied by an increase in the reflectance of the mid-infrared spectrum of most satellites (Lentile et al., 2006; Atak and Tonyaloğlu, 2020; Hu et al., 2021). Changes in spectral reflection of vegetation that occur after wildfire can be a good alternative for identifying patterns of areas affected by wildfire. The SWIR spectral bands used in the dNBR2 calculation are quite sensitive in terms of vegetation moisture content by identifying areas affected by wildfire due to their drastic drop in humidity level (Mallinis et al., 2018; Sacramento et al., 2020).

Table 4. Forest areas affected by wildfires in 2017 at the NPDM and the respective burn severity levels

Sites	Area (Ha)	Burn severity															
		Unburned				Low				Moderate				High			
		dNBR		dNBR ₂		dNBR		dNBR ₂		dNBR		dNBR ₂		dNBR		dNBR ₂	
Ha	%	Ha	%	Ha	%	Ha	%	Ha	%	Ha	%	Ha	%	Ha	%		
1	25.2	5.3	21.1	7.7	30.4	13.7	54.3	15.4	61.1	4.5	17.9	1.8	7.1	1.7	6.8	0.4	1.4
2	1.0	0.1	9.1	0.1	9.1	0.3	27.3	0.5	54.5	0.4	36.4	0.2	18.2	0.3	27.3	0.2	18.2
3	3.2	-	-	0.2	5.7	0.6	20.0	1.4	45.7	0.9	28.6	0.9	28.6	1.6	51.4	0.6	20.0
4	10.1	3.0	27.5	4.4	40.8	6.3	58.3	4.7	43.3	0.9	8.3	1.0	9.2	0.6	5.8	0.7	6.7
5	1.3	0.3	21.4	0.3	21.4	0.5	35.7	0.5	42.9	0.3	21.4	0.2	14.3	0.3	21.4	0.3	21.4
6	13.0	2.6	20.1	3.5	27.1	7.7	59.7	9.2	70.8	2.6	20.1	0.3	2.1	-	-	-	-
7	22.5	4.5	20.0	5.8	25.6	10.0	44.5	8.6	38.0	3.2	14.0	3.4	15.2	4.9	21.6	4.8	21.2
8	27.5	2.2	7.9	2.8	10.2	5.9	21.3	6.3	23.0	3.0	10.8	3.3	12.1	16.5	60.0	15.0	54.8
Total	103.6	17.9	17.3	24.8	23.8	45.0	43.4	46.6	45.0	15.8	15.1	11.1	10.7	25.9	24.9	22.0	21.2

Sites as in Figure 1.

3.2. Post-fire vegetation regeneration

Vegetation at the study area was generally characterized by high photosynthetic activity before the wildfire occurrence in 2017 but after the wildfire

there is a considerable decrease in the values of NDVI and EVI, respectively (Table 5). However, the dNDVI and dEVI images indicate the reactivation of photosynthetic activity /regeneration of vegetation in burned areas (Figure 5, Figure 6).

Table 5. Statistical parameters of NDVI and EVI within the burned areas

	NDVI				EVI			
	Pre	Post	Dif.	Next season	Pre	Post	Dif.	Next season
Min	0.46	0.26	-0.04	0.41	0.28	0.07	-0.01	0.21
Max	0.90	0.88	0.59	0.83	0.80	0.67	0.62	0.75
Mean	0.81	0.58	0.23	0.64	0.58	0.31	0.26	0.45
Std. dev.	0.07	0.15	0.14	0.09	0.09	0.13	0.12	0.10

As a matter of fact, the regeneration of vegetation appeared to be generally good in the subsequent years as the flora affected by fire mainly consists of shrub species which are characterized by high sprouting ability. The regeneration of vegetation was completely natural with no human interferences. The reduction of NDVI and EVI values immediately after the wildfire occurrence (Table 5) is related to the reduction of vegetation reflection in the near infrared spectral band due to the consumption of vegetation (chlorophyll) by wildfire, leaving the soil relatively bare.

In the case of Tujan forest area there exists moderate vegetation damage mainly at the central part where a more pronounced change is found in dNBR and dNBR₂ values (Figure 3, 4). In the succeeding year there are moderate level of vegetation regeneration at this site as revealed by the dNDVI and dEVI images (Figure 5, Figure 6). The area affected by wildfire at Shëngjin i Vogël, shows a higher degree of damage at the central part. However, the dNDVI and dEVI maps show a high level of vegetation restoration. In the forest area of Qafëmollë, regeneration of vegetation is evident in both dNDVI and dEVI indices and is observed mainly in the western and northwestern part of the affected area. In Derje forest area there is low impact of wildfire on vegetation and low changes regarding vegetation regeneration were observed in this area. Both vegetation indices showed the same pattern, although in the case of dNDVI the values obtained were higher. In the forest area of Shkallë vegetation

was considerably regenerated after wildfire, as high values of vegetation indices (mainly dNDVI) were observed. At Selbe forest area we found 2 sites affected by wildfires in 2017. At Selbe 1 in the succeeding year there was observed low regeneration of vegetation as the largest part of the affected area was characterized by low values of dNDVI and particularly dEVI. At Selbe 2 it was observed low impact of wildfire on vegetation and consequently low regeneration in the subsequent year. The regeneration pattern showed some variation between dNDVI and dEVI at this site. At Ibë forest area the impact of wildfire on vegetation was quite high. In the following year there were found high values of dNDVI and dEVI meaning high vegetation regrowth. Such values were observed mainly in the central and southern parts of the area while the other parts showed relatively low values of vegetation regeneration.

Our findings are in line with previously published research which found NDVI and EVI useful to evaluate vegetation activity (Huete et al., 2002, Pasho and Alla, 2015). However, NDVI showed higher performance and provided more realistic results of forest regeneration as confirmed by the field observations.

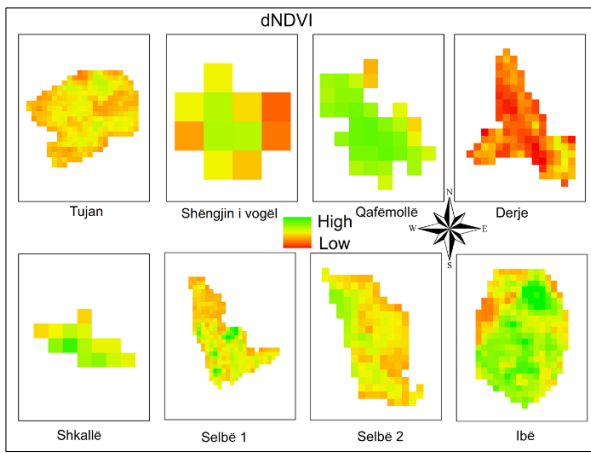


Figure 5. Spectral index maps showing the Normalized Difference Vegetation Index (dNDVI) of the burned areas in the subsequent growing season

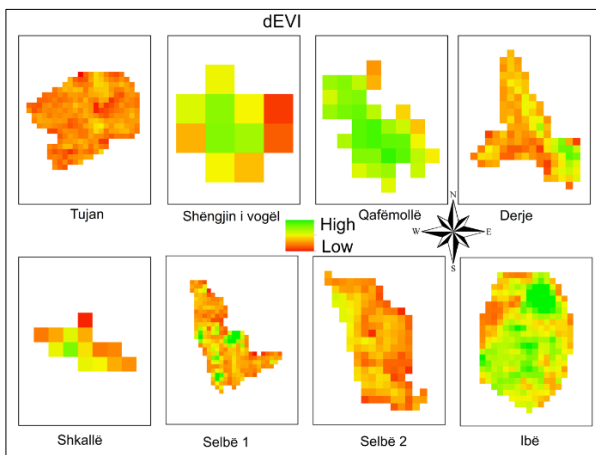


Figure 6. Spectral index maps showing the Enhanced Vegetation Index (dEVI) of the burned areas in the subsequent growing season

4. CONCLUSIONS

In this research, burn severity maps were produced to spatially detect the forest areas damaged by multiple wildfires in 2017. The dNBR and dNBR2 burn indices obtained from the Landsat 8 OLI satellite were closely related to field CBI estimates of burn severity, demonstrating their potential use in mapping wildfire severity effects experienced by Mediterranean forest ecosystems. The study concluded that Landsat 8 spectral indices were efficient at discriminating burned from unburned areas as well as different levels of burned severity. The dNBR and dNDVI were the best indices to discriminate/delineate burned areas/burn severity and to evaluate vegetation regeneration in the subsequent season. While the combination of several alternative indices did not provide significant improvements in this study, they could prove useful in other areas but this is subject to further investigations. The burn severity varied from one area to another but it was particularly high at the forest areas of Ibë and Qafëmollë. The regeneration

of vegetation in the succeeding year was poor at the forest areas of Derje and Tujan which were found to be low to moderately affected by wildfire while the areas highly affected by wildfires (Ibë and Qafëmollë) resulted to be in good state of vegetation regeneration in the following year. We recommend that in future studies, Remote Sensing and GIS technology be used widely for mapping and assessment of burned areas as an effective tool for forest managers/specialists in designing efficient management plans for the rehabilitation of these areas. In areas where the vegetation regeneration is low or absent, it is recommended to apply silvicultural measures (reforestation, afforestation, etc.) for their rehabilitation.

Author Contributions

Edmond Pasho: Conceptualization, Methodology, Software, Writing- Original draft preparation. **Arben-Q. Alla:** Data curation, Supervision, Writing- Reviewing and Editing. **Ernest Ramaj:** Data curation, Visualization.

Conflicts of Interest

The authors declare no conflict of interest.

REFERENCES

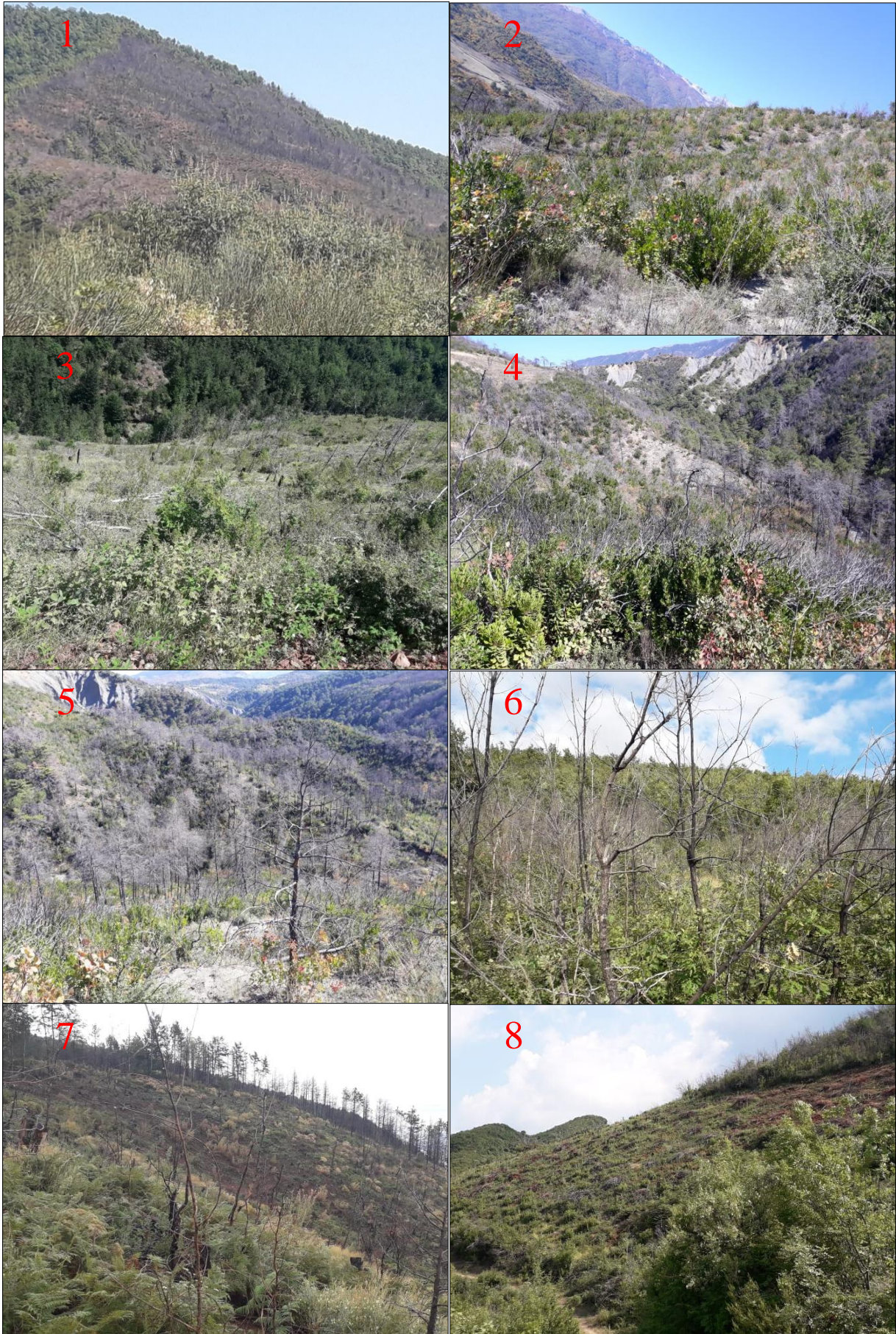
- Atak, B.K., & Tonyaloğlu, E.E. (2020). Evaluating spectral indices for estimating burned areas in the case of Izmir/Turkey. *Eurasian Journal of Forest Science*, 8(1), 49-59.
- Brown, A.R., Petropoulos, G.P., & Ferentinos, K.P. (2018). Appraisal of the Sentinel-1 & 2 use in a large-scale wildfire assessment: A case study from Portugal's fires of 2017. *Applied geography*, 100, 78-89.
- Bruci, E. (2007). Climate change projection for South Eastern Europe. Tirana: HMI, Tirana Polytechnic University.
- Escuin, S., Navarro, R., & Fernández, P. (2008). Fire severity assessment by using NBR (Normalized Burn Ratio) and NDVI (Normalized Difference Vegetation Index) derived from LANDSAT TM/ETM images. *International Journal of Remote Sensing*, 29(4), 1053-1073.
- Firewise, (1998). Wildfire News and Notes. *Wildland Fire Management Terminology*. 12(1), 10.
- Forestry Sector Study Report, (2021). Sustainable Development of rural areas in Albania – Sector Analyses – 2017.2192.7- 001.00.
- Hu, X., Ban, Y., & Nascetti, A. (2021). Uni-temporal multispectral imagery for burned area mapping

- with deep learning. *Remote Sensing*, 13(8), 1509.
- Hudak, A.T., Morgan, P., Bobbitt, M.J., Smith, A., Lewis, S. A., Lentile, L.B., Robichaud, P.R., Clark, J.T., & McKinley, R.A. (2007). The relationship of multispectral satellite imagery to immediate fire effects. *Fire Ecology*, 3(1), 64-90.
- Huete, A., Didan, K., Miura, T., Rodriguez, E. P., Gao, X., & Ferreira, L.G. (2002). Overview of the radiometric and biophysical performance of the MODIS vegetation indices. *Remote sensing of environment*, 83(1-2), 195-213.
- Key, C.H., & Benson, N.C. (2006). Landscape assessment: Sampling and analysis methods. In: FIREMON: Fire Effects Monitoring and Inventory System; Lutes, D.C., Keane, R.E., Caratti, J.F., Key, C.H., Benson, N.C., Sutherland, S., Gangi, L.J., Eds.; Gen. Tech. Rep. RMRS-GTR-164; LA1-LA55 ISBN USDA Forest Service Gen. Tech. Rep. RMRS-GTR-164-CD; U.S. Department of Agriculture, Forest Service, Rocky Mountain Research Station: Fort Collins, CO, USA, 2006.
- Lentile, L.B., Holden, Z.A., Smith, A.M., Falkowski, M. J., Hudak, A.T., Morgan, P., ... & Benson, N. C. (2006). Remote sensing techniques to assess active fire characteristics and post-fire effects. *International Journal of Wildland Fire*, 15(3), 319-345.
- Mallinis, G., Mitsopoulos, I., & Chrysafi, I. (2018). Evaluating and comparing Sentinel 2A and Landsat-8 Operational Land Imager (OLI) spectral indices for estimating fire severity in a Mediterranean pine ecosystem of Greece. *GIScience & Remote Sensing*, 55(1), 1-18.
- Morgan, P., Keane, R., Dillon, G., Jain, T., Hudak, A., Karau, E., Sikkink, P., Holden, Z., & Strand, E. (2014). Challenges of assessing fire and burn severity using field measures. *Remote Sensing and Modelling. International Journal of Wildland Fire*, 23(8), 1045-1060.
- Nasery, S., & Kalkan, K. (2020). Burn area detection and burn severity assessment using Sentinel 2 MSI data: The case of Karabağlar district, İzmir/Turkey. *Turkish Journal of Geosciences*, 1(2), 72-77.
- Pasho, E., & Alla, A.Q. (2015). Climate impacts on radial growth and vegetation activity of two co-existing Mediterranean pine species. *Canadian Journal of Forest Research*, 45, 1748-1756.
- Sacramento, I.F., Machado Michel, R.F., & Siqueira, R.G. (2020). Bitemporal analysis of burned areas in the Atlantic Forest. *Sociedade & Natureza*, 32, 540-552.
- San-Miguel-Ayanz, J., Durrant, T., Boca, R., Libertà, G., Branco, A., de Rigo, D., Ferrari, D., Maianti, P., Vivancos, T. A., ... & Costa, H. (2018). Forest fires in Europe, Middle East and North Africa 2017; EUR 29318 EN; JRC European Union: Luxembourg, 2018.
- Saulino, L., Rita, A., Migliozi, A., Maffei, C., Allevato, E., Garonna, A.P., & Saracino, A. (2020). Detecting burn severity across mediterranean forest types by coupling medium-spatial resolution satellite imagery and field data. *Remote Sensing*, 12(4), 741.
- Sirin, A., & Medvedeva, M. (2022). Remote Sensing Mapping of Peat-Fire-Burnt Areas: Identification among Other Wildfires. *Remote Sensing*, 14(1), 194.
- Tucker, C. J., Pinzon, J.E., Brown, M.E., Slayback, D. A., Pak, E.W., Mahoney, R. Vermote, E.F., & El Saleous, N. (2005). An extended AVHRR 8-km NDVI dataset compatible with MODIS and SPOT vegetation NDVI data. *International journal of remote sensing*, 26(20), 4485-4498.
- USGS. (2019). Landsat Surface Reflectance-Derived Spectral Indices. Retrieved 10 June 2022 from <https://www.usgs.gov/land-resources/nli/landsat/landsat-normalized-burn-ratio>.
- Url-1: <https://earthexplorer.usgs.gov/> (last accessed 21 June 2022)
- Warner, T.A., Skowronski, N.S., & Gallagher, R.M. (2017). High spatial resolution burn severity mapping of the New Jersey Pine Barrens with WorldView-3 near-infrared and shortwave infrared imagery. *International Journal of Remote Sensing*, 38(2), 598-616

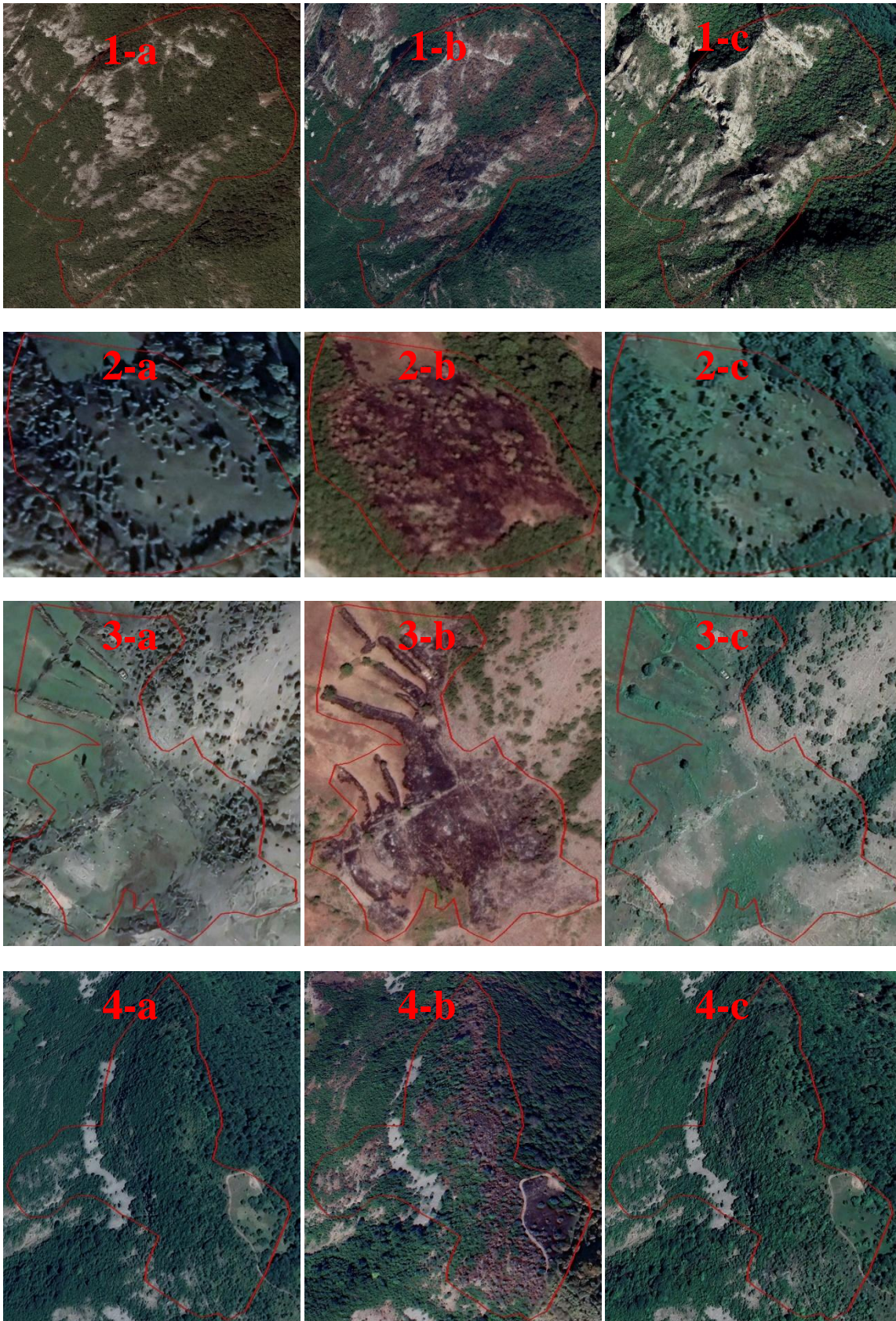


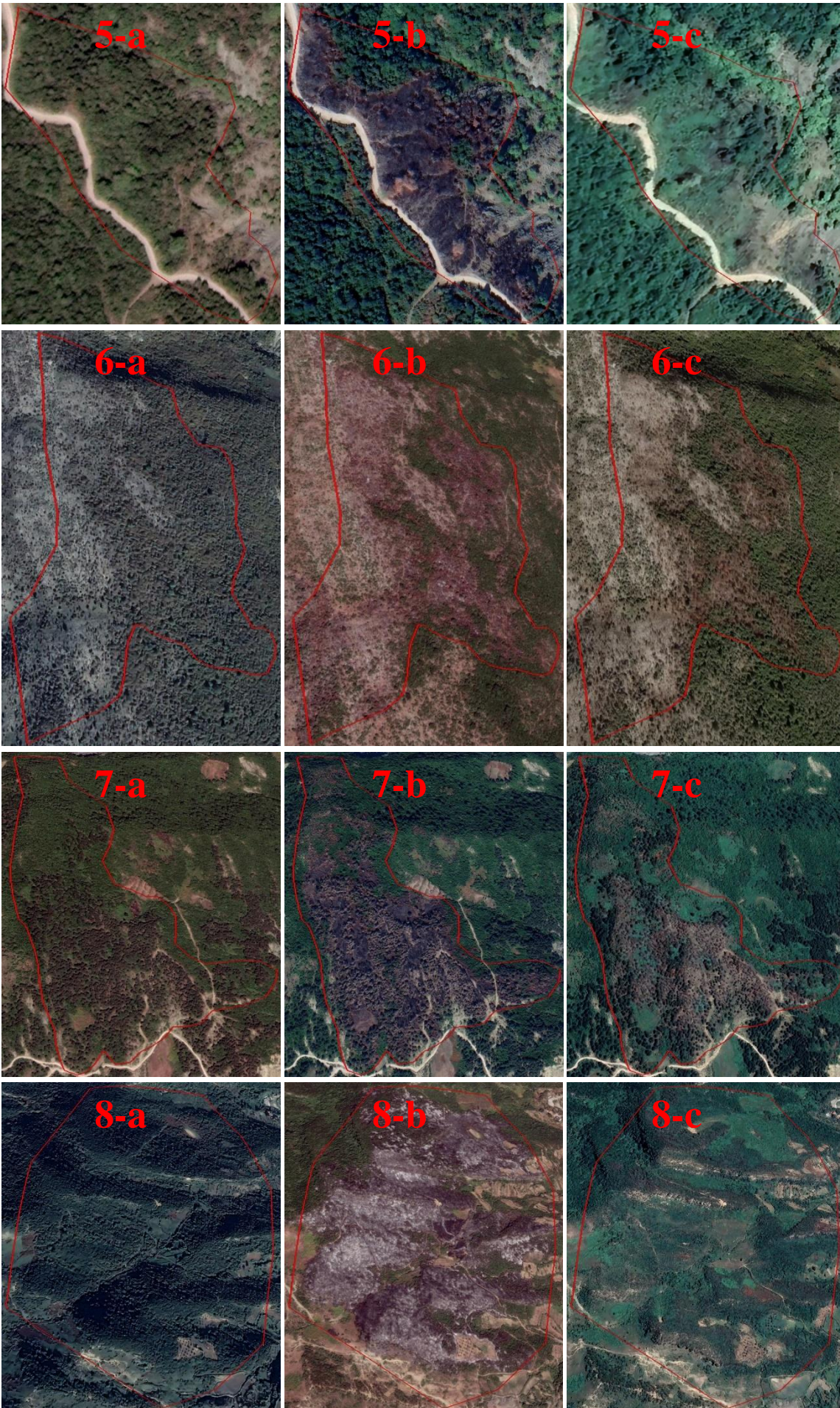
© Author(s) 2021. This work is distributed under <https://creativecommons.org/licenses/by-sa/4.0/>

Appendix 1. Field photographs of post-fire conditions in the study area. Numbers as in Figure 1.



Appendix 2. Google earth images showing the study areas before the fire (a), near after the fire (b) and after the fire (c). Numbers as in Figure 1.





Investigation of the Hamamayađı/Ladik (Samsun, Turkey) geothermal field and it's surroundings by optical Remote Sensing with GIS methods

Ömer Faruk Uzun*¹, Orkun Turgay²

¹ Sinop University, Boyabat Vocational School, Department of Architecture and Urban Planning, Sinop, Turkey

² Jeomodel Resources, Ankara, Turkey

Keywords

Geothermal
Potential
Mapping
ASTER
Remote Sensing
GIS

ABSTRACT

In this study, the geothermal potential was investigated by remote sensing methods in the Ladik Hamamayađı region of Samsun province at the Central Black Sea region. The satellite images were evaluated in the GIS environment. Various parameters differ in remote sensing studies and post-exploration geothermal field remote sensing for exploration studies, and these parameters are explained in detail in the study. All alteration types that should be in a geothermal field were mapped with the ASTER data, lineaments were extracted, thermal anomalies were captured and interpreted with alterations in the GIS environment, since there are no alteration information in the Hamamayađı geothermal field that previous studies have uncovered. As a result of these processes and interpretations, remote sensing and GIS methods were used together for the Hamamayađı geothermal field to produce guiding data and maps for the discovery of new potential areas. Within the framework of these produced maps, technical suggestions were made to the authorities who have a say on the subject.

1. INTRODUCTION

Depending on the development and growth rate of countries, their energy needs are constantly increasing (Arslan et al., 2001). For this reason, those who undertake the administration of the country have to find energy in uninterrupted, reliable, clean and cheap ways and to diversify these sources (Akkoyunlu, 2006; Pamir, 2003). In this context, countries are trying to create their energy policies for the development and use of renewable energy resources, both to meet this demand and to take into account the cost of exhaustible fossil resources and their environmental effects. Geothermal energy, one of the renewable energy sources that ensure the sustainability of nature in its own cycle, has started to have an important share in meeting the energy needs of countries in recent years. (Akkuş, 2017). As it is known, Geothermal Energy is a domestic underground resource that is renewable, clean, cheap and environmentally friendly. Ozdemir, (2012) studied known geothermal fields in Turkey. Ozdemir et al. (2017) studied Kavaklıdere

Geothermal Field with structural geological principles. Ozdemir and Palabiyik, (2019) developed a new evaluation method of magnetotelluric (MT) data for geothermal fields. Ozdemir et al. (2021a) studied Gediz Graben with structural geology and revealed the geological model of geothermal system. Since our country is located on an active tectonic belt. Ozdemir et al. (2021b) reevaluated the Çubukludağ geothermal field potential and produced 3D structural model of the geothermal system.

Due to its geological and geographical location, it is in a rich position among the world countries in terms of geothermal. There are many geothermal resources at different temperatures in the form of around 1000 natural outflows spread all over our country. Again, the geothermal potential of our country is quite high, and 78% of the potential-forming areas are located in Western Anatolia, 9% in Central Anatolia, 7% in the Marmara Region, 5% in Eastern Anatolia and 1% in other regions. 90% of our geothermal resources are low and medium temperature, and direct applications (heating, thermal tourism, various industrial applications,

* Corresponding Author

(ofuzun@sinop.edu.tr) ORCID ID 0000-0002-0391-4495
(orkun.turgay@yahoo.com) ORCID ID 0000-0001-6958-3628

Cite this article

Received: 19/06/2022; Accepted: 07/11/2022

Uzun Ö.F., & Turgay O. (2022). Investigation of the Hamamayađı/Ladik (Samsun, Turkey) geothermal field and it's surroundings by optical Remote Sensing with GIS methods. Turkish Journal of Geosciences 3(2), 75-83.

etc.), and 10% of them are suitable for indirect applications (electric power generation) (MTA, 2021a). In this context, the distribution and

application map of the geothermal resources of our country is shown in Figure 1.

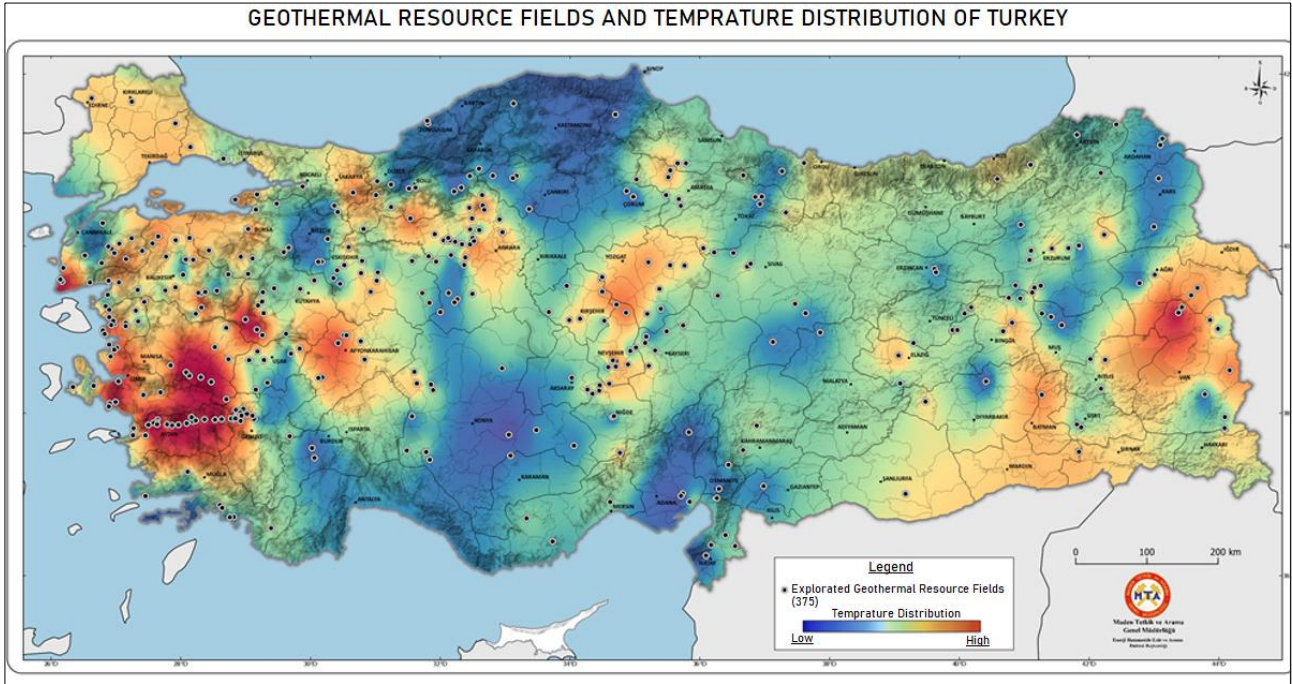


Figure 1. Geothermal map of Turkey (MTA, 2021b)

Within the framework of the mentioned issues, it is extremely important to find new potential geothermal resources in our country and to include them in energy production. Because although Turkey is lucky in terms of its geothermal resources, it is one of the countries with hundreds of geothermal resources that can use these resources at a minimum rate and are waiting to be uncovered (Akin et al., 2014). Remote Sensing technology has started to take its place in the scientific literature as one of the most effective methods involved in the preliminary research of these resource studies. In recent years, there have been important studies conducted in Turkey with Geographical Information Systems and Remote Sensing methods in geothermal exploration (Yalçın and Gül, 2017; Yıldız et al., 2017; Balçık and Ergene, 2017; Yurteri and Şimşek, 2017; Melikoğlu, 2017). Surface temperature distribution mapping using surface temperature analysis (STA) calculated using satellite images performed in these studies is widely used to determine geothermal fields. For studies such as geothermal research, land surface temperature is an important parameter. (Oğuz, 2015). In addition, in the use of remote sensing and GIS for geothermal exploration, suitable areas for exploration were determined by combining volcanic units, faults, hot water outlets, alterations, fumaroles, heat flux and temperature gradient with various GIS methods for exploration with spatial analysis in the study of Moghaddam et al. (2014). Apart from this, in the study of Noorollahi et al. (2015), in addition to the study of Moghaddam et al. (2014), geoelectric data were combined with

geological and geochemical data in the GIS environment and suitable locations for exploration were determined. In the study of Noorollahi et al. (2008), the distance to the faults, the distance to the calderas, the distance to the alteration zones, the distance to the hot water outlets and the distances to the volcanic domes were evaluated in the GIS environment, and results were obtained for the well location selection and geothermal exploration. The Ladik-Hamamayağı Geothermal Area, which has been studied within the framework of these aforementioned issues, is located in the Northwest of Ladik, 12 km away. The region is 73 km from Samsun Province. Within the scope of the study, potential geothermal resources were investigated by remote sensing methods in and around Samsun Ladik Hamamayagi Geothermal Zone. Aim of this article is using remote sensing derived parameters which are weighted in GIS environment can be used for remote detection of geothermal anomalous zones in study area.

1.1. Study Area

The Ladik-Hamamayağı Geothermal Area (Figure 2) which has been studied within the framework of these aforementioned issues, is located in the Northwest of Ladik, 12 km away. The region is 73 km from Samsun province away. Within the scope of the study, potential geothermal resources were investigated by remote sensing methods in and around Samsun Ladik Hamamayagi Geothermal Zone. The study area that is the subject

of the study is given in Figure 2. Gültekin et al. (2010) studied the hydrochemistry of geothermal waters of Hamamayağı-Ladik area.

Gray, gray colored, hard, heavily cracked Permian aged recrystallized limestone's can be found at the bottom of the Ladik Hamamaya geothermal area (Figure 3). The unit is overlain by beige, cream-colored chert nodules and cracked Jurassic-Cretaceous aged limestone's. It is covered by an Eocene-aged unit made up of sandstone and claystone. The sequence then moves on to Neogene-aged units with conglomerate, claystone, and sandstone lithology. The youngest rock units are Quaternary-aged alluvium cone with old and new alluviums (MTA, 2005).

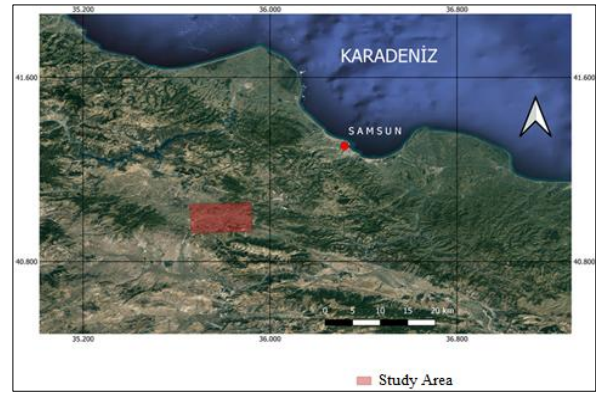


Figure 2. Study area

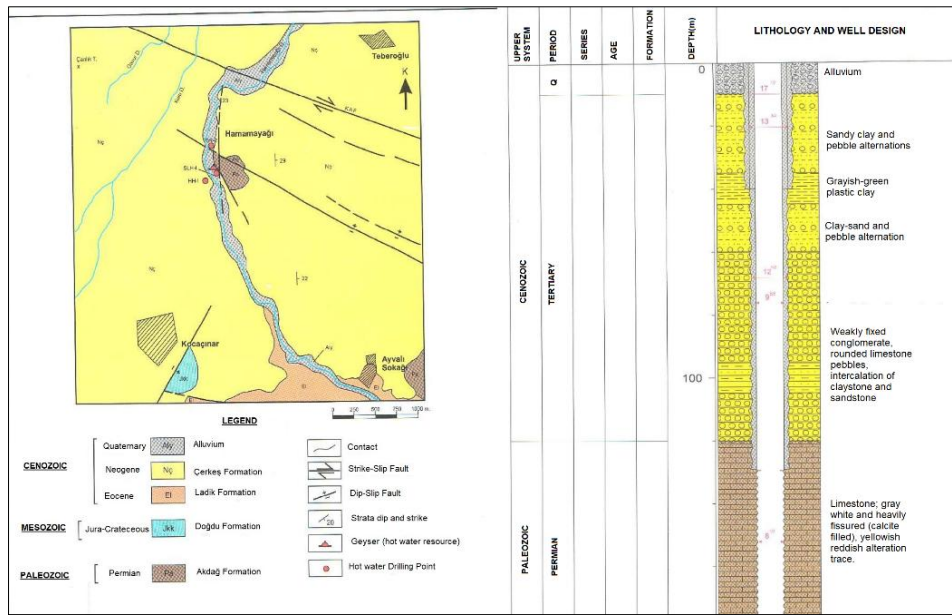


Figure 3. Geology of Hamamayağı-Ladik Geothermal area (MTA, 2005) and Bekdiğın BK-2 Well design with drilling log

2. METHOD

For remote sensing, ASTER (Advanced Space borne Thermal Emission and Reflection Radiometer) L1T dataset was used for gaining alteration parameters which used in GIS environment.

The ID of ASTER L1T dataset is AST_L1T_00303202004083222_20150503172907_68414. Alteration parameters gained from ASTER dataset by ENVI 5.3 software later parameters processed in ArcGIS PRO software. In ArcGIS, map visualizations and gridding made also in ArcGIS weighted overlay analysis was applied. For lineament extraction, LINE module of PCI Geomatica was used with Öztürk and Uygucgil, (2018)'s method later, extracted lineaments transformed to the lineation density with the line density module of ArcGIS software. Every raster data weighted to the five level from minimum to maximum level with ArcGIS Pro overlaid with Weighted Overlay tool to extract geothermal potential zones as map.

2.1. Preprocessing of ASTER Data

In preprocessing step, radiometric calibration and atmospheric correction of dataset was completed in ENVI 5.3 software, SWIR, VNIR and TIR bands of ASTER radiometrically calibrated then VNIR and SWIR data stacked in one file after this processing step radiometrically calibrated TIR bands atmospherically corrected by thermal atmospheric correction and Emissivity Normalization applied the corrected TIR dataset. While TIR dataset converting the Emissivity, surface temperature data in Kelvin obtained later it was transformed to the Celsius with (b1-273.15) formula.

2.2. Geological Image Processing of Aster Data

Hydrothermal alterations were extracted from ASTER SWIR and VNIR dataset and with Emissivity Normalization Thermal anomaly map extracted. Also Quartz and silification images obtained from corrected TIR dataset. Images of alterations obtained

from ASTER dataset are Potassic alteration, sericitization, propylitic alteration, argillic alteration, advanced argillic alteration which are important for hydrothermal alterations. Also these images were evaluated in GIS environment with Weighted Overlay algorithm. Lineament density maps were also evaluated in GIS environment. Weighted overlay analysis is using for decision making in GIS. In ArcGIS, analytical hierarchy model is most common in weighted overlay analysis.

3. RESULTS

The use of remote sensing in studies on the existence of geothermal potential was given in the introduction with previous studies. This study can be given as an example of geothermal potential maps that can be obtained with different data processing methods. The methodology of the study is to extract hydrothermal alterations such as alunitization (Figure 3), argillic alteration (Figure 4), fengite

(Figure 5), Kaolenitization (Figure 6), propylitization (Figure 7), Quartz distribution (Figure 8), sericitization (Figure 9), that may indicate geothermal exactly and after being subjected to weighted overlay analysis as a set, they are subjected to weighted overlay analysis together with surface temperature (Figure 11) and lineament density (Figure 10) maps. In this geothermal potential study carried out in the Hamamayağı region, the existence of a geothermal potential in Yenice, Bekgin and Hamamayağı regions was determined by remote sensing methods. In addition, it has been determined that the most visible alteration type in the Hamamayağı geothermal area is propylitization. Based on all this analysis, it has been determined that the study area has a paleotemperature history of up to 400 degrees and a geothermal potential. According to the maps obtained from the study, it is thought that positive results can be achieved if geothermal exploration studies are carried out in the red areas on the maps.

Table 1. Hydrothermal alteration formulas for ASTER L1T dataset

INDEX/INDICE	ALTERATION	REFERENCE
$(B4+B6)/B5$	Advanced Argillic Alt.	Fakhari et al., (2019)
$(B6+B9)/(B7+B8)$	Propylitization	Shahi and Kamkar-Rouhani, (2014)
$(B7/B5)*(B7/B8)$	Alunitization "ALI"	Ninomiya, (2002)
$(B4/B5)*(B8/B6)$	Kaolenitization "KLI"	Ninomiya, (2003)
$(B5+B7)/B6$	Argillic Alteration	Testa et al., (2018)
$B5/B6$	Fengitic Mica "Fengite"	Bakardjiev and Popov, (2015)
$(B11*B11)/(B10*B12)$	Quartz Indice "QI"	Ninomiya, (2003)
$(B5+B7)/B6$	Sericitization	Fatima et al., (2017)

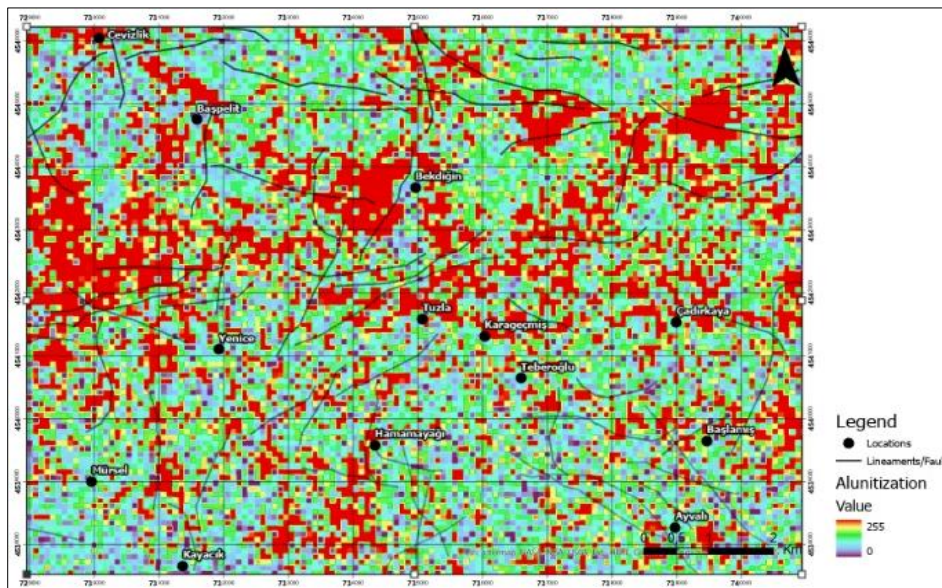


Figure 4. Alunitization distribution in study area

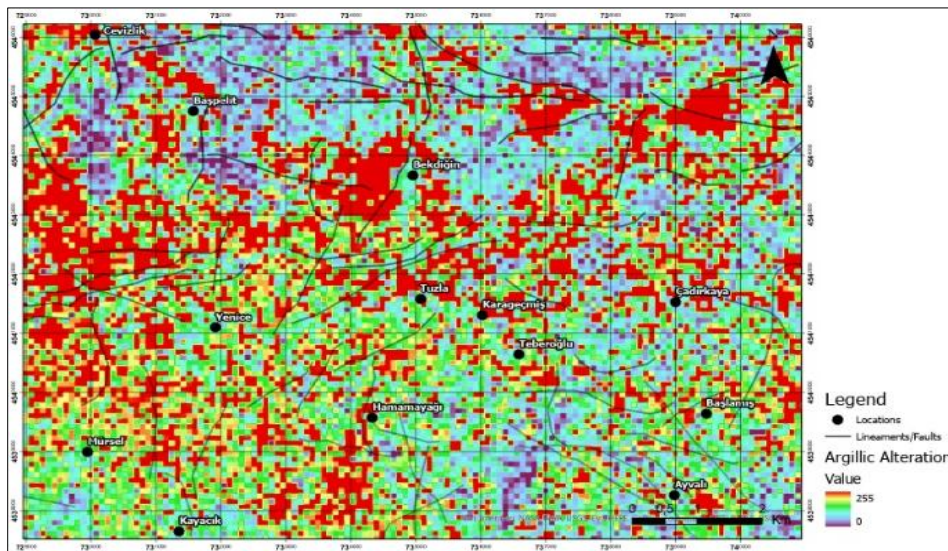


Figure 5. Argillic alteration in study area

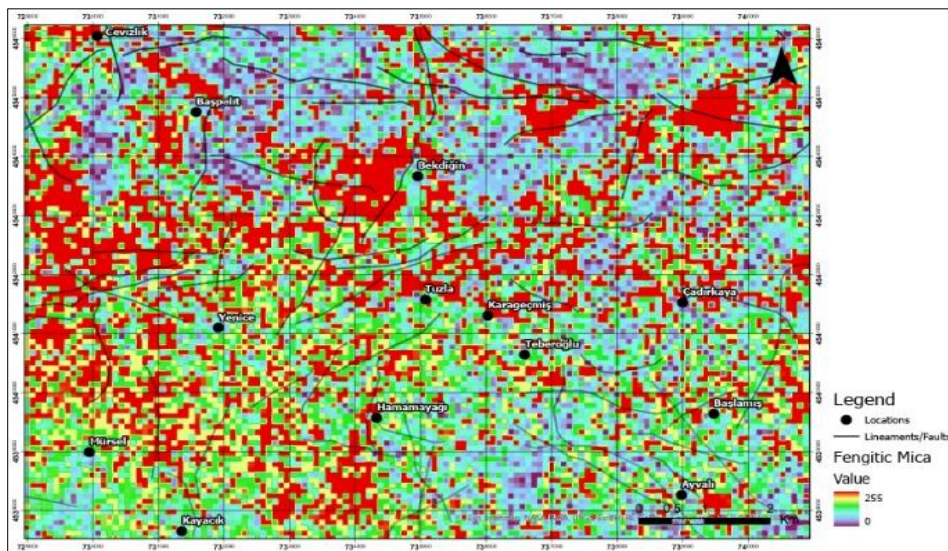


Figure 6. Fengitic mica in study area

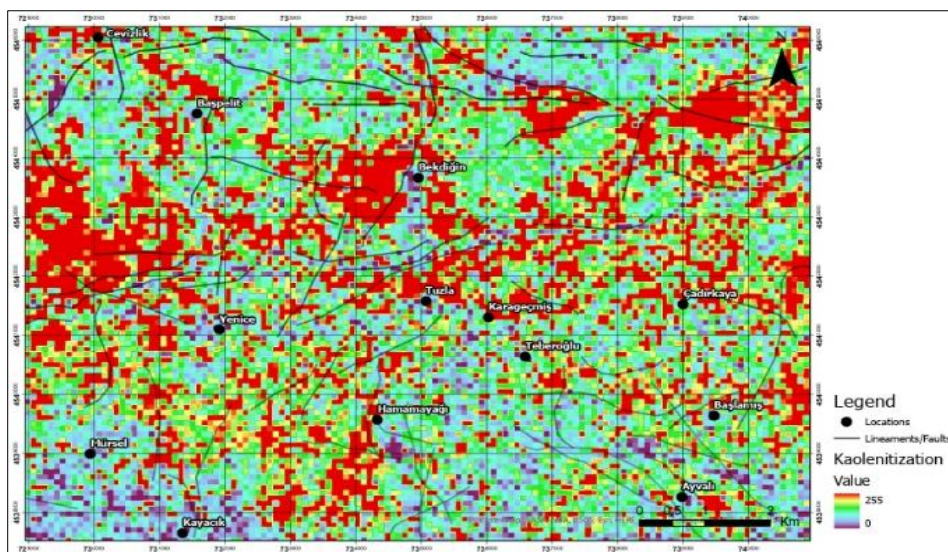


Figure 7. Kaolinitization in study area

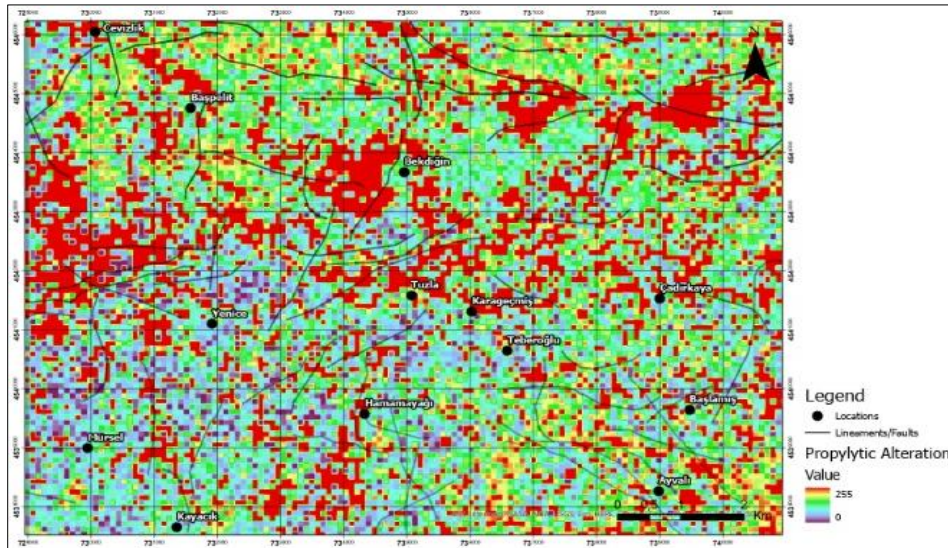


Figure 8. Propylitic alteration in study area

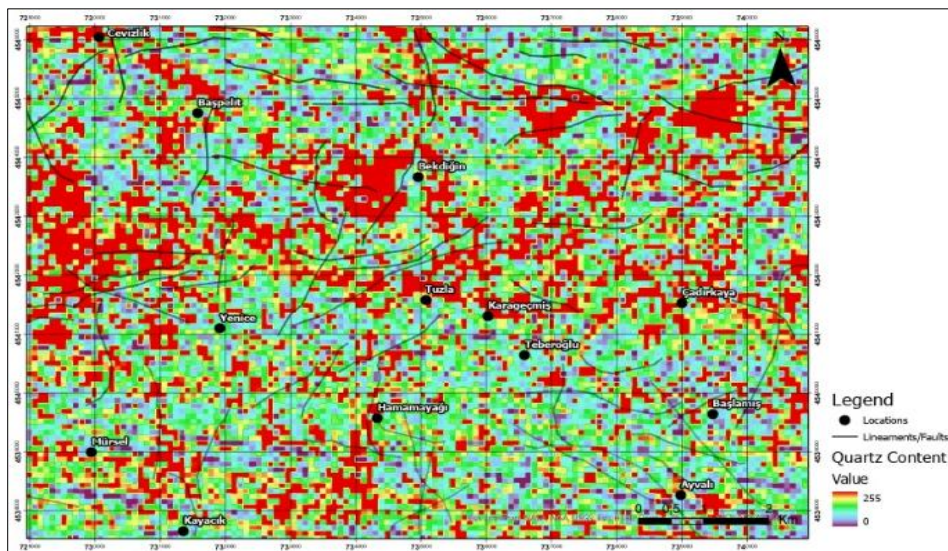


Figure 9. Quartz distribution in study area

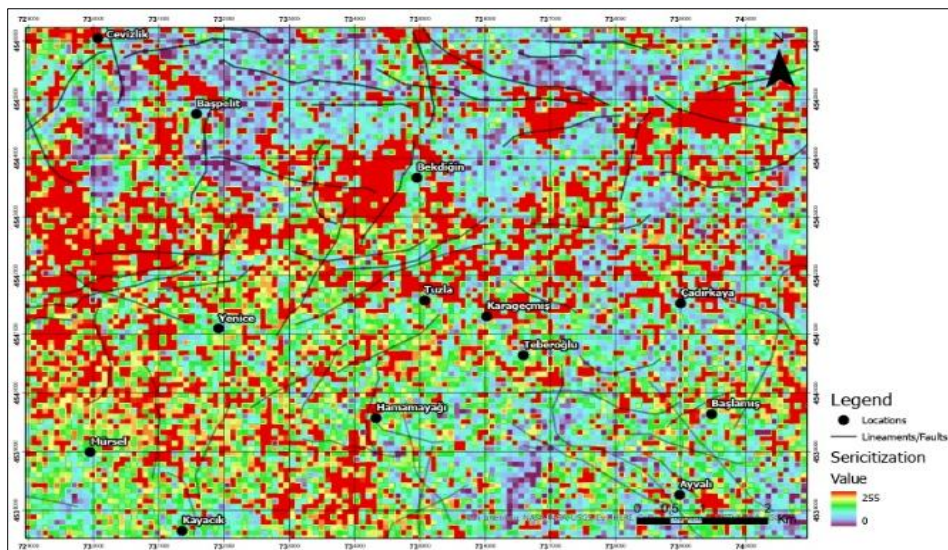


Figure 10. Sericitic alteration in study area

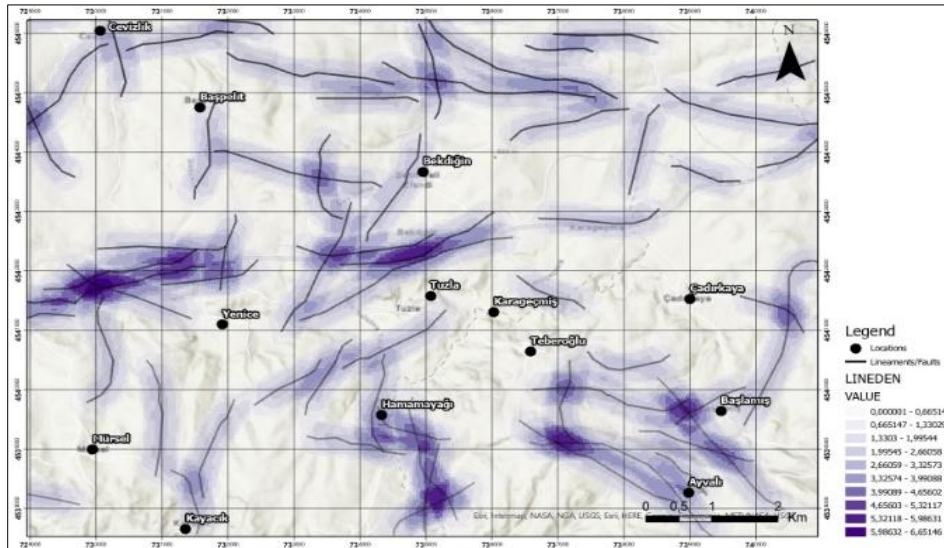


Figure 11. Fault (lineation) density in study area

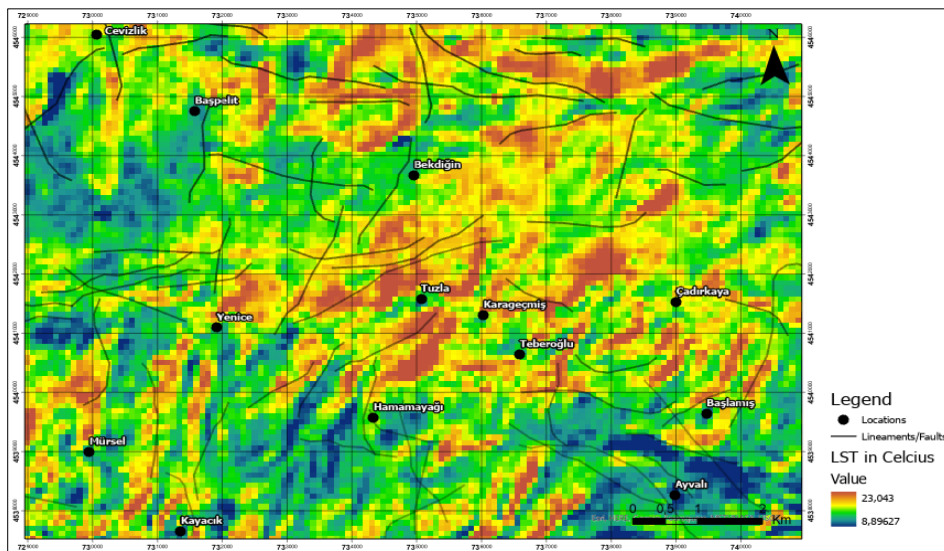


Figure 12. Land surface temperature (LST) in study area

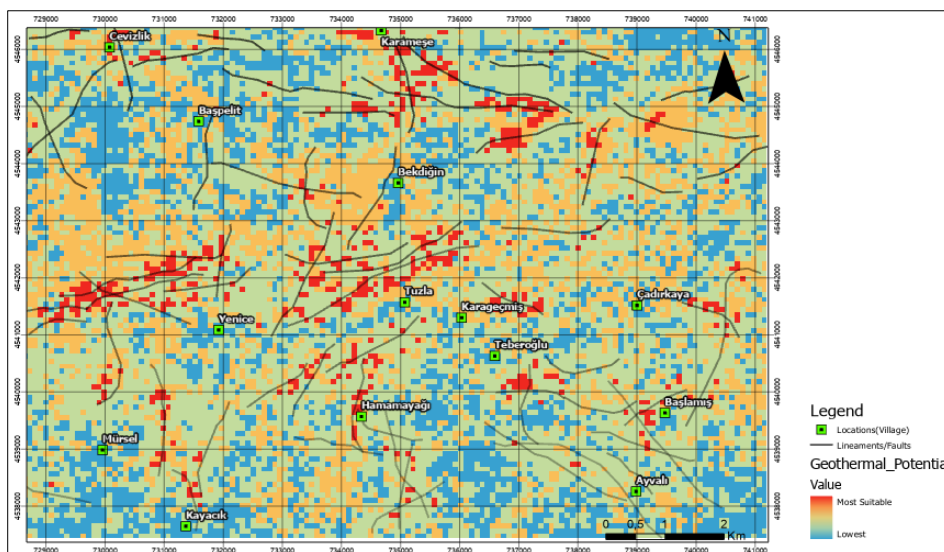


Figure 13. Resultant image of the study, geothermal potential map of study area

4. CONCLUSIONS

Among the alterations that can be form in the geothermal field, ASTER data has been processed for Advanced argillic alteration, Alunitization, Argillic alteration, Phengitic mica, Kaolinization, Propylitization/Propylitic alteration, silicification and sericitization (Table 1). The data obtained from the ASTER data, the lineament data and the temperature data were combined in the GIS environment. The results obtained as a result of the conducted studies are given in Figure 3 to 12.

It has emerged that the propylitic alteration in the Hamamayağı geothermal field should be defined as a pathfinder alteration. Because the geothermal field and the propylitic alteration image exactly coincide. The presence of thermal hotels in Hamamayağı province draws attention in places where there is propylitic alteration. The temperature of formation of propylitic alteration (epidote-chlorite) is between 250-400 degrees. This means that the paleo-temperature reaches 400 degrees.

Author Contributions

Ömer Faruk Uzun: Conceptualization, Methodology, Software. **Orkun Turgay:** Data curation, Writing- Original draft preparation and Data processing

Conflicts of Interest

The authors declare no conflict of interest.

REFERENCES

Akın, U., Uluggerli, E.U., & Kutlu, S. (2014). Türkiye jeotermal potansiyelinin ısı akısı hesaplamasıyla değerlendirilmesi. *MTA Dergisi*, 149, 205-214.

Akkoyunlu, A. (2006). Türkiye'de enerji kaynakları ve çevreye etkileri, *Türkiye'de Enerji ve Kalkınma Sempozyumu Bildiri Kitabı*, Bahçeşehir Üniversitesi, İstanbul, 131-145.

Akkuş, İ. (2017). Neden jeotermal enerji? Türkiye için önemi, hedefler ve beklentiler. *Mavi Gezegen Dergisi*, 23, 25-39.

Arslan, S., Darıcı, M., & Karahan, Ç. (2001). Türkiye'nin jeotermal enerji potansiyeli. *Jeotermal Enerji Semineri*, 21-27.

Bakardjiev, D., & Popov, K. (2015). ASTER spectral band ratios for detection of hydrothermal alterations and ore deposits in the Panagyurishte Ore Region, Central Srednogie, Bulgaria. *Review of the Bulgarian Geological Society*, 76(1), 79-88.

Balçık, F.B., & Ergene, E.M. (2017). Yer yüzey sıcaklığının termal uzaktan algılama verileri ile belirlenmesi: İstanbul örneği. *Türkiye Ulusal Fotogrametri ve Uzaktan Algılama Birliği 9. Teknik Sempozyumu Bildiri Özetleri Kitabı içinde (Turgut B. vd., Ed)*, Afyonkarahisar, Türkiye, 21.

Gültekin, F., Hatipoğlu, E., & Fırat Ersoy, A.F. (2010). Ladik-Hamamayağı (Samsun) sıcak ve soğuk su kaynaklarının hidrojeokimyası ve köken yorumu. *Yerbilimleri*, 31(2), 111-126.

Fakhari, S., Jafarirad, A., Afzal, P., & Lotfi, M. (2019). Delineation of hydrothermal alteration zones for porphyry systems utilizing ASTER data in Jebel-Barez area, SE Iran. *Iranian Journal of Earth Sciences*, 11(1), 80-92.

Fatima, K., Khattak, M.U.K., Kausar, A.B., Toqeer, M., Haider, N., & Rehman, A.U. (2017). Minerals identification and mapping using ASTER satellite image. *Journal of Applied Remote Sensing*, 11(4), 046006.

Melikoğlu, M. (2017). Geothermal energy in Turkey and around the World: A review of the literature and an analysis based on Turkey's Vision 2023 energy targets. *Renewable and Sustainable Energy Reviews* 76, 485-492

Moghaddam, M.K., Samadzadegan, F., Noorollahi, Y., Sharifi, M.A., & Itoi, R. (2014). Spatial analysis and multi-criteria decision making for regional-scale geothermal favorability map. *Geothermics*, 50, 189-201.

MTA, (2021a). Türkiye jeotermal enerji potansiyeli ve arama çalışmaları. from <https://www.mta.gov.tr/v3.0/arastirmalar/jeotermal-enerji-arastirmalari>.

MTA, (2021b). Türkiye jeotermal kaynaklarının dağılımı ve uygulama haritası. From <https://www.mta.gov.tr/v3.0/sayfalar/hizmetler/jeotermal-harita/images/1.jpg>

MTA, (2005). Inventory of Geothermal Resources of Turkey, Ankara.

Ninomiya, Y. (2003). A stabilized vegetation index and several mineralogic indices defined for ASTER VNIR and SWIR data. In *IGARSS 2003. 2003 IEEE International Geoscience and Remote Sensing Symposium. Proceedings* (Vol. 3, pp. 1552-1554). IEEE.

Noorollahi, Y., Ghasempour, R., & Jalilinasrabad, S. (2015). A GIS based integration method for geothermal resources exploration and site selection. *Energy Exploration & Exploitation*, 33(2), 243-257.

- Noorollahi, Y., Itoi, R., Fujii, H., & Tanaka, T. (2008). GIS integration model for geothermal exploration and well siting. *Geothermics*, 37(2), 107-131.
- Oğuz, H. (2015). A software tool for retrieving landsurface temperature from ASTER imagery. *Tarım Bilimleri Dergisi*, 21, 471-482
- Ozdemir, A. (2012). Geothermal Energy in Turkey: Potential, Exploration Methods, and Properties of Known Geothermal Fields. Elma Publishing, 354 p. (in Turkish)
- Ozdemir, A., Yaşar, E., & Çevik, G. (2017). An importance of the geological investigations in Kavaklıdere geothermal field (Turkey). *Geomechanics and Geophysics for Geo-Energy and Geo-Resources*, 3(1), 29-49,
- Ozdemir, A., Palabiyik, Y. & Arabacı, F. (2021a). Geological structure and geothermal potential of the southeastern Alaşehir, Gediz Graben (Western Anatolia, Turkey). *International Journal of Earth Sciences Knowledge and Applications*, 3(3), 190-207
- Ozdemir, A., Arabacı, F., & Palabiyik, Y. (2021b). Reevaluation of geothermal potential of Çubukludağ Graben (Western Anatolia, Turkey). *International Journal of Earth Sciences Knowledge and Applications*, 3(2), 70-88
- Ozdemir, A., & Palabiyik, Y. (2019). A new method for geological interpretation of 3D MT (magnetotelluric) depth maps of high-temperature and deep geothermal fields: A case study from Western Turkey. *In 2nd International Congress on Applied Sciences*, 28-30.
- Pamir, A.N. (2003). Dünyada ve Türkiye'de Enerji, Türkiye'nin Enerji Kaynakları ve Enerji Politikaları. *Metalurji Dergisi*, 134, 73-100.
- Shahi, H., & Kamkar-Rouhami, A. (2014). A GIS-based weights of evidence model for mineral potential mapping of hydrothermal gold deposits in Torbat-e-Heydarieh area. *Journal of Mining and Environment*, 5(2), 79-89.
- Testa, F.J. Villanueva, C., Cooke, D.R., & Zhang, L. (2018). Lithological and Hydrothermal Alteration Mapping of Epithermal, Porphyry and Tourmaline Breccia Districts in the Argentine Andes using ASTER Imagery. *Remote Sensing*, 10(2):203.
- Öztürk, T., & Uyguçgil, H. (2018). Hidrokarbon Aramacılığında Çizgiselliğin Bulunması İçin Bir Yöntem. *VII. Uzaktan Algılama ve CBS Sempozyumu*.
- Yalçın, M., & Gül, F.K. (2017). A GIS-based multi criteria decision analysis approach for exploring geothermal resources: Akarcay basin (Afyonkarahisar). *Geothermics* 67,18-28
- Yıldız, A., Bağcı, M., Başaran, C., Çonkar, F.E., & Ayday, C. (2017). Landsat 8 uydu verilerinin jeotermal saha araştırmalarında kullanılması: Gazligöl (Afyonkarahisar) çalışması. *Afyon Kocatepe Üniversitesi Fen ve Mühendislik Bilimleri Dergisi*, 17(4), 277-284
- Ninomiya, Y. (2002). Mapping quartz, carbonate minerals, and mafic-ultramafic rocks using remotely sensed multispectral thermal infrared ASTER data. *In Thermosense XXIV* (Vol. 4710, pp. 191-202). SPIE.
- Yurteri, C., & Şimşek, Ş. (2017). Hydrogeological and hydrochemical studies of the Kaman-Savcili-Büyükoba (Kirsehir) geothermal area, Turkey. *Geothermics*, Volume 65, Pages 99-112.



© Author(s) 2021. This work is distributed under <https://creativecommons.org/licenses/by-sa/4.0/>

Forest fire disaster risk analysis using Sentinel 2 and Landsat images case study: Al-Qoubaiyat and Tyre regions, Lebanon

Mohamed Issa*¹, Mohammad Abboud¹

¹Lebanese International University, School of Engineering, Topographic Surveying Department, Beirut, Lebanon

Keywords

DRR
Forest Fire
Satellite Remote Sensing
Burn Index
GIS
Lebanon

ABSTRACT

Fires are considered a threat to the world with all its components and sectors. Recently, it is noticeable an increase in these fires that hit many countries, especially in Lebanon which is considered a country, rich in forests. A forest fire can be naturally caused by either global warming or high temperature. On the other hand, it may be caused by man-made via factories and glass waste. Fires cause great damage to the environment and may lead to human death. Unfortunately, the fire that broke out in AL-Qoubaiyat and Tyre in Lebanon, have been witnessed and caused great damage to the environment, human losses, etc. In this study, a study of fire risk management for those two study areas, will be analyzed using two types of data (Landsat-8 and Sentinel-2) for AL-Qoubaiyat case study, whereas it will be between (Landsat-7 and Sentinel-2) for the Tyre case study. The Analysis will be done by using the Normalized Burn Ration (NBR), Differenced Normalized Burn Ration (Δ NBR) along with all type of required atmospheric corrections. According to our study, it was found advisable to monitor fire risk management using Sentinel-2 L2A data since the atmospheric correction is already performed on it but for L1C data the Sen2Cor python must be used to apply atmospheric correction. Furthermore, the Sentinel-2 L2A data analysis gave more precise results than Landsat-8 by about 2% in Sour case study and 5.7 % in AL-Qoubaiyat case study. Hoping that this method will help in tracking fires, disaster risk reduction, and help in classifying burn severity accompanied with calculating the area corresponding to each class.

1. INTRODUCTION

Since ancient times, forests have been considered an integral part of the human ecosystem and its environment. Frankly, they are the greatest bounty of nature to mankind and play a very important role in its life. In addition to providing shelter and protection to a great number of living beings, including pre-historic man, forests have been the main source of food, wood, and a large variety of other products. In fact, forests have played an important role in various economic, social, and religious activities in human life. Globally, forests encounter increasing challenges and risks from natural disasters, which continue to strike unabated without warning and are consistently increasing in their magnitude, frequency, complexity, and economic impact. To clarify, a forest fire is the most common hazard in forests as well as it is one of the

major disasters responsible for forests' degradation. In fact, forest fires have multiple causes as well as many consequences.

Those forest fires are caused either by anthropological or natural causes. In general, all over the globe, the majority of fires are caused by human activity (Ali, 2020). According to estimation, there are about 50,000 fires that occur each year in the Mediterranean basin and affect more than 600,000 hectares. Moreover, a reported number of 251 fires took place in the year 2020 in Lebanon with burnt area equals to 1851 ha. To be clear, the majority cause of fires in the Mediterranean basin is of human origin resulting either by accident, negligence, or intention (Haddad et al., 2014).

There are many consequences of forest fires, besides posing a serious threat to the forest's wealth, it also affects the entire regime of flora and fauna, thus disturbing the biodiversity of ecology and

* Corresponding Author

(mohamed.issa@liu.edu.lb) ORCID ID 0000-0002-8263-2225
(mohammad.abboud@liu.edu.lb) ORCID ID 0000-0003-3810-633X

Cite this article

Issa, M., & Abboud, M. (2022) Forest fire disaster risk analysis using Sentinel 2 and Landsat images case study: Al-Qoubaiyat and Tyre regions, Lebanon. Turkish Journal of Geosciences 3(2), 84-94.

environment. However, the impact of forest fires is not limited only to its physical component but also goes beyond it as it affects the socio-economic condition of the affected population. Moreover, forest fires also can have global consequences as it produces gaseous and particle emissions that affect the composition and functioning of the jet stream and the global atmosphere, exacerbating climate change as they feedback in global warming since they result from burning vegetation and release of stored carbon (Ali, 2020).

During the last decades, many researchers tried to analyze the usage of Remote Sensing (RS) techniques for forest fire risks, prevention, assessment and monitoring. These techniques have been employed to address three different temporal fire-effects phases: pre-fire conditions, active fire characteristics and post-fire ecosystem responses (Chu and Guo, 2014). Numerous algorithms and approaches for the first two phases have been developed; little effort, however, has yet been dedicated to assessing suitable RS data and methods over the widely spatial and temporal ranges of post-fire-affected environments.

Within the fire science community, there are a variety of terms used to describe the characteristics of fire and its effects. For instance, Sabuncu and Ozener, (2018), reviewed some of these terms: pre-fire environment, fire environment, active fire, post-fire environment, fire regimes defined by fire intensity, fire and burn severity, season of burn, type of fire and burned size and shape. They addressed many factors that can be used to detect fire severity and analyze its effect. Some of these factors are: NBR, Δ NBR, NDVI, Δ NDVI, pixel based classification, and object based classification (Sabuncu and Ozener, 2018). On the other hand, different RS data sources can be used related to a forest fire analysis. Fire-damaged areas could be identified by classifying optical satellite images such as Landsat or MODIS. Object-based classification and spectral classification are some of these methods. In addition, calculating land surface temperature with thermal bands of optical images is used to determine fire areas. Besides, topographic parameters such as elevation, slope, and aspect could be produced from the Shuttle Radar Topographic Mission (SRTM) in order to determine fire risk severity. Topographic factors can be integrated into a geographic information system and these areas can be determined by giving certain weights to them. Also, spectral fire indices are used to identify forest fire zones and risk areas (Navarro et al., 2017).

After looking generally at the causes and consequences of fires in forests, this study will focus mainly on Lebanon and specifically in Al-Qoubaiyat and Tyre regions. Since Lebanon has recently witnessed many fires in its forests that not only affected the plant and animal wealth but also

threatened the lives of the citizens with death. The fires occurred in 2021 and caused a great damage.

Because of this, we have used two sources of RS data, that are Sentinel-2 and Landsat (8 and 7) images (pre-fire and post-fire, Table 2 and Figure 5) to evaluate the burnt area in AL-Qoubaiyat and Sour regions corresponding to fires produced during July 2021. Those studies could help us understand both the causes and consequences of spatial variability of post-fire effects. Therefore, the main aim of our study was to test the suitability of Sentinel-2 MSI data and Landsat Operational Land Imager (OLI) for mapping different spectral indices related to the burn severity of the Al-Qoubaiyat and Tyre fires. These indices are cost-effective and spatially comprehensive views of both areas that have been affected by fire in different fire grading.

The Analysis will be oriented toward the selection of best suitable data for fire forest management, used parameters for classification, required corrections, and results analysis. Therefore, in order to accomplish the mentioned aims, the Landsat 8, Landsat 7, and Sentinel 2 data images will be used. In addition, NBR and Δ NBR indices will be used to create the fire risk classes.

2. METHOD

2.1. Study Area

2.1.1. Al-Qoubaiyat area

Al-Qoubaiyat is a village located in the northeast of the Lebanese republic spreading along 70 square kilometers almost and with an elevation of 700 meters above sea level. It is limited by "Akkar al-Atika" village to the west, and by the line that separates the two districts of Akkar (North) and the Hermel "Bekaa" to the east. Al-Qoubaiyat population is mostly around 12,000 persons. It is usually full of people during the summer but few of them stay during the winter due to the severe coldness of the area and the snow. This area suffers from frequent multiple fires every year. Figure 1 illustrates the location of Al-Qoubaiyat study area.

On the 28th of July in 2021, the region of Al-Qoubaiyat, the most greeny scurb and forests area of Akkar, turned into burned area after her core was burnt as a result of successive fires that broke out in it. Briefly, these fires left great destruction in the green forested areas and pine forests; as well it threatens the lives of the residents along with the forest. But the cause of the fire remains unknown, as it is expected to be due to glass waste and human neglect. The cause of the fire spread on such a large scale refers to the wind, dry vegetation, and the overcrowding of the area with forest trees.

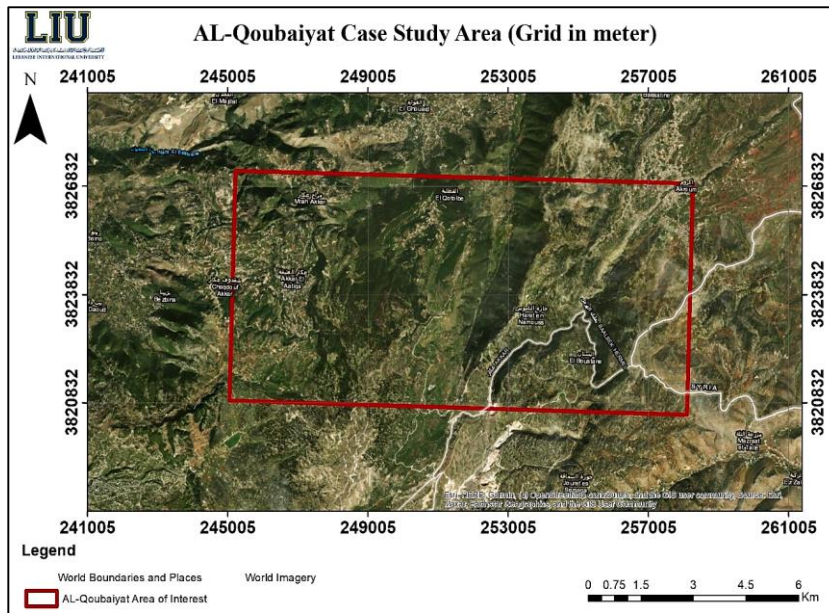


Figure 1. Al-Qoubaiyat study area

2.1.2. Sour (Tyre) Area

The city of Tyre (sour) is situated along the Mediterranean coast, around 80 kilometers south of Beirut with an area of 5 square kilometers. The city is one of the best tourist cities in Lebanon and includes many archaeological sites, which attracts tourists to visit it. Figure 2 illustrate the location of Sour study area. Unfortunately, on November 13,

2021, a huge fire broke out in Wadi AL-Aziya-Zebin in the Tyre region and it spread over large areas of agriculture and forest. The strong winds contributed to the approach of the fire to the residential houses in the town of Haniyeh, Zebin, and Majdel-Zone. The leadership of the Lebanese army suggested that the fire was made by unknowns and spreads through due to the presence of wind, leading to that big damage.

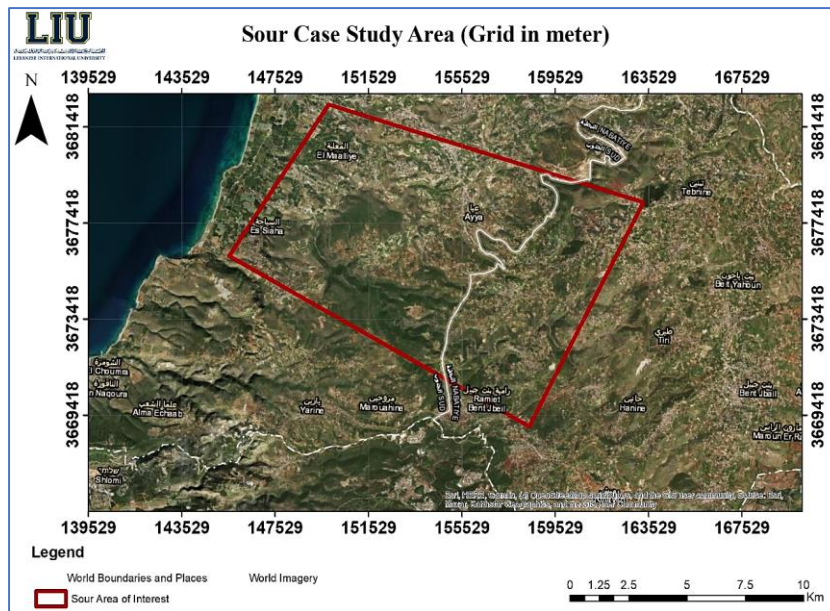


Figure 2. Sour study area

2.2. Methodology and Materials

The methodology demonstrates the procedure that was followed to choose, process, and analyze the data. Fire monitoring is an important project in which it gives information about the burned area,

classification and how to deal with its spread day by day basis. The same methodology was adopted for the two case study areas, that are Al-Qoubaiyat and Tyre in Sour regions. Below, flow chart that represents the methodology that was adopted in this study (Figure 3).

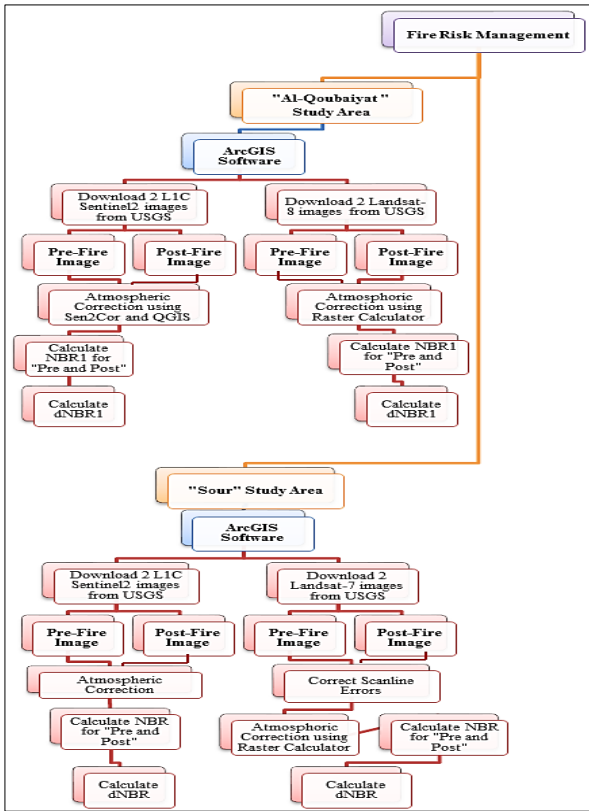


Figure 3. Flowchart illustrating the adopted methodology

The adopted methodologies used in this study, and illustrated in the previous flowchart, are explained briefly as follows:

Processing of Sentinel 2 L1C data:

- Use sen2cor python and QGIS Semi-Automatic Classification Plugin methods to correct the effects that the atmosphere has on Sentinel-2 L1C image data and to obtain the L2A surface reflectance product.
- Import the corrected Sentinel 2 bands (8a, 4, 12) (NIR, Red, SWIR2) to the ArcGIS.
- Then, divide each band by 10,000 using the raster calculator tool.
- After masking water bodies for all bands, use the raster calculator to calculate the (NBR) and (Δ NBR) for both pre and post-fire data of Sentinel.
- Classify the values using burn severity classification and use the reclassify command from the spatial analyst tool to give each class a value.
- Open the attribute table of the reclassified Δ NBR and calculate each burned area.
- Use the conversion tools to transform the reclassified Δ NBR data to a polygon.

Processing of Landsat data:

- Correct Scanline errors for each band used (4, 7) (NIR, SWIR2) in Landsat-7 data by using "fix Landsat 7 Scanline Errors" tool.
- Using the raster calculator tool in ArcGIS, apply an atmospheric and sun angle

correction for Landsat-8 bands (7, 5, 4) (SWIR2, NIR, Red) and Landsat-7 bands.

- Import the corrected Landsat-8 bands (7, 5, 4) (SWIR2, NIR, Red) and the corrected Landsat-7 bands to the ArcGIS.
- Create a polygon shapefile for Landsat data to digitize water bodies.
- Then, use image analysis to mask water bodies using the digitized shapefiles.
- Calculate the (NBR) and (Δ NBR) for both pre and post-fire data of Landsat-8.
- Classify the values using burn severity classification and using reclassify command from spatial analyst tool to give each class a value.
- Open the attribute table of the reclassified Δ NBR and calculate the area.
- Use the conversion tools to transform the reclassified Δ NBR data to a polygon

2.2.1. Software used

A Geographic Information System is a system of computer software that allows the user to enter, manipulate, analyze, and display information that is related to a certain location on the earth's surface. Since forest fires are considered one of the major causes of natural resource destruction, and this is often watched on a global scale, RS and GIS technologies are valuable disciplines in studying the features of the land in which they help in monitoring and detecting the forest fires' causes. In addition, GIS also helps in understanding how to decrease the impacts of forest fires and find a solution to various issues related to it. For instance, GIS software can play an important role before the fire by which it helps the municipalities to mark the exact locations of fire hydrants **Hata! Başvuru kaynağı bulunamadı.** (Stone, 2016). Moreover, GIS can serve an important function in terms of monitoring the burned areas resulting from forest fires and estimating their surface areas.

• Importance of the Use of QGIS in Monitoring Fires:

Concerning the QGIS, it is an acronym for Quantum Geographic Information System which is computer software that allows its users to edit, view, check, and process geospatial data. Moreover, it allows assessing and editing the spatial information needed and creating new maps. In addition, QGIS has many tools functions and it is considered very fast compared to other applications.

QGIS can serve as an important role in monitoring the burned areas resulting from forest fires. Through the QGIS tools, the user can analyze and determine the area affected by fire and classify its burn severity. QGIS tools allow users to employ satellite-based imagery and derivative information to produce a burn severity map and to provide an

important additional resource that supports fire managers.

- **Importance of the Use of Sen2Cor python in Atmospheric Correction:**

Sen2Cor is a prototype processor used to perform a pre-processing of Sentinel-2 Level-1C (L1C) Top of Atmosphere (TOA) image data where it applies an atmospheric correction and converts into Level-2A Bottom of Atmosphere (BOA) reflectance product. To add, it is used for Sentinel-2 data for land applications to ensure the highest quality of scientific exploitation (Mueller-Wilm et al., 2017).

2.2.2 Parameters used in forest fire analysis

NBR and ΔNBR were used as spectral indices for forest fires burn severity monitoring and analysis. The Normalized Burn Ratio “NBR” is an index designed to highlight areas burned in huge fire zones. Its equation is similar to NDVI, except that the equation combines the utilization of both Near Infrared (NIR) and Shortwave Infrared (SWIR) wavelengths as shown in Figure 4.

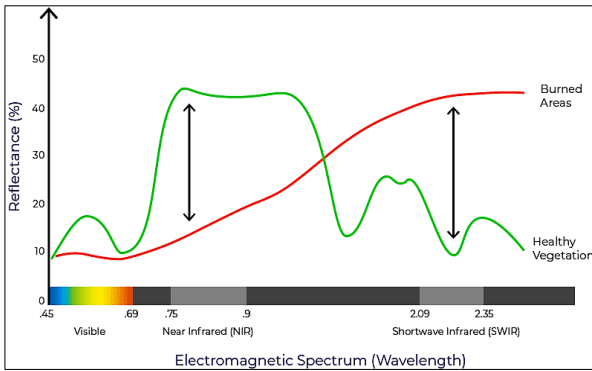


Figure 4. Comparison of the spectral response of healthy vegetation and burned areas (Keeley, 2009)

As shown in Figure 4, healthy vegetation represents a very high reflectance in the NIR portion and a low reflectance in the SWIR portion of the electromagnetic spectrum. This is in contrast to what is seen in areas devastated by fire; recently burnt areas show low reflectance in the NIR portion and high reflectance in the SWIR portion. Accordingly, the difference between the spectral responses of burnt areas and healthy vegetation reach their apex in the NIR and the SWIR portions of the electromagnetic spectrum.

The formula of NBR uses the ratio between NIR and SWIR bands but for making it more accurate some modification in the index was done which is shown in equation number 1. To clarify, a high NBR value signifies healthy vegetation however a low NBR value signifies bare ground and recently burnt areas. The non-burnt areas are normally attributed to values near zero (Keeley, 2009). The following

equation (equation number 1) shows the formula used to calculate the NBR value (Ryu et al., 2018).

$$NBR = \frac{NIR - SWIR}{NIR + SWIR} \quad (1)$$

Where:

NIR: Near Infrared Value

SWIR: Shortwave Infrared wavelengths

Moreover, the burn severity can be estimated from the delta NBR (dNBR or ΔNBR) which can be calculated from the difference between the pre-fire and post-fire NBR obtained from the images (Walz, et al., 2007). The equation below illustrates how to calculate dNBR (equation 2).

$$\Delta NBR = \text{Prefire NBR} - \text{Postfire NBR} \quad (2)$$

Furthermore, a classification table to interpret the burn severity was proposed by the United States Geological Survey (USGS) which can be seen in the table below (Table 1). The burn severity data and maps can help in developing emergency rehabilitation and restoration plan after the fire. In addition, they can be utilized to estimate not only the soil burn severity, but also the probability of future downstream impacts due to flooding, soil erosion, and landslides (Keeley, 2009).

Table 1. The Burn Severity levels, proposed by USGS (Rozario et al., 2018)

ΔNBR	Burn Severity
< -0.25	High post-fire regrowth
-0.25 to -0.1	Low post-fire regrowth
-0.1 to +0.1	Unburned
0.1 to 0.27	Low-severity burn
0.27 to 0.44	Moderate-Low-severity burn
0.44 to 0.66	Moderate High-severity burn
> 0.66	High-severity burn

2.3. Data Collection and Acquisition

In this study the results obtained from two different sources, namely: The Landsat 8 and the Sentinel 2 satellite images for Al-Qoubaiyat study area before and after fire occurrence, were analyzed. The following Table 2 illustrates the differences between the two data sources. On the other hand, for Tyre in Sour region, this case study used the images from Landsat-7 Enhanced Thematic Mapper + (ETM+) and Sentinel 2 satellite images. The main differences between Landsat-7 and Landsat-8 sensors are not only in the numbers of the spectral ranges but also in the radiometric resolution, which is 16 bits for the Landsat 8 OLI platform, and 8-bits

for the Landsat-7 ETM + (Figure 5). The fact that different sensors with different spectral and radiometric resolution are used for change detection

process should be taken into account during the results analysis.

Table 2. Illustration of the differences between Sentinel 2 and Landsat 8 data (Korhonen et al., 2017)

Sentinel-2			Landsat 8		
Band Specification	Wavelength (nm)	Resolution (m)	Band Specification	Wavelength (nm)	Resolution (m)
Band 1—Coastal	433-453	60	Band 1—Coastal	433-453	30
Band 2—Blue	458-523	10	Band 2—Blue	450-515	30
Band 3—Green	543-578	10	Band 3—Green	525-600	30
Band 4—Red	650-680	10	Band 4—Red	630-680	30
Band 5—Vegetation red edge	698-713	20	Band 5—NIR	845-885	30
Band 6—Vegetation red edge	734-748	20	Band 6—SWIR	1560-1660	30
Band 7—Vegetation red edge	765-785	20	Band 7—SWIR	2100-2300	30
Band 8—NIR	785-900	10	Band 8—Panchromatic	500-680	15
Band 8a—Vegetation red edge	855-875	20	Band 9—Cirrus	1360-1390	30
Band 9—Water vapor	930-950	60	Band 10—Thermal	10,600-11,200	100
Band 10—SWIR—Cirrus	1365-1385	60	Band 11—Thermal	11,500-12,500	100
Band 11—SWIR	1565-1655	20			
Band 12—SWIR	2100-2280	20			

Landsat 7 ETM+ Bands (mm)	Band 1	30 m Blue	0.441 - 0.514
	Band 2	30 m Green	0.519 - 0.601
	Band 3	30 m Red	0.631 - 0.692
	Band 4	30 m NIR	0.772 - 0.898
	Band 5	30 m SWIR-1	1.547 - 1.749
	Band 6	60 m TIR-1	10.31 - 12.36
	Band 7	30 m SWIR-2	2.064 - 2.345
Landsat 8 OLI and TIRS Bands (mm)	Band 8	15 m Pan	0.515 - 0.896
	Band 1	30 m Coastal/Aeros	0.435 - 0.451
	Band 2	30 m Blue	0.452 - 0.512
	Band 3	30 m Green	0.533 - 0.590
	Band 4	30 m Red	0.636 - 0.673
	Band 5	30 m NIR	0.851 - 0.879
	Band 6	30 m SWIR-1	1.566 - 1.651
	Band 7	30 m SWIR-2	2.107 - 2.294
	Band 8	15 m Pan	0.503 - 0.676
	Band 9	30 m Cirrus	1.363 - 1.384
	Band 10	100 m TIR-1	10.60 - 11.19
Band 11	100 m TIR-2	11.50 - 12.51	

Figure 5. Illustration of the differences between Landsat 7 ETM and Landsat 8 data (Jovanović et al., 2015)

The satellites images used within the scope of this study were obtained free of charge from the United States Geological Survey (USGS) site in UTM projection. The gathered data are:

- For El_Qoubaiyat study area:
Sentinel 2 satellite data from USGS for Qoubaiyat: pre-fire (19/7/2021) and post-fire (3/8/2021).
Landsat 8 satellite data from USGS for Qoubaiyat: pre-fire (26/7/2021) and post-fire (11/8/2021).

During this stage, the collected data are processed using ArcGIS. To clarify, Sen2Cor python is used only to apply an atmospheric correction for L1C Sentinel 2 data.

- For Sour study area:
Sentinel-2 satellite data from USGS for Sour: pre-fire (11/11/2021) and post-fire (16/11/2021).ss

Landsat-7 satellite data from USGS for Sour: pre-fire (7/11/2021) and post-fire (23/11/2021).

2.3.1. Notes on data processing:

In order to obtain the burned areas from the gathered data, the following processing corrections were made:

- The sen2cor python was used to correct the effects that the atmosphere has on Sentinel-2 L1C image data and to obtain the L2A surface reflectance product.
- The ArcGIS image analysis was used to mask water bodies using the digitized shapefiles. This due to that ΔNBR is sensitive to water and thus, sometimes pixels that are classified as high severity may be water (Rutkay et al., 2020).
- The symbology and reclassify command were used to classify the values using burn severity classification according to the classification Table 1.
- The ArcGIS raster calculator tool was used to apply an atmospheric and sun angle correction for Landsat-8 bands (7, 5, 4) (SWIR2, NIR, Red).
- Correct Scanline errors for each band used (4, 7) (NIR, SWIR2) in Landsat-7 data by using “fix Landsat 7 Scanline Errors” tool. That is, “fix Landsat 7 Scanline Errors” tool which found in the Landsat Toolbox was first used in order to correct the Scanline errors for each band used. After that, equation (3) was applied for each band by using the raster calculator tool and with the aid of information found in the metadata file of the Landsat-7.

$$(TOA\ reflectance = \frac{Band \times (Radiance_Max_Band - 255 - Radiance_Min_Band + 255) - Radiance_Min_Band}{\sin(\text{sun elevation})}) \quad (3)$$

3. RESULTS

After calculating NBR for pre and post-fire of both Sentinel-2 and Landsat-8 data, the indices Δ NBR were calculated using the raster calculator tool and in reference to equation No. 1 and 2. As a remark, setting an analysis mask for these indices must be done before processing where Δ NBR indices were masked according to a previously digitized shapefile for burned area. To clarify, this step that was done in the environment tab means that the processing for Δ NBR will only occur on locations that fall within the mask.

Concerning the classification of burn severity, it was done inside the ArcGIS using properties of calculated Δ NBR layer (Symbology) and in accordance to Table 1.

Area calculation for burn severity classes was done using the reclassification tool and multiplying the count number in each class by the cell size, taking into account that the cell size of sentinel-2 image is (20×20) m while that of landsat-8 is (30×30) m. After that, the L2A and Landsat-8 data of burned areas were arranged in excel, and the difference in area between them was calculated. For the 4 individual polygons that represent burned areas, the percentage of area difference between L2A and Landsat-8 data was calculated by dividing their area difference by the polygon area for L2A data since total L2A area is more than total Landsat-8 area. Afterwards, the percentage for the total difference was calculated by dividing the total difference value by the total L2A area (see Table 3 and Figure 6).

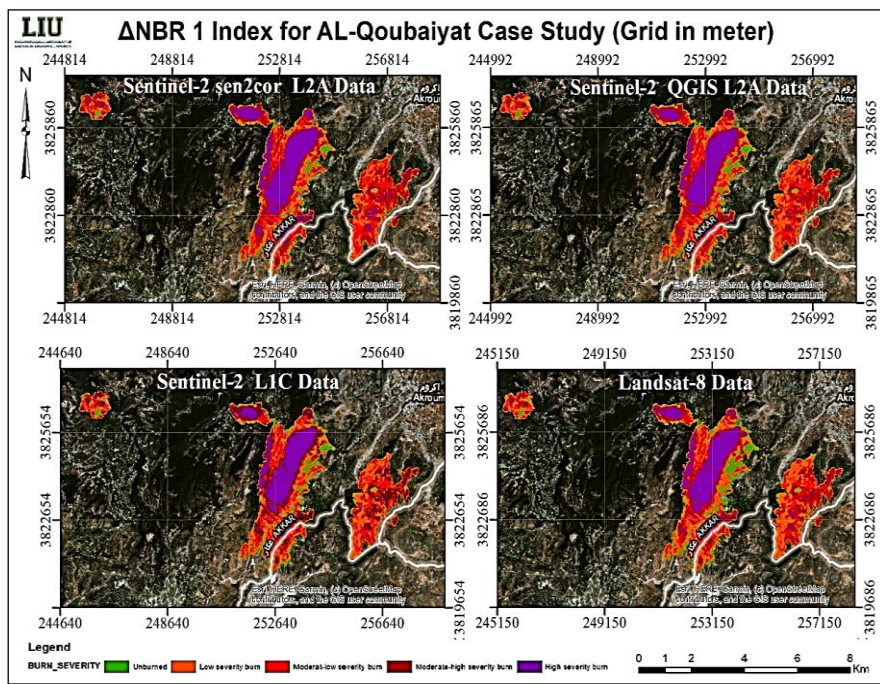


Figure 6. The dNBR classified map for Al-Qoubaiyat case study

Table 3. Table includes percentage of area difference between L2A and Landsat-8 Data for Al-Qoubaiyat area polygons

Al-Qoubaiyat	Polygon Area (Km ²)	(L2A-Landsat 8) km ²	Percentage of area difference between L2A and Landsat-8 data
Burned Area 1	0.721	0.035	4.9 %
Burned Area 2	0.848	0.031	3.6 %
Burned Area 3	4.035	0.118	2.9 %
Burned Area 4	8.632	0.630	7.3 %
Total Area	14.235	0.814	5.7 %

From this table, it can be seen that either Sentinel-2 or Landsat images can be used to classify and estimate the fire risks with difference ranges between 3 % to about 7 %. In addition, since the areas were arranged in ascending manner, this difference is increased as the area of spotted polygon increased. The difference may be attributed also to

the difference in pixel size between the two data sources. The calculated area was compared to the values estimated by the CNRS and they were very close and the differences can be attributed to the fact that CNRS had used a different post-fire image data from ours where the fires that had ignited post 29 July were not considered in the statistics of CNRS

map. For instance, (as depicted in Figure 7.), the reported burned area from CNRS was 10.27 km², the moderate to low severity was 2.71 km², the moderate to high severity was 3.85 km², and the high severity was 3.72 km².

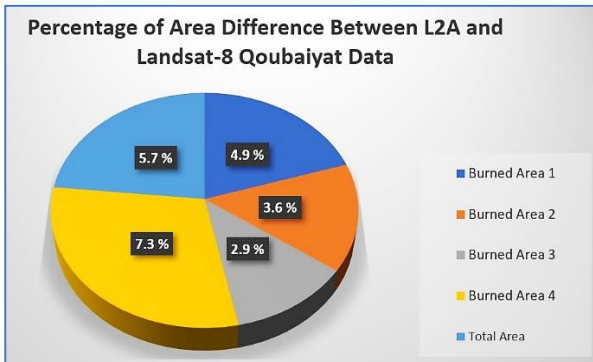


Figure 7. Illustration of the difference in area calculation for burned areas between L2A and Landsat-8

Figure 8 represents two classified fire burn severity maps for Al-Qoubaiyat case study; one resulted from Sentinel-2 L1C data atmospherically corrected using Sen2Cor python and second resulted from atmospherically corrected Landsat-8 data. These two results that obtained from Sentinel-2 Sen2Cor L2A and Landsat-8 data are similar visually with some differences in unburned, low-severity burn, and Moderate-low severity burn classes in the east side of the biggest burned area limit which may be due to the cell size difference between these two data images. Moreover, in the smallest polygon to the left the high severity class differs between L2A and Landsat-8 where it is wider in L2A than in Landsat-8. On the other hand, the high severity area almost equals to the low severity area where both of them equals to about 3.45 km². It should be noted that every year the fire took place in this region, and as can be seen, it starts in four different places which makes someone believes that fires were due to arson.

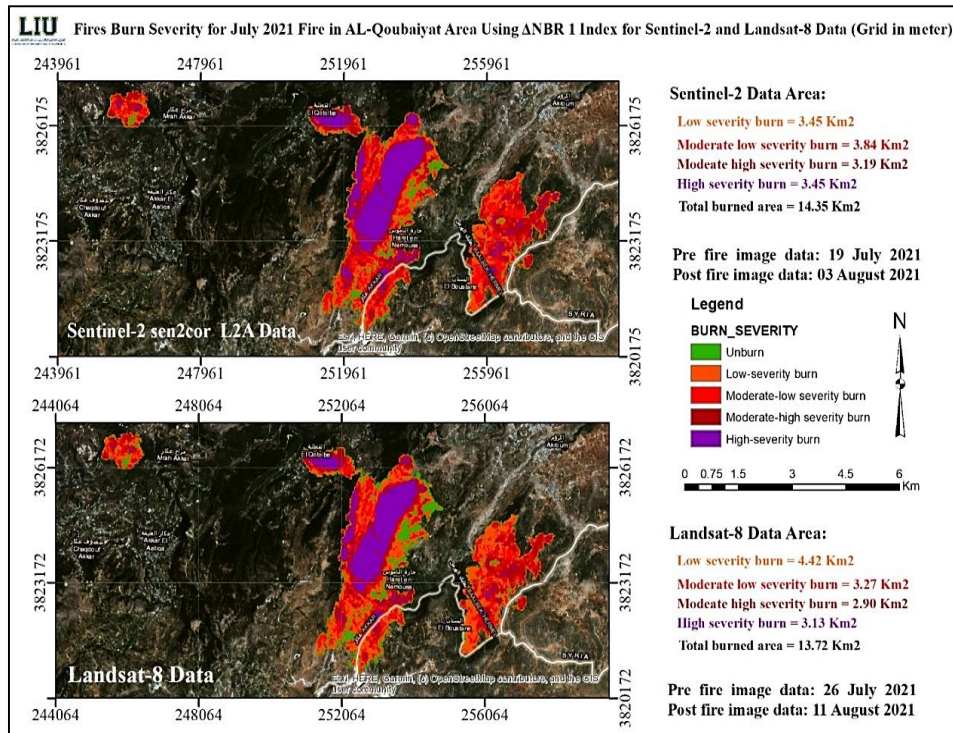


Figure 8. Figure showing fire burn severity map for July 2021 fire in Al-Qoubaiyat area using dNBR index for Sentinel-2 L2A data and Landsat-8 data

Concerning the Sour case study, the resulted fire burn severity maps for November 2021 fire using dNBR index, as calculated from Landsat-7 images, are shown in the Figure 9. These maps are also classified according to burning severity levels into 5 classes noting that data was also atmospherically corrected. From this figure, it can be seen that the

burn severity classification in this figure is logical visually where the moderate low severity burn class is dominant, the high severity class is present at the center of fire, and the unburned class is present at the border of the burned area and this corresponds to the actual fires noticed on the ground by fire fighter's groups shared in extinguishing fires.

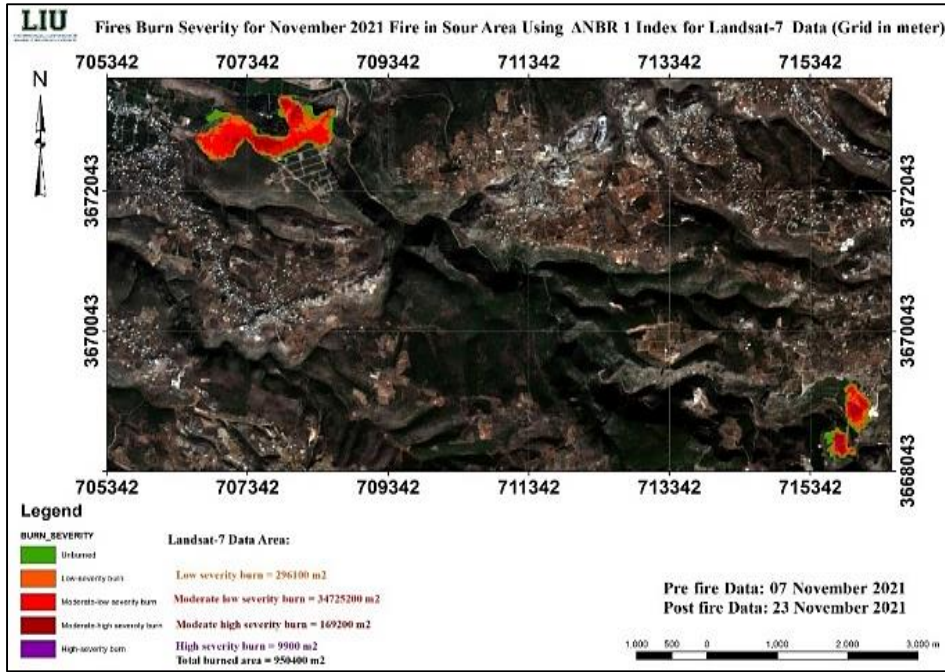


Figure 9. Illustration of fire burn severity map for November 2021 in Sour area using dNBR index for Landsat-7 data

Concerning the Sentinel-2 data, for Sour city, Figure 10. shows a classified map that is resulted from Sentinel-2 L1C data atmospherically corrected using Sen2Cor python. In this figure, it is noticeable that the low severity class is the dominant class, the high severity class is present at the center of fire, and the unburned class is also present at the border of

the burned areas. In addition, as written on the map, the low risk area equals to 100,1200 m², the moderate low severity equals to 406,800 m², the moderate high severity equals to 406,800 m², the high severity equals to 72,000 m², the total burned area equals to about 180,000 m².

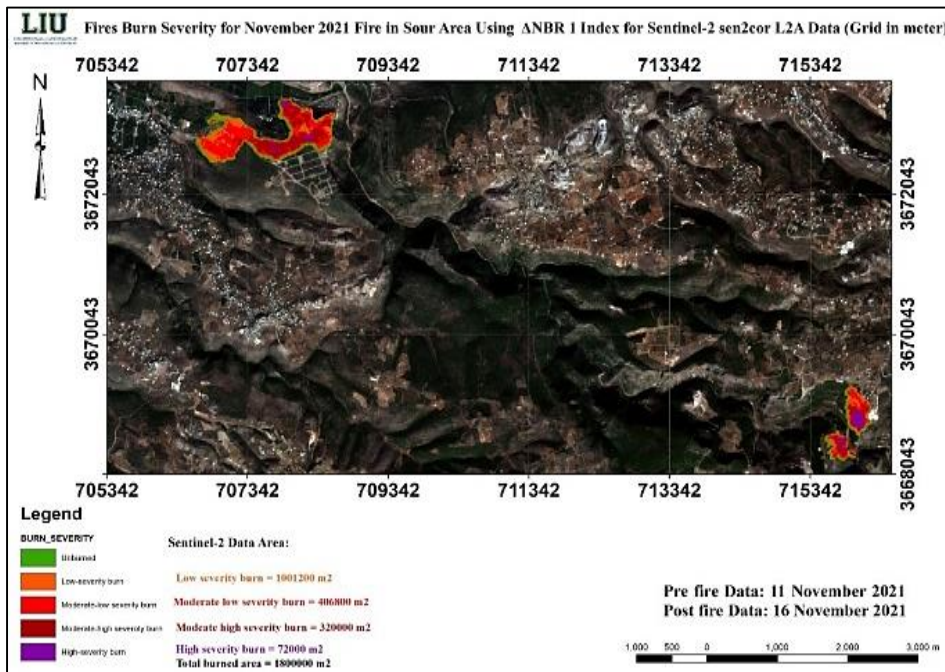


Figure 10. Demonstration of fire burn severity map for November 2021 in Sour area using dNBR index for Sentinel-2 Sen2Cor L2A data

In the following Figure 11, two classified fire burn severity maps for Sour case study are shown. The first one was resulted from Sentinel-2 L1C data

and atmospherically corrected using Sen2Cor python, whereas the second one was resulted from atmospherically corrected Landsat-7 data.

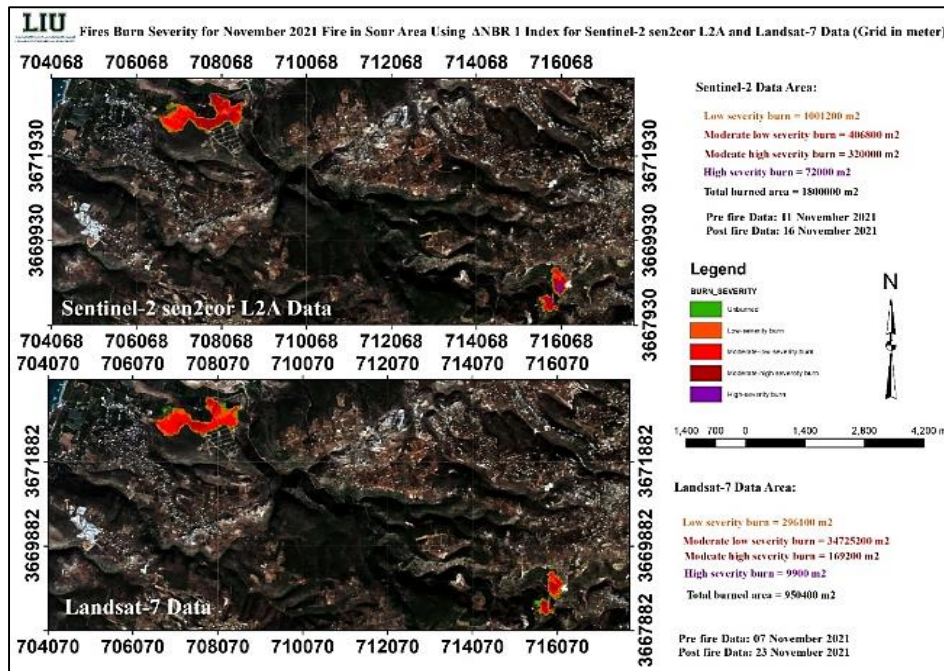


Figure 11. Figure showing fire burn severity map for November 2021 fire in Sour area using dNBR index for Sentinel-2 L2A data and Landsat-7 data

These two results that were obtained from Sentinel-2 Sen2Cor L2A and Landsat-7 data are, also, similar visually with some differences in burn severity classes at the border and at the center of fire region. To explain further, the moderate-high severity burn class at the center of fire region is higher in Sentinel-2 Sen2Cor L2A data than that in Landsat-7 data. That is, the unburned class in Landsat-7 is more noticeable than in Sentinel-2 L2A at the borders.

The following Table 4 represents the percentage of area difference between Sentinel-2 L2A and Landsat-7 data for the 2 biggest polygons in Sour case study. The area values in this table were calculated with the use of polygons area in ArcMap. It can be noticed that the percentage of the total area difference between Sentinel-2 L2A and Landsat-7 burned area is 2% which differs from that in Al-Qoubaiyat case study “5.7%”.

Table 4. The percentage of area difference between L2A and Landsat-7 Data for the 2 biggest polygons “Sour”

Sour Case Study	Shape Area L2A (m ²)	Shape Area Landsat 7 (m ²)	Area Difference (L2A-Landsat 7) m ²	Percentage of area difference between L2A and Landsat-7 data
Burned Area 1	747766.264	740979.556	6786.7082	0.9 %
Burned Area 2	151185.038	138117.578	13067.4608	9.4 %
Total Area	898952	898952	19854.169	2 %

From the previous table, it can be noticed also that the difference is increased as the area of spotted polygon increased.

4. CONCLUSIONS AND RECOMMENDATIONS

In conclusion, through this study two types of data for each of Al-Qoubaiyat and Sour case studies were handled. In addition, multiple atmospheric correction methods were applied in a way to verify the most reliable data. The data used for Al-Qoubaiyat case study are the Sentinel-2 L1C data and the Landsat-8 data while for Sour case study are the Sentinel-2 L1C data and the Landsat-7 data. A categorized map for both case studies showing the severity of burns as well as the area values for each

category, were obtained. According to performed analysis, among the atmospheric correction methods for Sentinel-2 L1C data, the most reliable and accurate correction method is Sen2Cor python. According to the work that was done and clarified previously about the “5.7%” between Sentinel-2 L2A and Landsat-8 data in Al-Qoubaiyat, it can be said that Sentinel-2 data is the most reliable data that can be directly relied upon in fire risk management due to its cell size and its complete full earth coverage each 10 days. To be clear, Sour case study came to verify the results that were obtained in Al-Qoubaiyat where the analysis also gave a positive value “2%” meaning that Sentinel-2 still gave more burnt area than Landsat.

Therefore, henceforth, for any fire or fire spark that may occur in the future, anyone who wants to study and monitor fire risk management he can directly use Sentinel-2 L2A data since the atmospheric correction is already performed on it but for L1C data the Sen2Cor python must be used to apply atmospheric correction.

According to study findings, it is recommended:

If possible, use post-fire image data as close as possible to the date of fire disaster to avoid the regrowth of burned vegetation.

Directly use Sentinel-2 L2A data or L1C data atmospherically corrected using Sen2Cor python.

Make sure to mask water bodies, if existed in your case study, before calculating NBR index in order to ensure that these bodies will not affect this index.

In addition, it is recommended for future work to categorize the trees in the vegetation texture according to their types to increase the accuracy of the study.

Using QGIS is much easier over traditional ArcGIS since for automatic correction of data atmospherically.

Acknowledgement

We are also grateful to the three anonymous reviewers for their constructive comments.

Author Contributions

Mohamed Issa: Conceptualization, Methodology, Software and Data curation. **Mohammad Abboud:** Data download and editing, Writing- Original draft preparation and contributed to the discussion.

Conflicts of Interest

The authors declare no conflict of interest.

REFERENCES

Ali, E. (2020). Geographic Information System (GIS): Definition, Development, Applications & Components. *Department of Geography, Ananda Chandra College, India.*

Rutkay, A., Kalkan, K., & Gürsoy, Ö. (2020). Determining the forest fire risk with sentinel 2 images. *Turkish Journal of Geosciences*, 1(1), 22-26.

Haddad, E.A., Farajalla, N., Camargo, M., Lopes, R.L., & Vieira, F.V. (2014). Climate change in Lebanon: Higher-order regional impacts from agriculture. *Region*, 1(1), 9-24.

Chu, T., & Guo, X. (2013). Remote sensing techniques in monitoring post-fire effects and patterns of forest recovery in boreal forest regions: A review. *Remote Sensing*, 6(1), 470-520.

Navarro, G., Caballero, I., Silva, G., Parra, P.C., Vázquez, Á., & Caldeira, R. (2017). Evaluation of forest fire on Madeira Island using Sentinel-2A MSI imagery. *International Journal of Applied Earth Observation and Geoinformation*, 58, 97-106.

Ryu, J.H., Han, K.S., Hong, S., Park, N.W., Lee, Y.W., & Cho, J. (2018). Satellite-based evaluation of the post-fire recovery process from the worst forest fire case in South Korea. *Remote Sensing*, 10(6), 918.

Jovanović, D., Govedarica, M., Sabo, F., Bugarinović, Ž., Novović, O., Beker, T., & Lauter, M. (2015). Land cover change detection by using remote sensing: A case study of Zlatibor (Serbia). *Geographica Pannonica*, 19(4), 162-173.

Keeley, J.E. (2009). Fire intensity, fire severity and burn severity: a brief review and suggested usage. *International journal of wildland fire*, 18(1), 116-126.

Korhonen, L., Packalen, P., & Rautiainen, M. (2017). Comparison of Sentinel-2 and Landsat 8 in the estimation of boreal forest canopy cover and leaf area index. *Remote sensing of environment*, 195, 259-274.

Mueller-Wilm, U., Devignot, O., & Pessiot, L. (2016). Sen2Cor configuration and user manual. *Telespazio VEGA Deutschland GmbH: Darmstadt, Germany.*

Rozario, P.F., Madurapperuma, B.D., & Wang, Y. (2018). Remote sensing approach to detect burn severity risk zones in Palo Verde National Park, Costa Rica. *Remote Sensing*, 10(9), 1427.

Sabuncu, A., & Ozener, H. (2018). Evaluating and Comparing NDVI and NBR Indices Performance for Burned Areas in Terms of PBIA and OBIA in Aegean Region Turkey. *FIG Congress, 2018*

Walz, Y., Maier, S.W., Dech, S.W., Conrad, C., & Colditz, R.R. (2007). Classification of burn severity using Moderate Resolution Imaging Spectroradiometer (MODIS): A case study in the jarrah-marri forest of southwest Western Australia. *Journal of Geophysical Research: Biogeosciences*, 112(G2).

